Engineering | Lancaster University

Optimising the generation of hydrogen as a carbon-free fuel for the future, by development of new and unique catalytic coatings

Yifu Wang

Supervisors:

Dr Nuno Bimbo Dr Richard Dawson

Thesis submitted in the fulfillment for the degree of Master by Research in Engineering

January 2020

Acknowledgement

I would like to express special appreciation to my primary and secondary supervisors, Dr Nuno Bimbo and Dr Richard Dawson from Lancaster University, both of whom convincingly guided and inspired me in this subject which has remarkable impact in my career development. Without the persistent help from either supervisor, the objectives of this project would not be successfully achieved. I also would like to thank to Centre for Global Eco-Innovation and Clean Power Hydrogen Ltd for both financial and technical support.

Abstract

The demand of producing hydrogen energy in a more efficient and cleaner process has been a top priority for scientists as hydrogen energy is expected to be a splendid alternative of fossil fuel in many applications such as trains and airplanes. This thesis aimed to improve the efficiency of alkaline water electrolysis system by developing a low-cost catalytic coating on its anode that is made of stainless steel, where oxygen evolution reaction occurs. Nickel-iron based materials are main focus in this study due to their low price, high earth abundance and high activity towards OER. The thesis contained the cyclic voltammetry and linear sweep voltammetry results of metallic NiFe and NiFe (oxy)hydroxide prepared by electrodeposition and thermal deposition methods. Chronoamperometry was used to study the durability of the materials. The thesis also contains SEM images EDS mappings of coatings for morphological and elemental analysis. The most significant finding of the study is that NiFe hydroxide thin film prepared by electrodeposition improved OER drastically by showing 0.518 V overpotential at 10 mA cm^{-2}. In a bench-scale single cell electrolyser test, the anode with NiFe hydroxide thin film generated 5.7 times as much columbic charge as electrode without coating when 1.6 V was applied for 30 minutes at room temperature and the electrolyte concentration was 0.1 M. These results indicate that the methodology can be applied to commercial scale of alkaline water electrolyser with stainless steel substrates for further testing.

List of Contents

List of Figures

List of Tables

1. Introduction

1.1 Issues with fossil fuels

Fossil fuels include coal, oil and gas are currently the major energy sources that are used in the world. They are cheap and generate sufficient amounts of energy to meet our daily demand for heating, electricity and transportation. However, the continued consumption of fossil fuels would lead to many issues, both environmentally and socially. The main disadvantages are:

1. **Climate impact**

   Burning fossil fuels produces carbon dioxide, carbon monoxide and other toxic gases. One of the major products, carbon dioxide, is responsible for the acceleration of global warming. Rise of temperature is severely damaging the earths' ecosystems and climate [1]. For example, the increasing temperatures are causing ice melting in polar regions, flooding to lower villages and towns, rising sea levels [1]. If this phenomenon continues, the consequences will affect environments and make it unsuitable for human beings and animals to live.

2. **Non – renewable and non – sustainable**

   The formation of fossil fuels is a long process and usually takes 50 – 60 million years, which is much slower than the rate at which they are being depleted [2]. In another word, when fossil fuel is run out, human beings and their future generation will lack of energy source. Hence to secure energy supplies for future generations, it is essential to seek alternatives energy sources and at a large scale.

3. **Causing health issues**

   During the combustion of hydrocarbon (coal), many particulates such as NOx, SOx and VOCs, will be released into the air which will then be inhaled by human beings. They may damage organs such as lungs and inspiratory systems within our bodies. Consequently, they may lead to some disease such as asthma, eye irritation, cardiovascular disease, cancer and neurological deficits [3].

4. Unstable cost

The cost of fossil fuel, especially for oil, keeps fluctuating depends on political situations and market circumstances. This leads to a very unstable cost of fossil fuel [4]. However, the cost of the fossil fuel is only a minor concern compared to health and environmental aspects.

1.2 Hydrogen as a fuel

As the demand for alternative energy resources continuously increases, renewable solutions and technologies for energy storage and conversion are urgently required. One of the major solutions is to use hydrogen as an energy storage vector and fuel due to its high mass-specific energy density, in replacement of fossil fuel, which contributes approximately 33% of total global CO_2 emissions in transportation sector in 2018 [5]. The hydrogen can be used directly

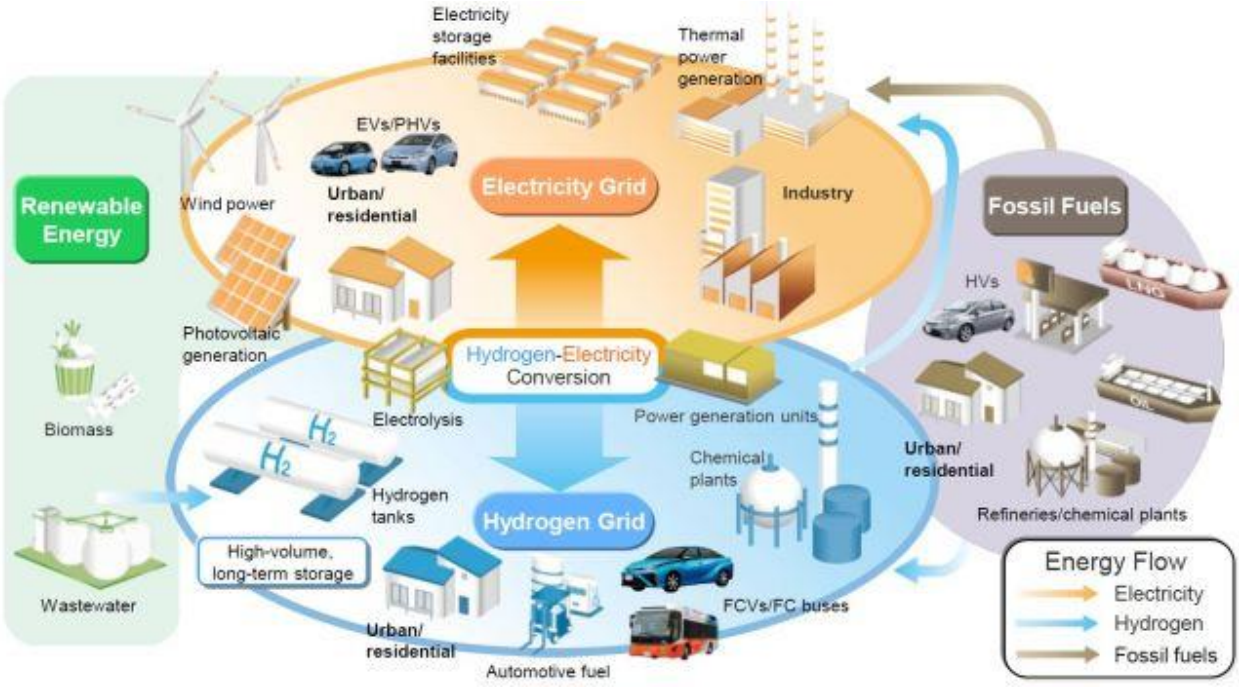

Figure 1. Flow diagram of hydrogen-electricity conversion [5].

in heating, transportation and electrical supply applications. As Figure 1 shows, in the future hydrogen economy, hydrogen is the key 'at scale' energy storage medium for energy system. The electricity can be supplied to industries and residential demand. Hydrogen itself as an energy carrier can be used in automotive fuel too, most likely for heavier transport at least initially [6]. Other applications such as fuel cells, will also require hydrogen to power them. Renewable energy

resources such as wind, solar and biomass will also play an important role in low – carbon society, whilst the consumption of fossil fuels is very significantly reduced. Importantly, the main product after hydrogen burnt or utilised in a fuel cell is water, which is much cleaner than fossil fuels as using hydrogen would reduce carbon emission to zero. It however also produces particulates VOCs, NOx and SOx.

1.3 Hydrogen production

There are 3 main routes to produce hydrogen:

1) **Thermo chemical route (reforming of hydrocarbons)**

This process involves heating of natural gas (methane) mixed with water steam to separate hydrogen from carbon [7]. At present, 95% of the global hydrogen is commercially produced by using fossil fuels and the steam reforming process has been utilised for this purpose for decades. This complex industrial process has always been suffered from low purity of hydrogen generation in accompany with the production of greenhouse and toxic gases such as carbon monoxide and carbon dioxide. This process is environmentally unfriendly, although it is the cheapest way to produce hydrogen [8].

In order to boost hydrogen economy, an alternative hydrogen production process must be developed to replace steam reforming. The most important consideration is that producing more hydrogen than the energy used to extract that amount of hydrogen.

2) **Biological route**

In a biological route, biomass is converted to hydrogen using microbial processes such as anaerobic digestion [9]. The issue of this route is that it is only studied in laboratory scale and some small pilot plants. There is still a long way to go for them to achieve industrial application as improving efficiency and purity is one of the major R&D needs for this technology [10].

3) **Electrochemical route**

Electrochemical route involves using electrochemical device called electrolyser, which could split up water molecules into hydrogen and oxygen. There are lots of electrolysers are already in market and have been used in electric vehicles. For example, atmospheric alkaline electrolyser provided by Nel [12].

Among these 3 routes, electrolysis is most likely to be an alternative of steam reforming with appropriate engineering work and cost reduction. Currently, using natural gas and the raw energy feed to a system (steam reforming) is more efficient route to generate hydrogen, whereas hydrogen production by electrolysis only makes sense if excess renewable electricity needs storing.

1.4 Water electrolysis

Many countries have set clear goals to minimise the greenhouse gas emissions in a broad range of industrial processes including hydrogen production. The development of electrolytic hydrogen production, also called electrolysis, is vital to boost low-carbon economy. Electrolyser in brief description is an electrochemical device which enable water (H_2O) to decompose into oxygen (O_2) and hydrogen (H_2) by electrical energy [11]. This technology can achieve zero carbon footprint by renewable energy source [11]. For example, when excessive electrical energy is produced by wind or solar energy, this extra can be stored by passing it into electrolyser. A typical electrolyser contains several main components:

- Electrodes: As other electrochemical device, an electrolyser contains anode and cathode, at which OER and HER occur under passage of electrical current. In commercial electrolysers, the electrodes are accompanied by electrocatalysts, which facilitate HER and OER at respective electrodes.
- Electrolyte: This allows the chemical species involved in electrochemical reactions to transport from anode to cathode (or the other way). For electrolysers, the chemical species can be either proton (H^+) or hydroxyl ions (OH^-), depends on the category of electrolysers. The electrolyte can be either liquid or solid.
- Membranes: This is also called separator, of which the function is to block the electrons whereas allows protons or hydroxyl ions to pass through.

Other important parts but attract less research interests include water inlet and outlet, gasket, and gas collector.

There are 3 types of electrolysis: alkaline water electrolyser, polymer electrolyte membrane (PEM) electrolyser and solid oxide electrolyser. PEM electrolyser has been very attractive for industrial applications due to its high efficiency and purity of hydrogen production [13]. The cost reduction of state-of-art electrocatalysts for PEM electrolyser remains a challenge.

Fortunately, the PEM electrolyser is now closer to commercial markets due to large amount of effort in cell component research, e.g. membrane [14]. Solid oxide electrolyser is another high efficiency technology which produces highly pure hydrogen. However, this technology faces more technical challenges than PEM electrolyser, for example, it suffers poor stability and degradation [15][16].

Alkaline electrolysis is a mature technology of hydrogen production, of which the cell voltage efficiency is approximately between 52-69%. This efficiency is improving steadily for small and medium-sized electrolysers by applying a catalytic coating on electrodes. It is also important to ensure that the coating would not compromise the lifespan of the electrolyser. Alkaline electrolyser also has advantages over PEM and solid oxide types in its low cost and higher capacities (up to 200 Nm^3/h of H_2) that manufacturers can achieve [12].

The research areas of electrolyser are now focused to achieve a number of goals [17]: (1) reducing operating cell voltage whilst maintaining the current; (2) Long lifespan, allowing the electrolyser to operate for a long period; (3) Low capital cost; (4) Provide balancing for renewable energy generation and compactness. Regardless the type of the electrolysers, scientists tackle these challenges by developing new electrode and catalyst materials that will reduce the energy consumption, therefore the cost for a unit of hydrogen produced.

A very simple example of an alkaline electrolyser is shown in Figure 2. The reaction on each electrode is shown as [18]:

Cathode: $2H_2O + 2e^- \rightarrow H_2 + 2OH^-$ $\quad E^0 = -0.83\ V\ vs\ SHE$ $\quad Equation\ 1$

Anode: $2OH^- \rightarrow H_2O + {}^1/_2\, O_2 + 2e^-$ $\quad E^0 = 0.40\ V\ vs\ SHE$ $\quad Equation\ 2$

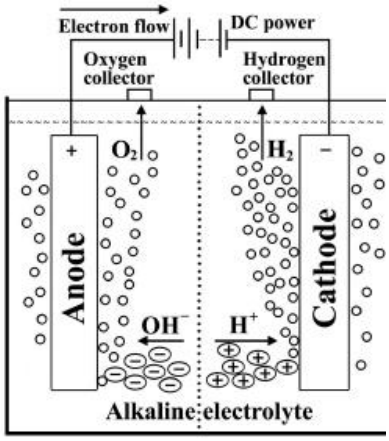

Figure 2. A simple model of an alkaline electrolyser [18].

In alkaline electrolyte, e.g. KOH, the standard cell potential is measured at 25°C at pH 14, when the concentration of OH^- is 1M.

When the electrolyte is acidic, the half reactions at anode and cathode are different from the case when electrolyte is basic. In acidic electrolyte, the half reactions occur at cathode and anode are described by [19]:

Anode: $H_2O \rightarrow {}^1/_2\, O_2 + 2H^+ + 2e^-$ $\quad E^0 = 1.23\, V\ vs\ SHE$ $\qquad Equation\ 3$

Cathode: $2H^+ + 2e^- \rightarrow H_2$ $\quad E^0 = 0.00\, V\ vs\ SHE$ $\qquad Equation\ 4$

Regardless of electrolyte pH, the overall reactions of electrolysis can be written as:

$$H_2O \rightarrow H_2 + {}^1/_2\, O_2 \quad \Delta E^0 = -1.23\, V \qquad Equation\ 5$$

The negative standard potential of Equation 5 indicates that the water electrolysis is unspontaneous reaction and requires external power source to drive the reaction. This standard potential was obtained by the equation $E^0_{cell} = E^0_{cathode} - E^0_{anode}$ = -1.23V. As this value is standard potential of water electrolysis cell, it was measured at 25°C at pH 0, when the concentration of H^+ is 1.0 M at pressure of 1 atm [20].

During operation of an alkaline electrolyser, electricity is supplied to the electrolyser to split water molecules into OH^- and H^+. The proton (H^+) diffuses towards to the cathode, where its reduction reaction takes place, producing hydrogen gas. The reaction at cathode is therefore called hydrogen evolution reaction (HER). Similarly, the OH^- is oxidised at anode, producing oxygen. This reaction is therefore named as oxygen evolution reaction (OER).

1.5 Faraday's Law of Electrolysis

The most important and fundamental laws related to water electrolysis are Faraday's first and second laws of electrolysis. The first law stated that 'the weights of chemical produced at electrodes due to the flow of electrical current during electrolysis are directly proportional to the quantity of electricity passes through the electrolyte [19]. The Faraday's first law of electrolysis can be expressed by:

$$m = \frac{QM}{nF}$$

Where m is mass of the product formed
M is the molar mass of the product formed
Q is the electricity counted in coulomb; this can be calculated by multiplying current by time
n is the number of electrons
F is Faraday constant

The current passes through during electrolysis can be categorised into 2 types, which are named faradic current and non-faradic current. The majority of current is related to the chemical reaction of water electrolysis, whereas small amount of current is not involved in chemical reaction (non-faradic current). The non-faradic current however, tends to be negligible in the case of water electrolysis [19].

1.6 Cell voltage

The overall cell voltage of an alkaline electrolyser cell is consisted of 4 terms, as shown in Equation 6 [21].

$$E_{cell} = E_{rev} + \eta_{cathode} + \eta_{anode} + I \times R_{Ohmic} \qquad Equation\ 6$$

Where E_{rev} is the reversible cell voltage, which is 1.23V at standard condition
ηanode is overpotential at the anode
ηcathode is overpotential at cathode
I is the current and Rohmic is the ohmic resistance of the cell

For water electrolysers used in industries, the cell voltage is commonly within the range of 1.8 to 2.0V, with current density of 300 to 1000 A/m^2 [22].

The cell voltage is also a function of operating temperature of electrolysers. Zhang et al presented a diagram that shows the relationship between cell potential and temperature, this diagram is shown in Figure 3 [23]. There are 3 regions that split up by equilibrium voltage and thermoneutral voltage. The equilibrium voltage reduces as operating temperature increases. If the operating conditions are in the area below equilibrium voltage line, the reaction of water electrolysis would not occur. When the operating conditions are in shaded area, the reaction is endothermic until the cell voltage applied is above the thermoneutral voltage, the reaction then becomes exothermic.

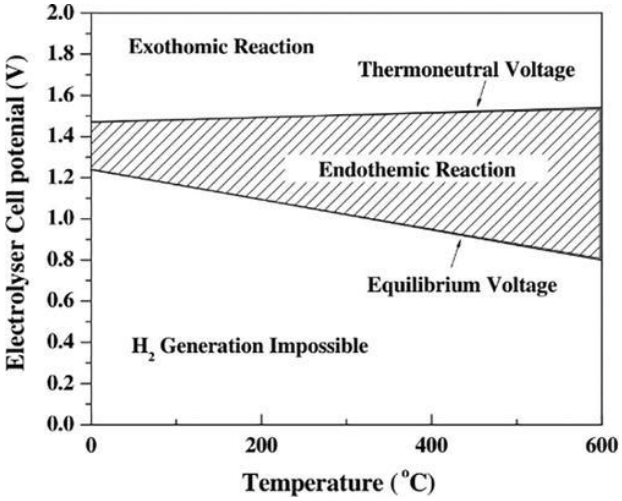

Figure 3. The relationship diagram between cell potential and operating temperature [23].

1.7 Alkaline Electrolyser

The most popular electrolyte used for alkaline electrolyser are sodium or potassium containing positive ions, hydroxide or chloride containing negative ions. During the operation of alkaline electrolysis, water molecules are diffused to cathode due to concentration gradient. Similarly, species with negative ions are diffused to anode. The mass transport of negative ions can also be migration because of the opposite charge attraction.

The electrolyser developed by Clean Power Hydrogen Ltd uses potassium hydroxide as electrolyte, which is a highly conductive electrolyte and caused fewer problems associated with corrosion [24]. Clean Power Hydrogen's specific design of electrolyser is bipolar configuration, that is similar to the schematic diagram shown in Figure 4 [25].

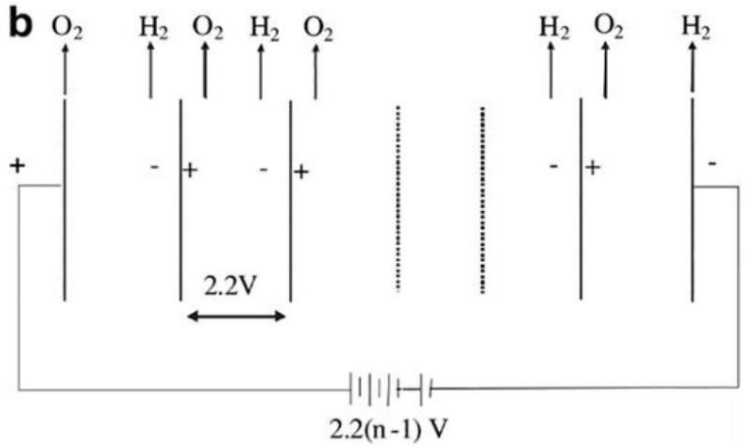

Figure 4. The schematic diagram of bipolar design of electrolyser [25].

For the bipolar design, only the cathode and anode at the end of the whole electrolyser are connected to the DC power source. The electrodes between two electrodes at end act as both anode and cathode on different sides of the plates. The total voltage of the electrolyser unit is 12V, which is split up by individual unit cell. The total current passes through the whole electrolyser equals to that passes through the individual unit cell.

1.8 Oxygen Evolution Reaction

During water splitting process, oxygen evolution reaction has been the main challenge and attracted huge attention because it involves four proton-coupled electron transfers and O-O bond formation that make OER kinetically unfavourable. Like other electrochemical devices, water electrolysis also involves 2 reactions: oxygen evolution reaction (OER) and hydrogen evolution reaction (HER), which take place at anode and cathode, respectively. The efficiency of overall water electrolysis predominantly limited by OER due to it complex mechanisms and energy-demanding intermediate steps. OER, also refers to water oxidation, is a reaction in which one molecule of oxygen is generated by a 4-electron transfer process, each of which increases the complexity and difficulty. In comparison, HER on cathode only involves 2 electrons. Consequently, OER has been identified as thermodynamically unfavourable reaction and contributes a very large overpotential towards overall water electrolysis. Moreover, due to the generation of oxygen, OER potentially is the main reason of electrode breakdown because it can degrade the material structure and cause degenerative performance [26].

In alkaline environment, the hydroxyl groups (OH^-) is oxidised and transformed into H_2O molecules and O_2 molecules, by losing 4 electrons. This reaction is shown in the Equation 7:

$$4OH^- \rightarrow 2H_2O + O_2 + 4e^- \quad E_a^0 = -0.40\,V \;\; vs\,SHE \;\; Equation\,7$$

According to the theoretically proposed models, Equation 1 has been split up into four steps described in Equation 8-11 [27]:

$$4OH^- \rightarrow OH^* + 3OH^- + e^* \quad Equation\,8$$
$$OH^* + 3OH^- \rightarrow O^* + 2OH^- + H_2O + e^- \quad Equation\,9$$
$$O^* + 2OH^- + H_2O \rightarrow OOH^* + OH^- + H_2O + e^- \quad Equation\,10$$
$$OOH^* + OH^- + H_2O \rightarrow O_2 + 2H_2O + e^- \quad Equation\,11$$

Where * represents a surface adsorption site.

Some scientists also suggested that the formation of oxygen could be the direct combination of 2MO without the formation of MOOH intermediate as shown in the Equation 12, which takes place after Equation 9 [28]:

$$2MO \rightarrow 2M + O_2 \quad Equation\,12$$

There is no evidence of which mechanism is the most accurate process describing the formation of oxygen [28]. However, it has been commonly accepted that the catalysis of OER is a heterogeneous reaction where the strength of M-O bonds within the MOH, MO and MOOH that indicate the overall ability of electrocatalysts.

As shown in the equation 7, for each molecule of oxygen produced during the electrolysis, 4 accompanying electrons are produced, along with intermediates of OH^*, O^* and OOH^* produced following each step described in Equation 8-10. The reaction would reduce local pH towards neutral due to the consumption of OH^-. The overall overpotential of OER is related to the energy barriers of each individual step. These steps require electric potential and electron transfer, which are used as energy input, to drive these reactions forward, therefore the efficiency of OER is limited by the step with the highest kinetics barrier, also called the rate-limiting step. Another concept that is becoming more popular is potential determining step [29], which represents the step that has most difference of Gibbs free energy (ΔG). According to the research of Man et al. [30], there is a correlation between the energy barriers of each step described in Equation 8-10 and they called this correlation a scaling relation. In scaling relation, they described that the sum of energies required for the OH*→ O* (Equation 8-9) and O* → OOH* (Equation 9-10) is maintained nearly the same. This sum has a rough value of 3.2 eV [30]. The Figure 5 shows the standard Gibbs free energies of formation of each intermediate at pH=0 and U=0 V vs SHE [30].

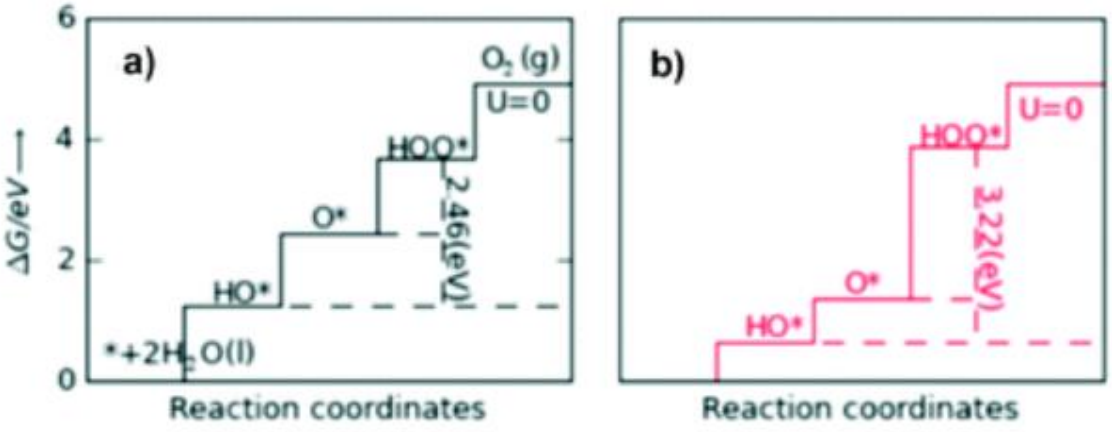

Figure 5. Standard Gibbs free energies of formation of each imtermediate at pH=0 and U=0V. Left: ideal electrocatalyst; Right: $LaMnO_3$ [30].

According to the conclusions made by Man et al. it was expected that the ideal electrocatalyst should provide consistent ΔG value, that was 1.23 eV at each reaction step. However, in real case

the potential determining step has higher ΔG. An example shown in Figure 5 was the $LaMnO_3$ catalyst which had high standard Gibbs free energy change at the step where O^* was transformed to HOO^* [30]. For most types of electrocatalysts, there is a linear relationship between the adsorption energies of intermediates. The relationship can be plotted in volcano plot.

1.8.1 Volcano plot

The work carried out by Man et al. used the sum of energy energy required for the OH*→ O* step and O*→ OOH* step as the descriptor for the OER catalytic activity. This relationship is explained in the volcano plot shown in the Figure 6 [31]. The volcano plot provides the information of binding strength, for example, if the catalyst species bind oxygen too weakly, the reaction of intermediates formation cannot proceed easily, therefore the oxidation of HO^* will be the potential limiting step (in ascending region of the volcano plot). On the other hand, if the binding strength is too strong between species and oxygen, the intermediate become stable and consequently, the formation of HOO^* will be the potential limiting step (on descending region of the volcano plot). As the result, to minimise the kinetically unfavourable reactions of intermediate formation, the ideal electrocatalyst should have neither too weak nor too strong binding strength to O^*. According to the left volcano plot in Figure 6, some best candidates of OER electrocatalysts are NiO, RuO_2, PtO_2, Co_3O_4.

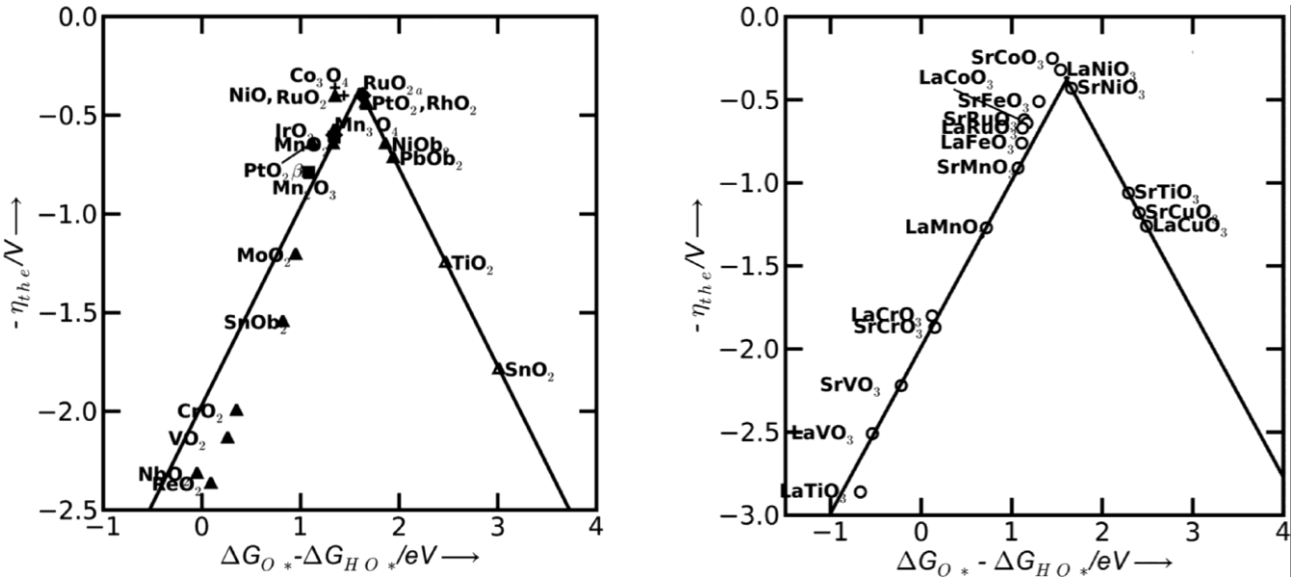

Figure 6. Volcano plots of left: metal oxide catalysts, and right: perovskite [27].

1.9 Requirements for the OER

As the OER proceeds, more electrons will be involved in the reaction and therefore causes accumulation of the energy barrier in each step. Consequently, this will lead excessive overpotential on top of its theoretical potential, which is 1.23V vs reversible hydrogen electrode (RHE) regardless of the pH. To reduce this overpotential, it is vital to develop an appropriate electrocatalysts that satisfy a number of requirements:

(1) **Low overpotential**: The most important parameter is the activity of the catalysts towards OER. High OER activity means that low overpotential that needs overcoming, therefore reduces the energy consumption and efficiency of the electrolysis. Usually, the reference point at which the overpotential is measured and compared is when the current density is 10 mA cm^{-2} [32]. This has been used as benchmark by many researchers to assess the electrochemical performance of the OER activity.

(2) **Good stability:** Another important parameter of OER catalysts is their mechanical and electrochemical stability, as these properties will decide the lifespan of the electrodes. Active site poisoning, corrosion and oxidisation of the catalyst will lower the performance of electrodes and reduce the efficiency of electrolysis. This is also described as electrode breakdown. Zayat et al suggested that a highly stable OER catalysts should show no significant performance loss when operating under 1 A cm-2 for 1000 hours [33].

(3) **Low cost:** Up to now, the best OER catalysts in both acidic and basic environment are believed to be precious metal based such as platinum, ruthenium and iridium oxides. Nowadays it is very challenging to make them commercial due to their high cost despite their high OER activity.

(4) **Earth abundance:** The catalyst materials must be earth-abundant and avoid using rare-earth metals such as perovskites, although they will be potential OER catalysts in future perspective.

(5) **High surface area:** High surface area is the key to boost the catalytic performance because of the exposure of more active sites. The electrochemical catalyst surface area (ECSA) can be calculated from the double-layer capacitance by the equation [34]:

$$ECSA = \frac{C_{DL}}{C_s}$$

Where C_s is the specific capacitance of the electrocatalyst and C_{DL} is double layer capacitance. Oakton et al. developed an IrO_2 electrocatalyst that had surface area of 245 $m^2 g^{-1}$ with particle size between 1-2 nm [35], which can be defined as high surface area. For NiFe based material, Wang et al. defined a high surface area of 250-290 $m^2 g^{-1}$ [36].

(6) **Sufficient pathway:** During electrochemical reaction, it is important to ensure sufficient reactant transfer onto the substrates and fast removal of products, in case of electrolysis, the oxygen bubbles away from substrates. The ideal structure of this catalyst is tunnel-like which provides pathway to reactants and products. The bubble blinding will increase the overpotential.

(7) **Compatibility and wettability of catalysts in electrolyte:** The chemical properties of the catalysts must be considered too. They must not dissolve in the electrolyte and provides good electrolyte penetration.

Unfortunately, the best materials that satisfy all requirements mentioned above have not been discovered yet. Ni-Fe based material is one of the most promising candidates among all materials, in particular, non-precious metal-based materials.

The aforementioned scaling reaction suggests that the sum of energies required for the OH*→ O* and O* → OOH* is maintained the same. For this reason, if the energy required in OH*→ O* step requires relatively low energy, the O* → OOH* step would need higher energy to compensate the difference. This is described in the volcano plot as shown in Figure 6 [27].

As the plot is approaching to the peak, the energies gap between OH*→ O* and O* → OOH* steps is gradually decreasing until the peak of the plot is reached, at which the energies between these steps are identical, which means that the smallest overpotential. As the volcano plot (Figure 6) shown, precious metal-based oxides are all near the peak of the plot. Nickel and cobalt based oxides also have place near the peak.

Dennis A. Corrigan investigated the catalysis of OER by iron impurities in thin film nickel oxide electrodes [37]. In the research, Dennis confirmed that the iron impurities introduced from the electrolyte or co-precipitated into thin film nickel oxide electrodes had strong effects on OER. Even trace amount of iron impurities (as low as 0.01%) would significantly lower the overpotential of OER. More importantly, Dennis concluded that NiFe hydrous oxide with 10-

50% iron into nickel oxide thin films shown promising result as anode electrode materials in alkaline electrolyser.

1.10 Catalysts for the OER

A comprehensive literature review was carried out prior to the commencement of the project in order to fully understand the background knowledge and previous work in relation to the electrode materials for oxygen evolution reaction and hydrogen evolution reaction in alkaline electrolyte, and their synthesis or coating processes. This literature review also aims to provide the history and the evolution of relevant technology, as well as detailing the recent progress that have been made by other researchers with similar objectives. Furthermore, it also includes the current challenges and future prospects of different OER electrocatalysts.

Some key criterion of a commercial standard electrolyser systems is listed in Table 1, where some specifications such as current density, energy consumption, cost and system lifetime can be used as benchmarks to evaluate the performance of the developed alkaline electrolysers which have catalytic coating on electrodes [38].

Specification	Units	Values
Cell temperature	◦C	60-80
Cell pressure	Bar	< 30
Current density	A cm^{-2}	< 0.45
Cell voltage	V	1.8-2.4
Voltage efficiency	%	62-82
Specific system energy consumption	kWh Nm^{-3}	4.2 - 4.8
Minimum partial load	%	10 – 40
Cell area	m^2	3 – 3.6
Hydrogen production per stack	Nm^3 h^{-1}	< 1400
Stack lifetime	kh	55 – 120
System lifetime	Year	20 – 30
Hydrogen purity	%	> 99.8
Cold start-up time	Min	15

Investment costs	Euro kW−1	800 – 1500

Table 1. The performance specification table of standard commercial alkaline electrolyser.

In order to achieve cheaper and more efficient water splitting process, developing the performance of electrocatalysts plays an essential part. Iridium and ruthenium have been investigated by many researchers due to their high OER activity, low overpotential and Tafel slope, and superior stability [39]. Nevertheless, there are some limitations which could counteract their advantages. For example, ruthenium oxide undergoes deactivation in alkaline electrolyte, low abundance of iridium and their high cost [39]. Consequently, with regards to commercial application, the research interest of OER electrocatalysts have been shifted to cheaper, more abundant transition metal catalysts especially in alkaline electrolyte. The most studied and review OER catalysts are categorised as following:

1.9.1 Noble metal materials

Currently, the most studied noble metal materials are iridium (Ir), ruthenium (Ru), palladium (Pd) and platinum (Pt), and their oxides and alloys. It is accepted that their OER activity order, from the highest to the lowest, is Ru > Ir > Pd > Pt [40]. Thus, for the review of noble metal materials in this section, the attention will be paid in mainly Ru and Ir based catalysts.

Many researchers called Ir and Ru state-of-the-art OER electrocatalysts, owing to low overpotential, low Tafel slope and decent stability [41]. Reier et al. investigated and compared the OER activities of bulk and nanoparticle of Ru, Ir and Pt, recoded with 6mV/s scan rate and 1600 rpm in deaerated 0.1 M $HClO_4$ at room temperature [40]. As the Figure 7 demonstrates, the bulk Ru catalyst showed excellent OER activity. However, the study also revealed that Ru showed very low stability, which caused Ru remained a challenging candidate for commercial use.

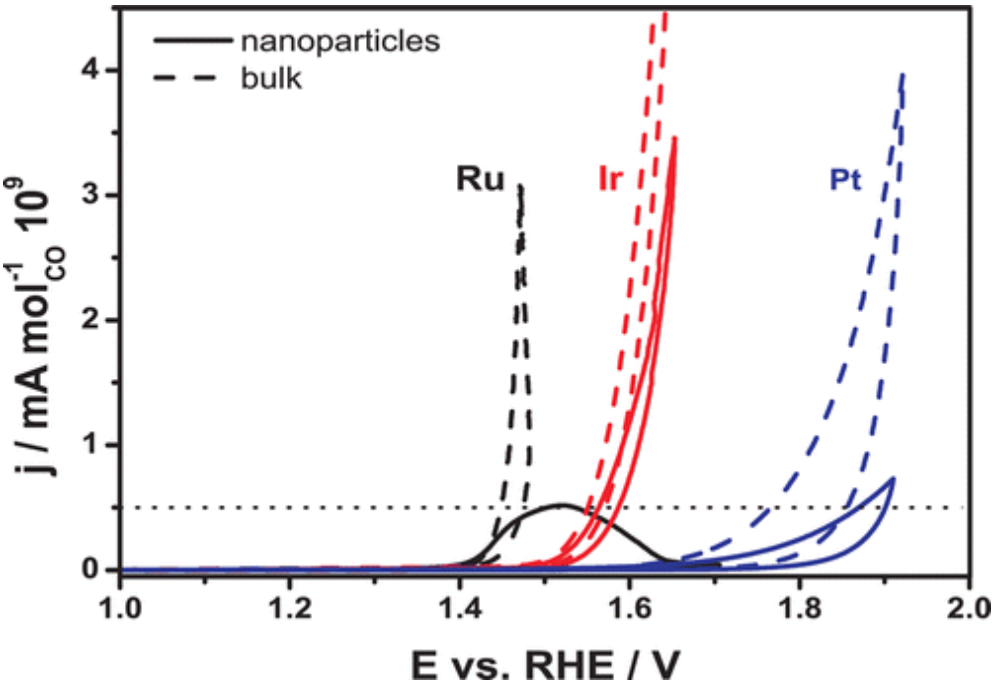

Figure 7. CV scan for bulk and nanoparticle catalysts of Ru, Ir and Pt recorded with scan rate of 6mV/s and 1600 rpm, in deaerated 0.1 M $HClO_4$ [40].

Iridium oxide (IrO_2) and ruthenium oxide (RuO_2) have also been studied by many researchers as they are classified as the most active OER electrocatalysts [42]. Thermodynamically stable rutile iridium oxide (r-IrO_2) and rutile ruthenium oxide (r-RuO_2) nanoparticles have been tested in both acid and basic electrolyte by Lee et al. [43]. The conclusion was that both of them showed very high OER activities, with r-RuO_2 exhibiting up to 10 A/g oxide at 1.48 V vs RHE [43]. After comparing, they found that r-RuO_2 has slightly higher intrinsic and mass specific OER activities than r-IrO_2 in both acid and basic electrolytes.

However, in the long-term operation, Ru will deactivate in both alkaline and acidic electrolyte due to dissolution, which causes very poor stability of RuO_2 as an electrocatalyst [44]. They investigated the stability of noble metal electrodes in alkaline electrolyte. They too found that the OER activity increases as IrO_2 > RuO_2 ≈ Ir > Ru. The Figure 8 presents the amounts of dissolved metals for all four electrodes in 0.05 M NaOH during the anodic scan.

In addition, they also compared the dissolution of metals in acid and base electrolyte and found that the dissolution amounts of noble metal and their oxides are higher in alkaline electrolyte than those in acidic electrolyte. Consequently, the noble metal-based catalyst is less stable in alkaline electrolyte.

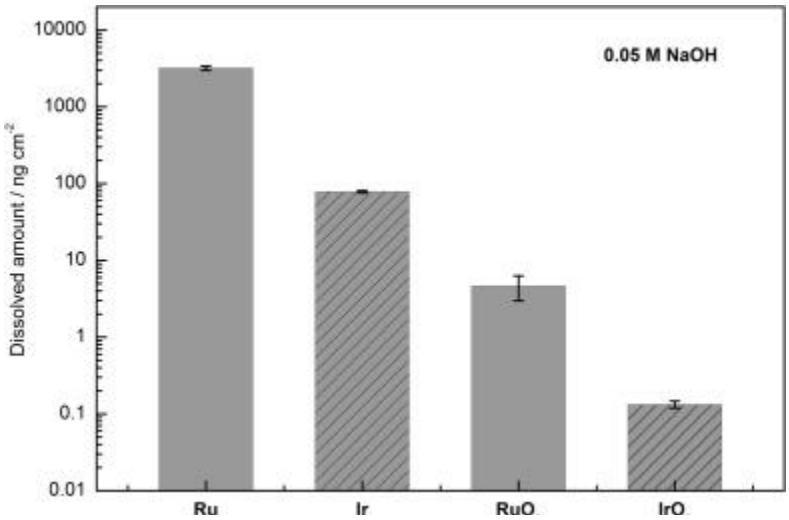

Figure 8. Dissolved amounts of metal from all 4 electrodes during anodic scan, with scan rate of 10 mV/s in 0.05 M NaOH [44].

In conclusion, although IrO_2 and RuO_2 materials exhibit excellent OER activities, their high cost, low abundancy and low stability in both acidic and alkaline electrolyte still prevent them from being ultilised commercially in various applications. For this reason, the development of low-cost and earth-abundant materials are urgently required in order to replace those state-of-the-art electrocatalysts.

1.9.2 Transition metals oxides

1.9.2.1 Cobalt Oxide

Cobalt has various valence states in its oxide (CoO_x), it could be 2^+, 3^+ and 4^+ [41], and therefore it makes cobalt oxide a strong candidate in OER application, in which the phase conversion of Co-based oxides to hydroxides or oxyhydroxides catalysis the OER. Wang et al. fabricated a facile solution reduction method to produced mesoporous Co_3O_4 nanowires treated with $NaBH_4$, creating a high surface area mesoporous structure. Their experiment revealed that the reduced Co_3O_4 nanowires exhibited higher current density at 1.65 V vs RHE than pristine Co_3O_4 nanowires, as showed in Figure 9 [45].

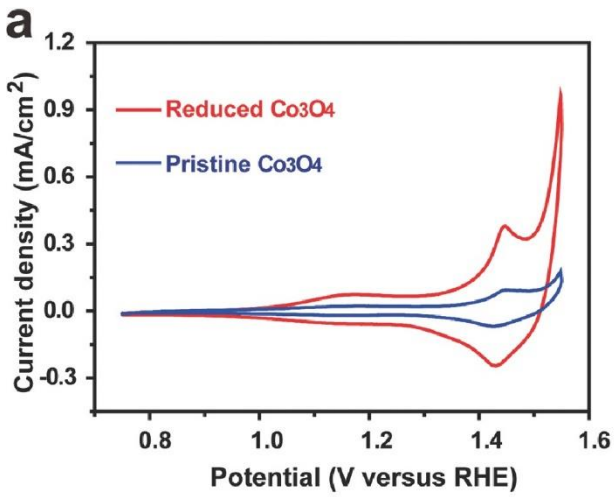

Figure 9. CV of the pristine Co_3O_4 and reduced Co_3O_4 nanowires on glassy carbon electrodes in 1 M KOH at 5 mV s^{-1}, performed by Wang et al [45].

The experiment performed by Want et al. explained that the degree of OER activity improved by Co_3O_4 was associated with its surface area and morphology. Furthermore, the mixed valence states of cobalt provide oxygen vacancies which enhances the electrical conductivity. Similarly, Xu at el. also investigated the relationship between Co^{2+}/Co^{3+} ratio in Co_3O_4 and OER activity by fabricating plasma engraved Co_3O_4 nanosheets [46]. They concluded that the engraved Co_3O_4 exhibited lower onset potential and 10 times higher OER activity than that of pristine Co_3O_4, owing to the increased surface oxygen vacancies. This was achieved by optimal tuning of Co^{2+}/Co^{3+} ratio and therefore the electronic structures and catalytic properties were optimised. In addition, they found that Co^{2+} plays more vital and active role than Co^{3+} in facilitating OER [46]. Later on, Want et al. agreed this conclusion by studying both Co^{2+} and Co^{3+} [47]. According to their studies, Co_3O_4 has a spinel structure with Co^{2+} in the tetrahedral site (Co^{2+}Td) and Co^{3+} in octahedral site (Co^{3+}Oh) of the cubic molecular structure showed in the Figure 10 [48].

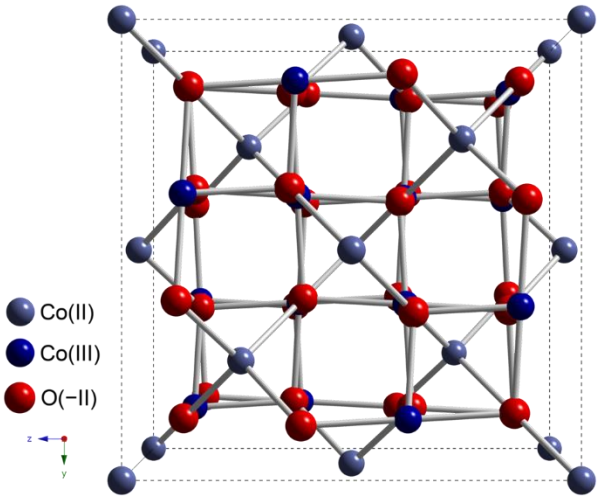

Figure 10. For the above images on the left and right are coordination geometry of Co^{2+} and Co^{3+}, respectively. The image below is the molecular structure of spinel cobalt oxide, Co_3O_4 [48].

The X-ray absorption results identified that it was Co^{2+} that was responsible for the OER active CoOOH formation. Want et al. further explained that Co^{2+} in spinel Co_3O_4 could release electrons and promote the affinity to oxygen ions to form CoOOH. As spinel Co_3O_4 contained Co^{2+} and Co^{3+}, the reaction process of Co_3O_4 production is referred to disproportionation, which means that the product contains same element but different oxidation states, whereas the reactant (raw material) contains only one oxidation state.

1.9.2.2 Nickel Oxide

NiO exhibits the highest OER activity among all transition metal oxides, for which it has attracted much attention in applications of supercapacitor electrodes and electrocatalysts in alkaline electrolyte [49]. Researchers have devoted to increase the electrocatalytic performance of Ni-based electrocatalysts by tuning its nanostructure which enables more active sites to participate the OER. It has been accepted that NiO lies on the electrode surface layer by layer, and its outermost layer is covered by $Ni(OH)_2$ that is in contact with the electrolyte [50]. More precisely, the initial form of $Ni(OH)_2$ is α-$Ni(OH)_2$. During potential cycling, the transformation of α-Ni(OH)2 occurs and results in the formation of β-Ni(OH)2 and β-Ni(OOH). As the potential cycling continues, the outer layer of $Ni(OH)_2$ further grows and subsequently form γ-NiOOH. This entire process is presented in the Bode diagram (Figure 11) [51].

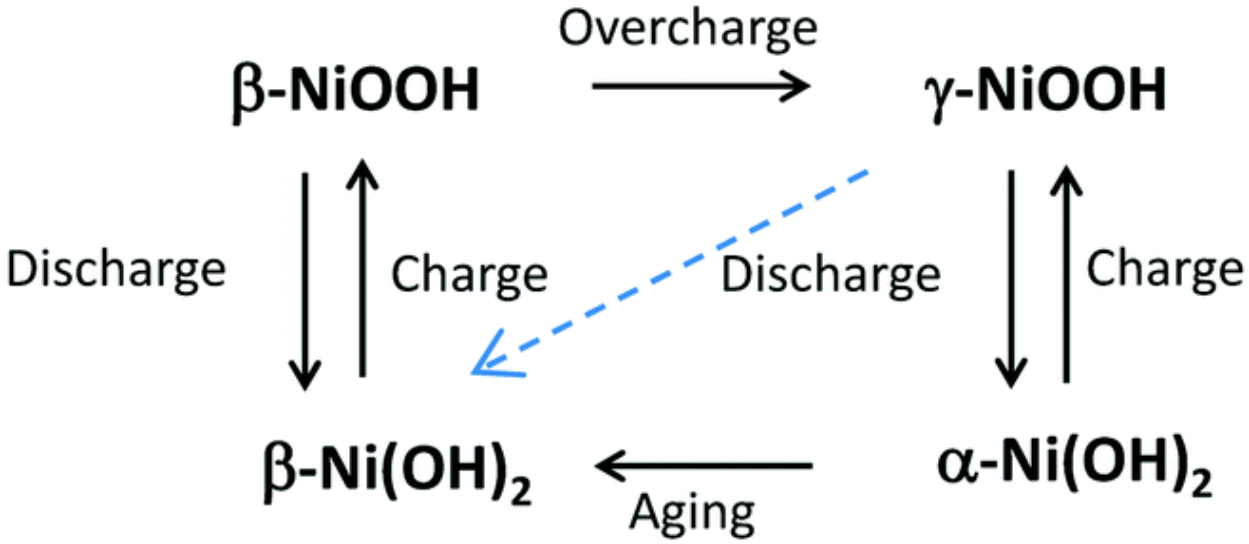

Figure 11. Bode diagram of $Ni(OH)_2$ redox transformation [51].

The γ-NiOOH is believed to be responsible for enhanced OER because it contains higher oxidation state of $Ni^{3+}$and Ni^{4+} [41] [50], which is very active for OER.

Consequently, many studies related to Ni-based catalysts have been focused on the formation of higher oxidation states of Ni as well as decent crystal structures of NiO [41]. As for specific examples, Fominykh et al. fabricated ultrasmall dispersible crystalline NiO nanoparticles by solvothermal reaction with nanocrystal sizes tunable between 2.5 to 5 nm [52]. They concluded that the nanoparticles of 3.3 nm demonstrated high turnover frequency of 0.29 S^{-1} at an overpotential of 300 mV for oxygen evolution reaction. Furthermore, due to its high crystallinity

and dispersibility, this nanoscaled NiO could be deposited on temperature sensitive susbtrates such as polymers without heat treatment [52].

The doping of another metal, particularly Fe, would result in significant enhancement towards the OER activity of NiO. This will be discussed later on in the "spinel-type oxides" section.

1.9.2.3 Manganese Oxide

Manganese oxide has also drawn some attention in the application of electrocatalyst although it is slightly less efficient compared to Ni and Co based oxides. Its OER activity strongly depends on their crystal structures, morphologies and pore structures [41]. Bergmann et al. constructed an atomic scale structure-activity relationship of two different nano-structured manganese oxides, MnOx. One was prepared by chemical symproportionation (s-MnOx) and the other one was prepared by impregnation (i-MnOx) [53]. The s-MnOx was consisted of a layered structure whereas the i-MnOx was consisted of a mixture of tunneled, 3D cross-linked structure. The experimental results revealed that the layered structure exhibited large Tafel slope and high intrinsic OER activity. In contrast, the 3D cross-linked structure exhibited small Tafel slope but low intrinsic OER activity [53]. Their findings inspired many researchers to investigate the so-called structure-activity relationship and provided guidelines to design and control the structural engineering of non-precious transition metal oxides as a highly active OER electrocatalyst. Lian et al. fabricated a mesoporous manganese oxide via hydrothermal template-free synthesis. They used porous manganese carbonate as a precursor, which was subsequently annealed at different temperatures between 450 – 575 °C [54]. The MnOx obtained at 380 °C and 450 °C had very high specific surface area which was the cause of high OER activity. When the annealing temperature of precursor was 450 °C, they obtained an overpotential of 427 ± 10 mV at a current density of 10 mA cm^{-2}, which was the optimum condition in this case. Huynh revealed that MnOx prepared by constant anodic potential deposition shown modest OER activity and could be improved by activating the MnOx film by potential cycling. This was the result of the formation of disordered birnessite phase during oxygen evolution reaction [55].

1.9.3 Mixed metal oxides (AB_xO_y)

Almost all reviews suggested that the mixed metal oxides exhibited better OER activity than single metal oxides alone. For example, cobaltite spinel $MxCo_{3-x}O_4$, where M could be Ni, Cu, Zn, and Mn. The strategy of mixed metal oxides was designed to improve the OER performance by either

optimising the adsorption energies. This is done by developing materials that are close to the peak of volcano plot as possible.

1.9.3.1 Spinel type oxides

Spinel type oxides have structure of AB_2O_4, where both A and B are metals. Typically, cation A has charge of 2^+ at tetrahedral sites and cation B has charge of 3^+ at octahedral sites. For example, cobaltite spinel oxides include $NiCo_2O_4$, $ZnCo_2O_4$ and $MnCo_2O_4$. Figure 12 is the

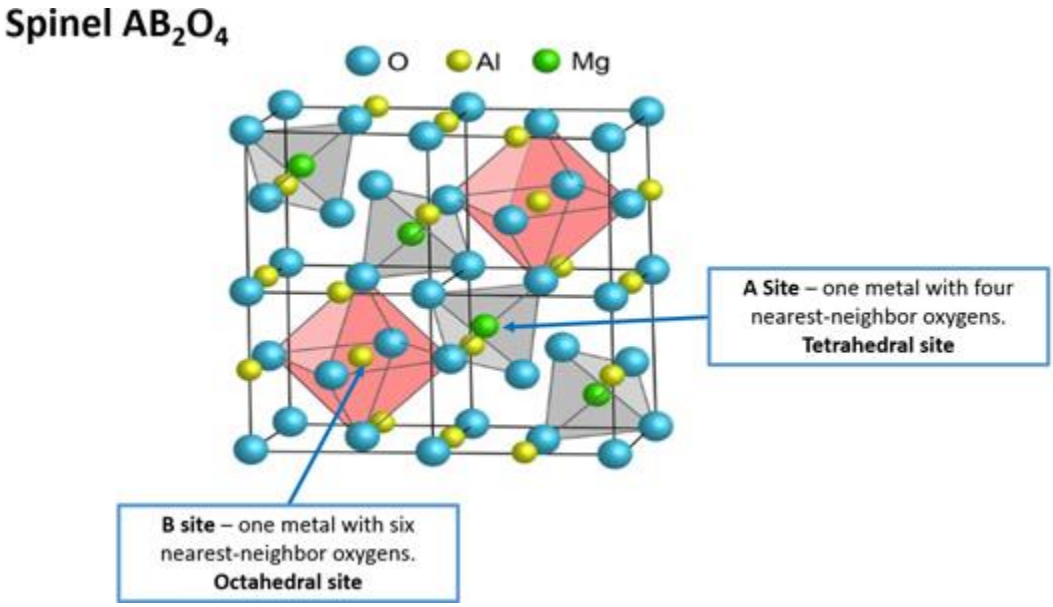

Figure 12. An example molecular structure of $MgAl_2O_4$ spinel [56].

example of $MgAl_2O_4$ spinel structure, where the Mg^{2+} cations and Al^{3+} cations sit at tetrahedral and octahedral sites, respectively.

Among all spinel oxides, $NiCo_2O_4$ with various nanostructures have attracted much attention due to its decent electrical conductivity and OER activity [41]. Li et al. fabricated a $Ni_xCo_{3-x}O_4$ nanowire arrays (NW) on Ti foil and compared its electrocatalytic activity with pure Co_3O_4. The resulted substrate could be directly used as the anode in water splitting process. They found that the introduction of Ni dopants to cobalt oxide enhanced the OER activity due to the improvement of their physical properties such as roughness factor, electrical conductivity and active site density. Furthermore, the nanowire arrays structure provides open space to active reactants and products and the direct contact between NWs and conductive Ti foil ensures each NW to participate in the reaction and direct use in the electrochemical cells [57]. Similarly, Jin et al. synthesised a functional catalyst of $NiCo_2O_4$ spinel nanowire arrays by

template-free co-precipitation route. They too concluded that the mesoporous nanowire morphology had advantage in increasing the specific surface area and was responsible for the enhanced OER activity [58]. Chen et al. fabricated a three-dimensional $NiCo_2O_4$ core-shell nanowire made up of $NiCo_2O_4$ nanowire core and $NiCo_2O_4$ nanoflake shell on conductive carbon cloth substrates with combination advantages of high surface area, enhanced mass and charge transport and conductivity. The electrochemical test exhibited only 320 mV overpotential at a current density of 10 mA cm^{-2} [59]. A core-ring structured $NiCo_2O_4$ synthesised by Cui et al. also exhibited great electrocatalytic properties, with an overpotential of 315 mV at current density of 100 mA cm^{-2} [60]. Shi et al. performed morphological study by investigating the OER activity on spinel $NiCo_2O_4$ nanoneedles (NNs) and nanosheets (NSs) by solvothermal processes. The preparation procedures were almost same except DMF and ethanol solvents were used to form nanoneedles and nanosheets, respectively [61]. By using different solvents, different Ni/Co ratios were also achieved. They found that the onset potential of OER on $NiCo_2O_4$ NNs and NSs were 365 mV and 415 mV, respectively [61]. The NNs exhibited superior activity due to its efficient electron transfer tunnel and large surface area. Furthermore, they suggested that the surface of $NiCo_2O_4$ NNs was better hydroxylated and easy to adsorb water molecules. Therefore they believed that the hydroxylated surface indicated the presence of $M(OH)_2$ or MOOH, where M could be Co and Ni that was favorable for water splitting [61].

Apart from nickel based cobaltites, other transition metals can also combine with Co_3O_4 spinel that form good OER catalysts. Tan et al. synthesised cobaltites $M_xCo_{3-x}O_4$ (M = Ni, Cu, Zn, Mn; x = 1 or 0.9) by co-precipitation method and studied their OER performance in 1M KOH at room temperature [62]. They compared the electrocatalytic properties with the bare nickel electrode. The results (Figure 13) showed that all cobaltite spinel catalysts exhibited higher OER activities with $ZnCo_2O_4$ and $Cu_{0.9}Co_{2.1}O_4$ outperformed $NiCo_2O_4$ and $MnCo_2O_4$. In addition, they all exhibited high stability at 100 mA cm^{-2} in 1 M KOH (Figure 14) [62]. They also discovered that the amount of surface Co cations occupying the octahedral sites (Co^{3+}) is the key for OER performance.

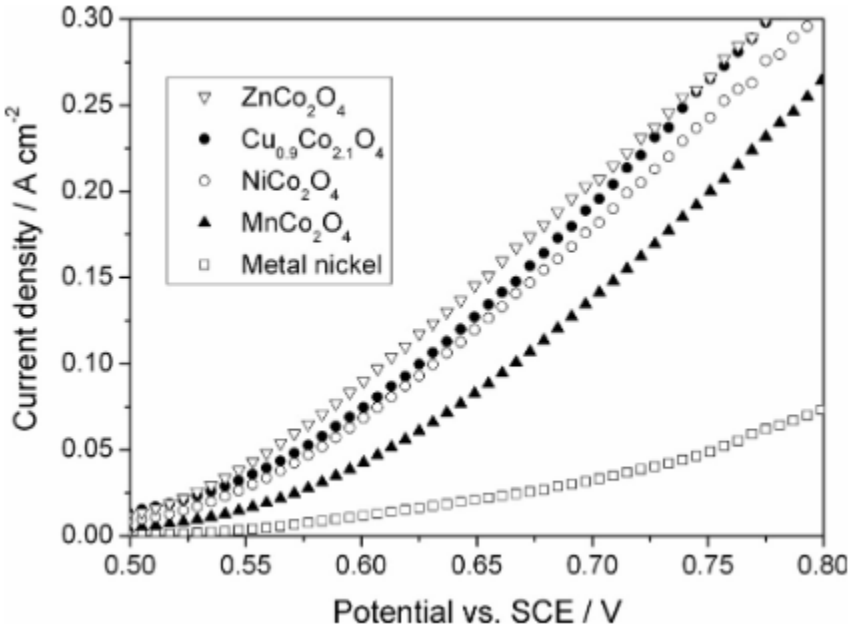

Figure 13. Polarisation curve of cobaltites and metal electrode [62].

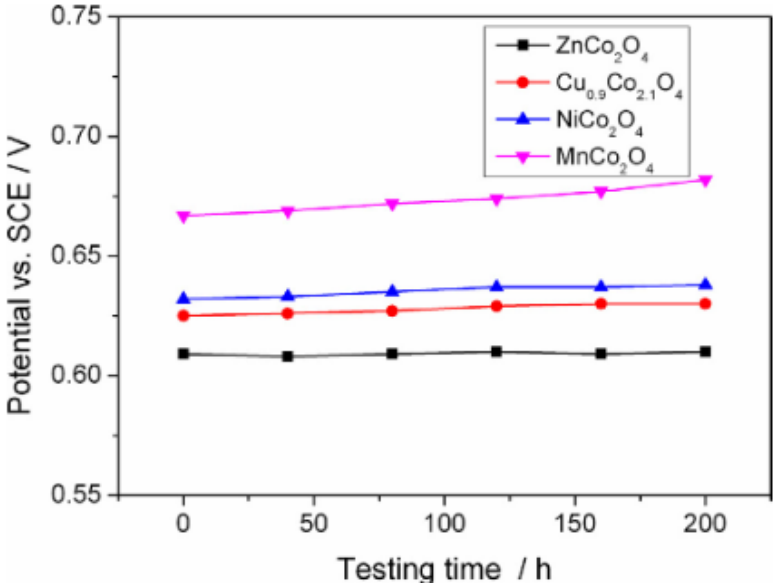

Figure 14. Stability test of cobaltites in 1M KOH [62].

On top of the above conclusion, researchers investigated the role of Zn in its role of improving OER. The incorporated Zn into Co_3O_4 replaces the Co^{2+} in tetrahedral sites and their state of Co^{3+} in octahedral sites remains the same. Therefore any difference in OER performances of Co_3O_4 and $Zn_xCo_{3-x}O_4$ must be caused by the differences in electronic and structural nature of substituted tetrahedral sites [27]. Kim et al produced a high-quality thin film of spinel $ZnCo_2O_4$ that contains only Co^{3+} in octahedral sites. By comparing the catalytic properties of $ZnCo_2O_4$ and Co_3O_4, they found that $ZnCo_2O_4$ exhibited slightly higher activity than Co_3O_4, which was the evidence that the Co^{2+} at tetrahedral sites are catalytically inactive for OER [63]. Menezes et al. further compared the properties of $ZnCo_2O_4$ and Co_3O_4 and concluded that the higher activity of $ZnCo_2O_4$ over Co_3O_4 was resulted by the defective tetrahedral sites and higher fraction of available Co^{3+} at octahedral sites. Therefore the authors believed that it was the Co^{3+} that mainly caused the improved OER activity. When Co^{3+} is oxidised to Co^{4+} during OER, the O adsorbate attached to Co^{4+} and forms an O-O bond due to large electronegativity [27].

1.9.3.2 Perovskites

Perovskites have a common formula of ABO_x as the Figure 15 shows, where A cation is alkaline-earth or rare-earth metals and B cation is transition metals [64]. Perovskites are strong candidates for OER electrocatalysts because their structural stability and flexibility because the A and B cations can partially be substituted by additional elements of different valences and sizes, as well as their tenability of composition [65].

As the Figure 15 shows, A cations are bigger and B cations are smaller. Usually, cation A is any of lanthanide, alkaline or alkaline-earth metal and cation B is transition metals with 3d, 4d or 5d

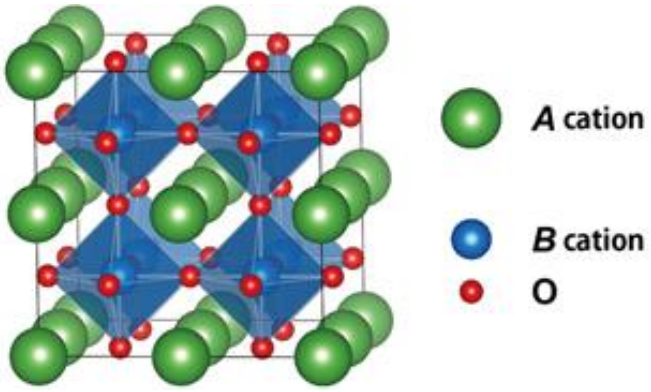

Figure 15. Molecular structure of a perovskite.

configuration [65]. Cation A and oxygen atoms have a cubic structure with cation B resides in the

centre of the octahedral cage. As mentioned above, one of perovskites advantages is its tunability of composition. Substitution of A cation would affect its oxygen sorption ability and substitution of B cation would affect the reactivity of the sorbed oxygen [65]. So far, the most promising perovskite was $Ba_{0.5}Sr_{0.5}Co_{0.8}Fe_{0.2}O_{3-\delta}$ (BSCF) fabricated by Suntivich et al., who thereafter developed the vocalno plot for all perovskites he/she studied [111].

1.9.4 Layered double hydroxide

Layered double hydroxide has been a popular candidate of OER catalyst because of its structure. They contain cationic brucite like layers separated by intercalates of which the charge is balanced by metal cations [66]. An example of LDH is shown in the Figure 16. LDH has a layered structure of divalent and trivalent metal hydroxides, separated by intercalated anions such as CO_3^{2-}, NO^{3-}, SO_4^{2-} and etc. Owing to its unique structure, LDH allows fast reactants and products diffusion as well as electron transfer [66]. As the result, the OER active sites easily become available.

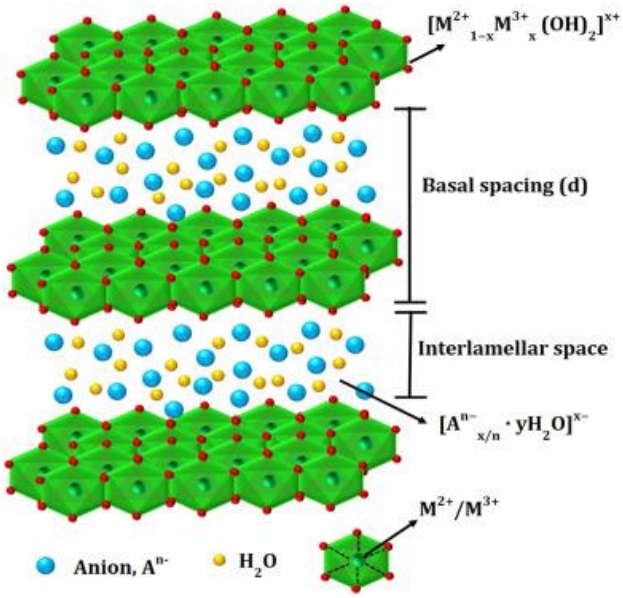

Figure 16. An example of LDH molecular structure [66].

.

The important parameters of LDH synthesis are ratio of M^{2+}/M^{3+} and basal spacing (d), which could be controlled by exfoliation method. Many researchers are working on the optimisation of LDH synthesis and structure design. So far, the OER activity ranking of most LDH in terms of activity is NiFe > NiCo > CoCo [67].

1.11 Key performance indicators for OER catalysts

To deeply evaluate electrocatalyst materials for OER, several key performance indicators are identified to create fair comparison and evaluation. They are listed below with their thorough explanations.

1.11.1 Overpotential

Overpotential is one of the most convictive indicators to evaluate the activity of certain catalysts. Although it has been accepted that the thermodynamic equilibrium potential for water oxidation is 1.23V for a single cell, a lot higher potential should be applied in reality to achieve the same result because of the electrode kinetics barriers. The difference between applied potential and thermodynamically equilibrium potential (1.23V) is defined as overpotential under specific current density. This value is usually measured in mV. A lower overpotential usually indicates better electrocatalyst activity for a certain electrochemical reaction. These values are also difficult to be measured, therefore many researchers used 10 mA cm^{-2} as a reference current density at which the overpotential of many electrocatalyst materials are measured and compared [32]. The values of overpotential are different at different current density, therefore when comparing the overpotential of an electrocatalyst, the current density at which the overpotential was measured must be mentioned.

1.11.2 Tafel slope

Tafel slop is a useful tool to understand the reaction kinetics and a performance indicator to compare how well the electrocatalysts perform for a reaction. Tafel equation relates the rate of an electrochemical reaction to the overpotential. Tafel equation is a simplified form of the Butler-Volmer equation, which is shown in Equation 13:

$$i = Ai_0 \left[exp\left(\frac{\alpha_a nF\left(E - E_{eq}\right)}{RT}\right) - exp\frac{\alpha_c nF\left(E - E_{eq}\right)}{RT}\right] \quad Equation\ 13$$

Where:

- i = electrode current, A
- A = electrode active surface area, m2
- io = exchange current density, A/m2
- E = applied electrode potential, V
- Eeq = equilibrium potential, V
- T = absolute temperature, K
- n = number of electrons involved in the electrode reaction
- F = Faraday constant
- R = universial gas constant

- α = symmetry factor or charge transfer coefficient, dimensionless

For the OER, only anodic overpotential was applied to the system, therefore the overall current is predominantly attributed to the anode side. Consequently, the cathodic term of the Butler-Volmer equation is vanishingly small. The overpotential term (E-Eeq) can be replaced by symbol η. Thus, the Equation 13 becomes:

$$i = Ai_0 exp\frac{\alpha_a nF\eta}{RT} \quad Equation\ 14$$

To express the Tafel slope, the Equation 14 is re-written as:

$$\eta = b \cdot \log\left({}^{i}/_{i_o}\right) \quad Equation\ 15$$

Where b denotes the Tafel slope.
From Equation 15, it can be understood that the Tafel slope tells how fast the current will increase and how sensitive the current will respond with overpotential. In terms of Tafel slope, a good electrocatalyst is defined as having smaller Tafel slope because that indicates the current density increases faster with even small change of overpotential, as Figure 17 explains. In the figure [32], catalyst b1 has a steeper Tafel slope than catalyst b2. When the overpotential (y-axis) increases, the current density of b2 increases more than b1 (x-axis). Therefore it can be concluded that the catalyst b2 exhibits more sensitive response to change of overpotential than b1 and the reaction kinetics of b2 is faster than b1. As the result, b2 outperforms b1.

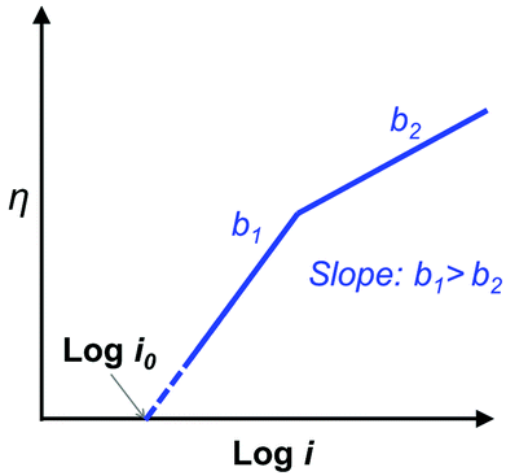

Figure 17. This is an example of Tafel equation. There are 2 Tafel slopes, b1 and b2, involved in comparison [32].

1.11.3 Exchange current density

From the Tafel equation, exchange current density (i_0) can be obtained, which is another important factor to consider in order to evaluate electrocatalysts. Exchange current density is a small amount of current in the condition where the overpotential is 0. When the overpotential is 0, the anodic current and cathodic current are balanced by each other, however the electron transfer process continues occurring, resulting in the exchange current. It can be also defined as the current density that flows equally in equilibrium and in both directions. The forward and reverse reactions proceed at equal rates means that reaction occurs in both forward and reverse directions with zero net current reaction rate (the system is at equilibrium state). This rate is the exchange current density. The larger the exchange current density, the better electrocatalysts because the reaction is faster. The exchange current density can only be obtained experimentally by extrapolating the Tafel slope. The interception of Tafel slope and the line where the overpotential equals 0 is the value of log (i_0).

1.11.4 Stability

The stability is a vital property to determine whether the electrocatalysts are commercially valuable. Only those being able to work for long term can be employed in real electrochemical devices. In this study, the stability was mainly studied via chronoamperometry technique, where a fixed potential of 1.2 V vs SCE is applied to the working electrodes for 60 hours. The current density was measured, and the percentage of peak currents difference was calculated.

The desired performance metrics with values are listed in Table 2.

Performance metrics	Values
Current density	0.3 – 0.4V at 10 mA cm^{-2} [68]
Stability	No performance loss when operating at 1 A cm^{-2} for 1000 hours [33]

Table 2. Desired performance metrics of a good electrocatalyst.

1.12 Aims and objectives for the thesis

This thesis contains the experiments carried out at Lancaster University which intended to improve the OER of an alkaline electrolysis device owned by Clean Power Hydrogen Ltd (CPH2), by applying a catalytic coating that is satisfied with requirements mentioned in section 1.7. CPH2's current electrolyser could achieve a high electrical efficiency up to 73% under optimised operation conditions. The main aims of this project are: (1) developing an earth-abundant and non – expensive materials for improved OER in alkaline media. (2) designing experiments to make those materials grow on stainless steel substrates without using any chemical binder. (3) analysing their morphologies and electrochemical properties. (4) giving recommendations for commercial production of catalyst – coated substrates, and suggestions to future work. In CPH2's perspective, the main expectation from this research is improving the electrical efficiency of their alkaline electrolyser by another 10%.

As a summary of literature review, nickel based electrocatalysts are very promising because nickel is an earth-abundant metal and the cost of nickel is relatively low compared to noble metal-based catalysts. According to the volcano plot shown above, nickel oxide was positioned very close to the peak of the plot along with RuO_2 and IrO_2, which meant that nickel oxide would have neither too strong nor too weak binding strength to O*, thus lower OER overpotential. Furthermore, many researchers found that when iron impurities were introduced to the nickel-based materials, the electrochemical activity was even more improved and higher than nickel oxide alone. The early discovery of this was done by Tichenor et al [69], who concluded that the existence of foreign ion (Fe) could increase the electrochemical activity of nickel oxide electrodes in potassium hydroxide electrolyte. Corrigan et al. also discovered that when the iron was present in electrolyte it could also improve the OER activity of nickel hydroxide thin film [37]. Thus, nickel-based materials were selected as good candidates at the early stage of catalytic coating development of anode material for Clean Power Hydrogen Ltd's electrolysers.

2. Materials and Methods

This section outlines the preparation procedures of NiFe based catalytic materials via electrodeposition or thermal deposition on stainless steel 316 substrates, including raw materials used, experimental parameters and equipment used.

All experiments were designed for different purposes. Of four experiments, Experiment 1 investigated the pH effect on the chemical properties and electrochemical performance to improve OER of electrodeposited NiFe thin films. Nickel sulphate and iron sulphate were used as salts of the deposition solution mainly because of their low cost. Furthermore, the sulphate ion is very weak oxidising agent, therefore the deposition potential would have minimum impact on sulphate anions and film properties.

Experiment 2 aimed to find out how differences in deposition chemistry would affect the properties and electrochemical performance of catalytic film by replacing nickel sulphate and iron sulphate with nickel nitrate and iron nitrate. The pH effect was not considered in this experiment. Many researchers such as Louie et al suggested that the optimum Ni/Fe ratio in a NiFe oxdie OER catalyst is between 10 – 50 mol% [70], therefore attempts were made in Experiment 2 to change Ni/Fe ratio in deposition solution in order to discover the ratio with the best performance in terms of OER reaction kinetics. Furthermore, the deposition potential was another variable that was changed in the experiment to investigate if low potential can be used to generate good performing catalytic layer. This would be useful to know especially for manufacturing of coated electrodes for commercial use because the manufacturing cost can be reduced by less energy consumption.

Experiment 3 was inspired by Wei et al. [71], where they developed Fe-doped nickel hydroxide. Compared to Experiment 1 and 2, both of which were single – step process, Experiment 3 consisted of three steps, where the Fe was doped as impurity into $Ni/Ni(OH)_2$ rather than simultaneously depositing Ni and Fe hydroxide via one-step electrodeposition. Researchers such as Ioannis Spanos investigated the effect of Fe impurities on transition metal catalysts for OER and summarised that only small amount of Fe impurity would enhance the OER activity of Ni based catalysts significantly [72]. One hypothesis made was that one-step electrodeposition of NiFe hydroxide would result in high loading of Fe, which may hinder Ni active sites to participate OER. Therefore Experiment 3 was designed to study if doping small amount of Fe impurity to Ni

based material would improve the OER further. It also helps understand future design of Fe-doped Ni catalysts of similar type.

Experiment 4 was the development of NiFe layered double hydroxide (LDH), which has been reported as one of the most efficient OER electrocatalysts by many researchers, according to the literature review section of the thesis. The experiment performed in Experiment 4 was only an early stage of synthesising this material, substantial amount of effort is required to develop the materials and optimise experiment conditions. However, the conclusions of Experiment 4 were still useful for comparison purpose with Experiment 1 – 3.

The morphologies of all electrode samples were characterised by scanning electron microscopy (SEM – JOEL JSM – 7800F).

2.1 Materials and procedures

Nickel sulphate ($NiSO_4 \cdot 6H_2O$, ≥ 98.0% ACS reagent, Sigma-Aldrich), iron sulphate ($FeSO_4 \cdot 7H_2O$, ≥ 99.0% ACS reagent, Sigma-Aldrich), sodium sulphate (Na_2SO_4, ≥ 99.0%, anhydrous granular, Sigma-Aldrich), 1M sulphuric acid (H_2SO_4, 99.999%, Sigma-Aldrich). Nickel nitrate ($Ni(NO_3)_2 \cdot 6H_2O$, 98%, Alfa Aesar), iron nitrate ($Fe(NO_3)_3 \cdot 9H_2O$, ≥ 98%, Alfa Aesar), potassium nitrate (KNO_3, 99%, Alfa Aesar). Nickel chloride ($NiCl_2 \cdot 6H2O$, 98%, Alfa Aesar), ammonium chloride (NH_4Cl, ≥ 99.5%, Sigma-Aldrich), sodium chloride (NaCl, 99.99%, Alfa Aesar), ethylene glycol ($C_2H_6O_2$, 99%, Alfa Aesar), iron sulphate ($FeSO_4 \cdot 7H_2O$, ≥ 99.0% ACS reagent, Sigma-Aldrich). urea ($CO(NH_2)_2$, Sigma-Aldrich), ammonium fluoride (NH_4F, 96%, Alfa Aesar).

2.2 Experimental procedures

Experiment 1: Electrodeposition of NiFe alloy and hydroxides

In Experiment 1, the NiFe alloy and hydroxide was fabricated by adjusting pH of the precursor solution. The precursor solution was prepared by mixing 0.025M $NiSO_4 \cdot 6H_2O$, 0.025M $FeSO_4 \cdot 7H_2O$ and 0.1M Na_2SO_4 in deionised water. The pH of the solution was adjusted to 2 by adding 1M sulphuric acid dropwise under continuous stirring. A piece of 1.4 cm x 2 cm stainless steel 316 (SS316) was rinsed by deionised water and sonicated for 30 minutes. The SS316 sample

was used as cathode during electrodeposition process. The deposition of NiFe thin film was completed in a 3-electrode system, where SS316, saturated calomel electrode and platinum wire were used as working, reference and counter electrodes, respectively. A constant potential of -1.3V was applied by potentiostat (Ivium Compactstat – Ivium Technologies, Netherlands). The deposition time was 300 seconds.

For the acidic condition of the electrodeposition process, pH of 2 was used because the when the first few drops of 1M sulphuric acid was added to the mixture of $NiSO_4 \cdot 6H_2O$ and $FeSO_4 \cdot 7H_2O$, the solution pH quickly dropped to ~2. Continuation of further acid addition only resulted in very small pH drop, therefore pH 2 was the best acidic condition in this experiment without significantly affecting the overall concentration of $NiSO_4 \cdot 6H_2O$ and $FeSO_4 \cdot 7H_2O$.

The entire procedures were repeated with varied precursor concentration, deposition time and pH. The details of 5 samples prepared are shown in the Table 3.

Sample number	Precursor concentration (M)	pH of the precursor solution	Deposition time (seconds)	Deposition potential (V vs SCE)
1	0.025	2	300	-1.3V
2	0.025	2	500	-1.3V
3	0.05	2	300	-1.3V
4	0.05	2	500	-1.3V
5	0.025	4.2	300	-1.3V

Table 3. Experimental conditions of electrodes preparation in Experiment 1.

Experiment 2: Electrodeposition of hierarchical NiFe hydroxides

For hierarchical NiFe hydroxide coatings, the precursor solution was prepared by adding total amount of 0.05M metal salts with varied ratio of Ni:Fe (1:1, 3:1, 6:1 and 9:1). 0.1M KNO_3 was added as supporting electrolyte. Pieces of 1.4 cm x 2 cm SS316 were rinsed by deionised water and sonicated for 30 minutes prior to the deposition. The deposition time was 300 seconds. To investigate the effect of deposition potential, -1.3 V and -1.0 V vs SCE were applied. Based on the cyclic voltammogram of nickel nitrate and iron nitrate reduction, -1.0V vs SCE was appropriate because this is slightly more negative than the individual reduction potential of $Ni^{2+} \rightarrow Ni$ and $Fe^{2+} \rightarrow Fe$. The reduction potential of -1.3V vs SCE was used to compare with the morphologies and electrochemical performance of electrodes prepared in Experiment 1. The electrodeposition time of 300 seconds was used for all electrode samples prepared in this experiment.

Experiment 3: Doping of Fe on electrodeposited metallic Ni/Ni hydroxide in organic solvent

The experiment 3 contains 3 steps:

(1) Deposition of Ni: The deposition of nickel on stainless steel was performed by electrodeposition in a 3-electrode system, where the precursor solution contained 0.1M $NiCl_2$, 0.5M NH_4Cl and 2M NaCl. The potential of -1.0V vs SCE was applied to the working electrode for 200 seconds, where the working electrode was a piece of 1.4 cm x 2 cm SS316 of which the cleaning procedures were the same as described in experiment 1.

(2) Formation of nickel hydroxide by using deionised water: After the step 1, the substrate was rinsed by deionised water multiple times and was left to dry naturally in the air. After drying, the substrate was submerged in 50 ml deionised water in a PTFE Teflon reaction vessel. Then, the vessel was heated at 150 °C for 5 hours in a stainless-steel autoclave.

(3) Deposition of Fe on dendritic nickel: In the final step, 5 mmol $FeSO_4$ was dissolved in 30 ml ethylene glycol under nitrogen flow and the solution was stirred for 30 minutes. Then the solution was transferred to a PTFE Teflon reaction vessel. The substrate prepared in step 2 was rinsed by DI water and dried. After drying, the substrate was submerged into the ethylene glycol solution that contained $FeSO_4$. The Teflon vessel was then heated at 240 °C for 15 hours. After cooling down, the substrate was rinsed by deionised water multiple times and stored in oven at 60 °C.

Experiment 4: Thermal deposition of NiFe LDH

To prepare NiFe LDH, total amount of 1 mmol of nickel nitrate and iron nitrate was mixed in 18ml deionised water under stirring. The ratio of Ni and Fe was varied. The NiFe LDH thin films were deposited on SS316 via one-step hydrothermal reaction. The solution was prepared by mixing 0.5 mmol $Ni(NO_3)_2 \cdot 6H_2O$, 0.5 mmol $Fe(NO_3)_3 \cdot 9H_2O$, 5 mmol urea and 2 mmol NH_4F. The solution was then transferred to a PTFE Teflon reaction vessel with 1.4 cm x 2 cm SS316 submerged in the solution. The solution was heated at 150 °C for 8 hours. Finally, the substrates were rinsed by large amount of deionised water and stored in a warm environment. The initial attempt of electrode preparation process missed the addition of NH_4F by mistake, however they were still used in the 3-electrode testing. The sample details are shown in the Table 4:

Sample number	Ni (NO3)2 6H2O	Fe (NO3)3 9H2O	Ammonium fluoride added?
1	0.7 mmol	0.3 mmol	Yes
2	0.7 mmol	0.3 mmol	No
3	0.5 mmol	0.5 mmol	Yes
4	0.5 mmol	0.5 mmol	No
5	1 mmol	0	Yes

Table 4. Preparation conditions of LDH prepared in Experiment 4.

3. Results and discussions

3.1 Experiment 1: Electrodeposition of NiFe alloy and hydroxides

3.1.1 The growth of NiFe alloy on the stainless-steel substrate

The deposition solution of this experiment contained Fe^{2+} and Ni^{2+}, which were reduced to metallic form under reduction potential when the pH of the solution was 2. According to the standard reduction potential data, the reduction potentials of Fe^{2+} to Fe and Ni^{2+} to Ni are -0.44 V and -0.25 V vs SHE, respectively, both against SHE [73]. A more negative potential than -0.44V vs SHE had to be used to ensure both reduction of Fe^{2+} and Ni^{2+} occurred. The supporting electrolyte Na_2SO_4 was added to increase the conductivity of the electrolyte, as Na_2SO_4 contained non electroactive species and which had large ionic strength and conductivity than electroactive species added to the solution.

The detailed mechanism of growth was not investigated in this experiment. However, similar experiment performed by Kyung Ho Kim and his/her colleagues studied how NiFe was grown on the nickel foils [74]. They investigated the mechanism by in-situ SEM and EDS pattern of TEM during electrodeposition process. In the paper, they suggested that the initial growth of NiFe film, also called nucleation, occurred during the first 30 seconds of the electrodeposition process. Evenly distributed nuclei then grew to a tree-like structure that consisted of hexagonal crystals that were connected to each other. As the process continued, the side-branched crystals started to grow on edges of hexagonal crystals and its growth rate is faster than the growth of hexagonal crystals themselves. This was because the concentration of Ni^{2+} and Fe^{2+} was higher on the edge of the hexagonal crystals, therefore the new side-branches continued to grow further. Eventually, the characteristics of the film became a multi-branched, dendritic like structure.

According to Saraby-Reintjes and Fleischamann's study on kinetics and reaction mechanism of metallic nickel electrodeposition, it is accepted that the reaction consists of two single-electron charge transfers, where an anion such as SO_4^{2-}, OH^- or Cl^- is involved in the formation of an adsorbed intermediate. The reaction mechanism can be shown as [75]:

$$Ni^{2+} + X^- \rightarrow NiX^+ \quad Equation\ 16$$

$$NiX^+ + e^- \rightarrow NiX_{ads} \quad Equation\ 17$$

$$NiX_{ads} + e^- \rightarrow Ni + X^- \quad Equation\ 18$$

Where X^- represents an anion, that could be SO_4^{-2}, OH^- and Cl^-.

This mechanism could be different depending on the electrode on which the metallic nickel is deposited. For example, Orinakova et al studied pH effect on electrolytic deposition of nickel onto a paraffin impregnated graphite electrode (PIGE) and summarised that the deposition of nickel consisted of 1) a chemical reaction that produces $Ni(OH)_{aq}^{+}$ intermediate, 2) an electrochemical reaction with adsorption of intermediate onto the PIGE and finally 3) further electrochemical reaction where diffusive electroactive species transported to the electrode [76]. Su et al. investigated the nucleation and growth mechanism of electrodeposited NiFe alloys on stainless steel 316 surface, where they concluded that the nucleation and growth of NiFe alloy was different from the growth of individual of nickel and iron metals [77]. They obtained an amperommogram of which the main characteristics

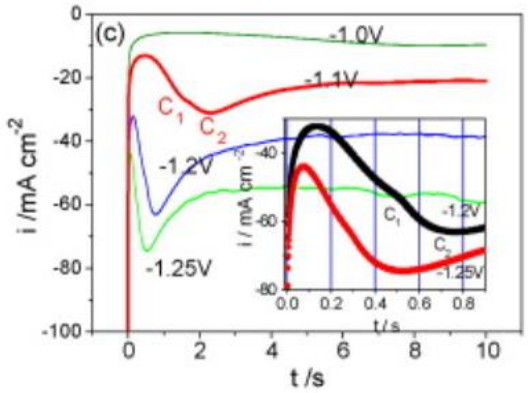

Figure 18. The amperommogram obtained by Su et al. that indicates current transient of NiFe codeposition at different potentials. From the inset plot, 2 current changed can be observed (C1 and C2), that represented two nucleation and growth processes occurring during NiFe deposition. Such current trend was not observed in individual nucleation and growth process of Ni and Fe, according to Su et al [77].

were 1) a reducing current at beginning of the deposition process, which was due to the charging of electrical double layer [78] and intermediate adsorption; 2) then rising current that was due to nucleation and growth of NiFe alloys; 3) and a stable period in which the current remained constant for some time, at this point the current reached maximum; 4) and finally a reduced current due to the growth of diffusive layer of metal ions, at which point a limit diffusion current was reached [77]. This could be caused by hydrogen evolution reaction. The graphic explanation of their studies is shown in Figure 18.

They also found that during the electrodeposition of NiFe, there was a second nucleation and growth occurring, as shown in the inset in Figure 18 at -1.2V. Therefore, they constructed a theoretical non-dimensional relationship between current and time, considering the interaction of both Ni and Fe nucleation and growth processes, which are given by [77]:

$$\left(\frac{i}{i_{max}}\right)^2 = \frac{1.9542}{t/t_{max}}\left\{1 - \exp\left[-1.2564\left(\frac{t}{t_{max}}\right)\right]\right\}^2 \qquad Equation\ 19$$

$$(\frac{i}{i_{max}})^2 = \frac{1.2254}{t/t_{max}}\left\{1 - \exp\left[-2.3367\left(\frac{t}{t_{max}}\right)^2\right]\right\}^2 \qquad Equation\ 20$$

for instantaneous and progressive nucleation, respectively.

3.1.2 The pH effect on the deposition of the films

As stated in experimental section, electrodes 1-4 were prepared in very acidic aqueous solution, whereas electrode 5 was prepared in slightly acidic solution where sulphuric acid was not added. As seen in Figure 19, pH played an important role in the kinetics of nickel electrocrystallisation.

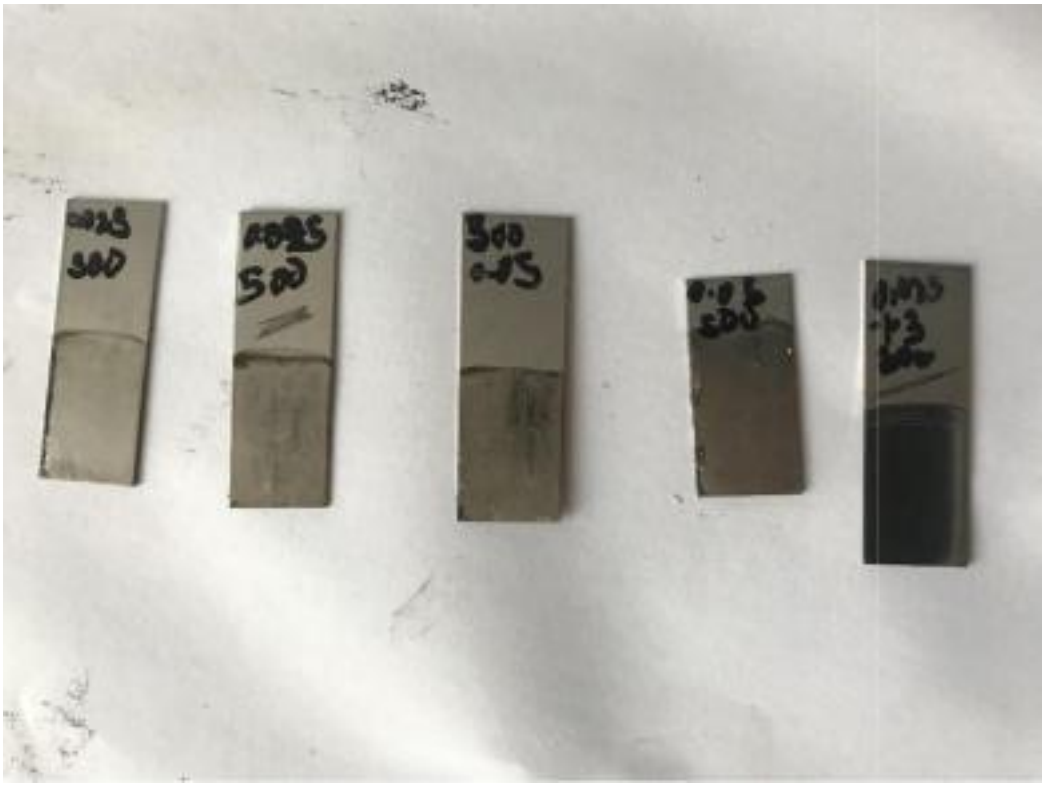

Figure 19. Samples from left to right are Electrode 1, 2, 3, 4 and 5. The pH of electrolyte during deposition was 2 for Electrode 1-4, and that was 4.2 for Electrode 5.

During the deposition process, hydrogen evolution reaction (HER) occurs at working electrode. As the electrolyte was acidic, following reaction occurs:

$$2H^+ + 2e^- \rightarrow H_2 \qquad Equation\ 21$$

In meantime, Ni^{2+} also undergoes charge transfer process, where Ni^{2+} near the electrode surface is transformed to adsorbed Ni_{ads}^{+}, which is an intermediate as well as a catalyst for the formation of adsorbed hydrogen, H*ads. This is supported by Chassaing's work of impedance measurement on the kinetics of nickel electrocrystallisation, which suggested that when the deposition sulphate solution pH is 2-4, the reaction that is associated with nickel electrocrystallisation is [79]:

$$Ni^{2+} + 2e^- \rightarrow Ni \qquad Equation\ 22$$

In Madhusmita's study, it was suggested that the mechanism of nickel deposition also contained other reactions in addition to the those shown in Equation 22. According to their conclusion,

nickel monohydroxide plays a key role in the overall charge transfer process that led to nickel deposition. The reactions suggested by Madhusmita are [80]:

$$Ni_2^+ + H_2O \leftrightarrow NiOH^+_{(aq)} + H^+ \qquad Equation\ 23$$

$$NiOH^+_{(aq)} \leftrightarrow NiOH^+_{(ads)} \qquad Equation\ 24$$

$$NiOH^+_{(ads)} + e^- \rightarrow NiOH \qquad Equation\ 25$$

$$NiOH + H^+ + e^- \rightarrow Ni + H_2O \qquad Equation\ 26$$

When nickel sulphate is dissolved in water, nickel monohydroxide is produced (Equation 23). This species is then adsorbed onto the electrode surface (Equation 24), where the charge transfer process would convert adsorbed $NiOH^+$ to NiOH (Equation 25). The further charge transfer in acidic solution would bring to the products which are nickel metal and water (Equation 26). The preparation of Electrode 1 – 4 in this experiment all followed above reactions.

The appearance of Electrode 5 is very different from those of Electrode 1 – 4, of which the difference can be attributed to the pH change. When the deposition solution is less acidic and with presence of hydrogen, the dominated reaction is:

$$2H_2O + O_2 + 4e^- \rightarrow 4OH^- \qquad Equation\ 27$$

The pH near the electrode increases due to the presence of OH^-, which reacts with adsorbed nickel, producing nickel hydroxide by following reaction:

$$Ni^{2+} + 2OH^- \rightarrow Ni(OH)_2 \qquad Equation\ 28$$

This is supported by Lantelme's work in establishing model of nickel electrodeposition from acidic medium, where Lantelme compared the current density at different solution pH by using potentiostatic deposition technique and concluded that in unbuffered sulphate solution (pH 4.5), oxygen reduction reaction takes place before nickel deposition, for which a layer of nickel hydroxide is formed before any nickel deposition could occur [81]. In Holm and O'Keefe's study of evaluation of nickel deposition on stainless steel cathode by EIS study also proved that at low pH (2.5), the impedance spectra showed two semi-circles, the quality of deposition prepared under this condition was good according to their morphology study. Under conditions which all other parameters were controlled, when the pH of sulphate solution increased to 3.5, the spectra consisted of a incomplete semi-circle and a huge impedance growth at low frequency region,

which indicated the formation of a passivating layer that was believed to be nickel hydroxide [82]. The impedance spectra obtained by Holm and O'Keefe is shown below [82].

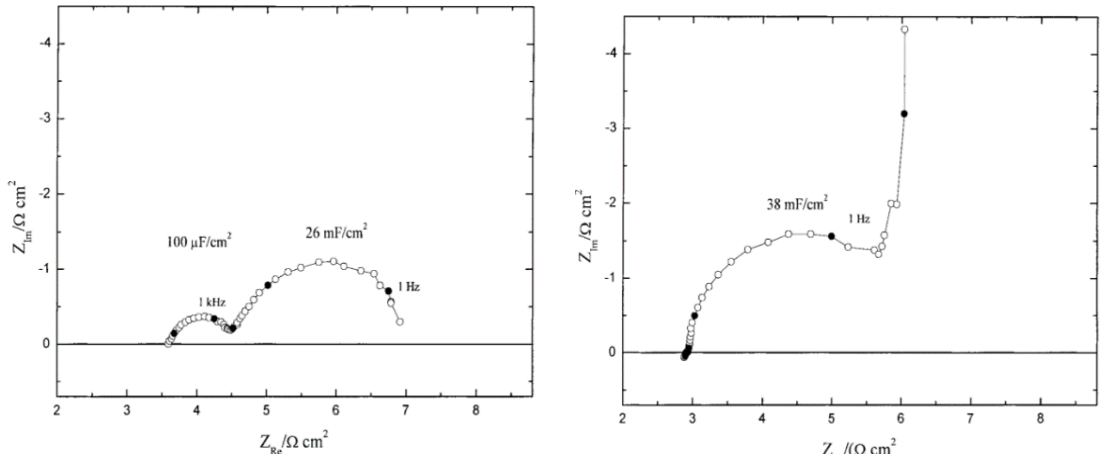

Figure 20. The impedance spectra for nickel sulphate electrolyte at pH 2.5 (left) and 3.5 (right) at 40 °C, no stirring, platinum anode, stainless steel 316 substrate. The spectra were obtained by Holm and O'Keefe [82].

3.1.3 Material morphologies

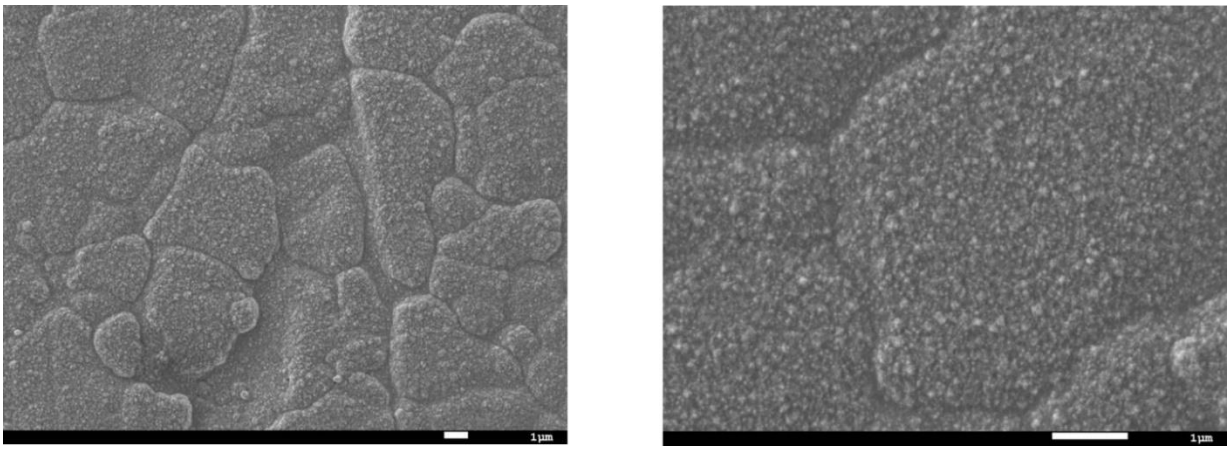

Figure 21. SEM images of electrode 5. Left: x5000 magnification. Right: x16000 magnification.

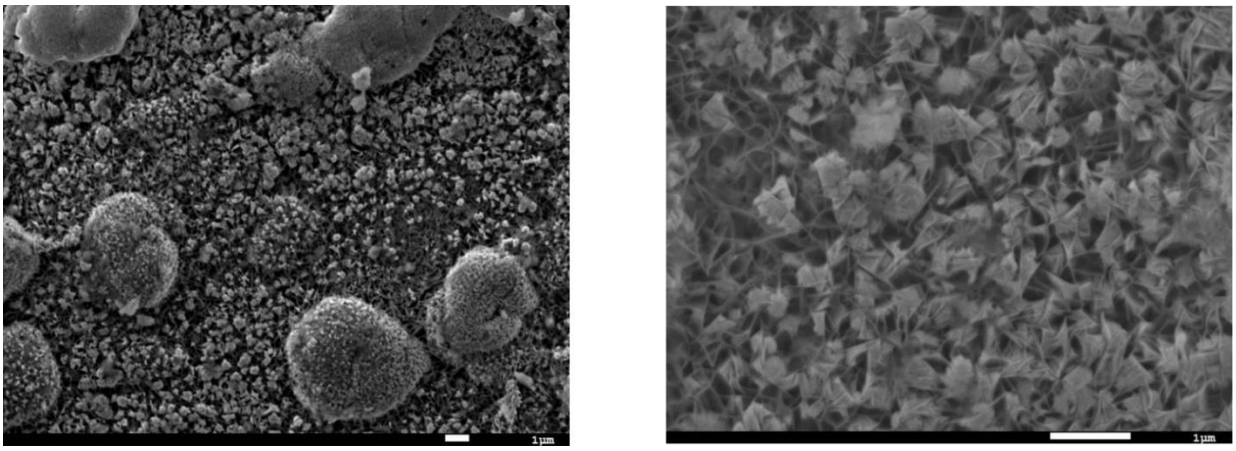

Figure 22. SEM images of electrode 2. Left: x5000 magnification. Right: x16000 magnification.

The SEM images shown in Figure 21-22 confirmed that the pH will affect the morphologies of the NiFe deposits. When the pH of deposition solution was 2, the SEM image shown a grain-like structure of the deposit, which was grown under sufficiently fast mass transport and growth rate of Ni and Fe crystals. When the pH of deposition electrolyte was 4.2 (no H_2SO_4 was added), the SEM image shown a flower like morphology (Figure 21). The morphologies of electrodes 1-4 did not have distinguishable difference.

As suggested by Equations 27-28, the secret of pH effect on morphologies of electrodeposited NiFe is the local concentration of hydroxide ions present near the electrode in the deposition electrolyte. When sulphuric acid was added to the solution, it became very acidic due to increasing of hydrogen ion concentration. Under high reduction potential, Ni^{2+} and Fe^{2+} ions in the bulk solution were reduced to their metallic form on the substrate. When sulphuric acid was not added, the concentration of hydroxide ions increased due to the reduction of water ($2H_2O + 2e^- \rightarrow H_2 + 2OH^-$). The negative hydroxide ions near the substrate would combine with positive Ni^{2+} and Fe^{2+}, producing NiFe hydroxide. To confirm the presence of, the elemental analysis was performed by EDS, of which the results are shown in section 3.1.4.

3.1.4 OER reaction in NiFe deposited anode

To understand the OER reaction mechanism, cyclic voltammetry was conducted for the as prepared samples (Electrode 2 and Electrode 5) in 0.1M KOH at room temperature within potential range from -0.2 V to 0.6 V, the scan rate was 20 mV/s (as Figure 23 shown). Electrode 2 was used because it was assumed that it was representative enough for Electrodes 1-4, which was prepared under same pH condition. In Figure 23, O1 and O2 denote first and second oxidation peaks, respectively, and R1 represents first reduction peak for Electrode 5 (red plot). The first oxidation peak O1 occurred at potential of 0.4 V, at which OH^- adsorption was triggered on electrode surface, followed by the formation of other oxygen containing intermediates which contain active sites such as $Ni(OH)_2$, NiO and NiOOH. In general, Ni^{2+}/Fe^{2+} hydroxides or oxides was converted to Ni^{3+}/Fe^{3+} oxyhydroxide. This reaction is represented in Equation 29:

$$Ni/Fe(OH)_4 + 2OH^- \leftrightarrow Ni/Fe\big(O(OH)\big)_2 + 2H_2O + 2e^- \quad Equation\ 29$$

The second oxidation peak O2 represented OER, of which the gradient was much steeper. When the potential was scanning to more negative direction, the reduction peak, R1 occurs at 0.5 V. At this step, the reaction occurred was reverse reaction shown in Equation 29. However, it may also be the reduction of oxygen that has not escaped the electrode surface. The R1 peak was very evident for Electrode 5, however it was relatively small for Electrode 2. This can be explained by that the phase transformation of NiFe alloy did not occur. This small peak was owing to the reduction of oxygen remaining on the electrode.

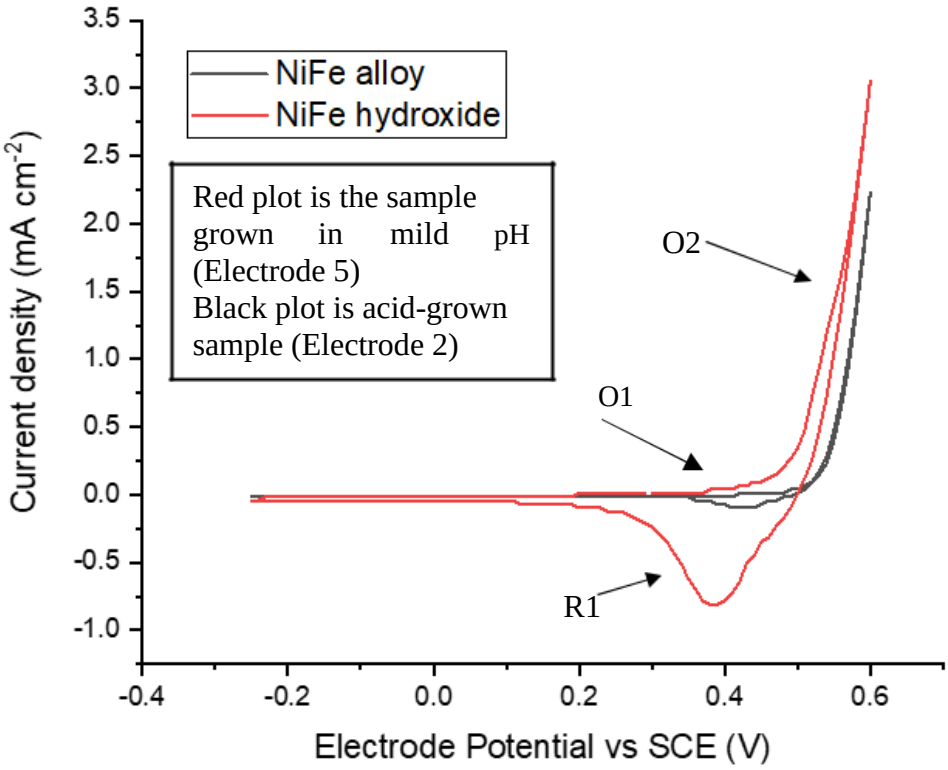

Figure 23. Cyclic Voltammetry of NiFe alloy (Electrode 2) and NiFe hydroxide (Electrode 5).The CV was scanned in room temperature between -0.2V to 0.6V with scan rate of 20 mV/s. The electrolyte of KOH was 0.1M KOH.

The reason of higher OER activity of Electrode 5 than Electrode 2 is still not understood in detail due to ambiguous understanding in the structure of the nickel compounds variants [83]. According to the Bode's Diagram mentioned in literature review section, pristine $Ni(OH)_2$ deposit produced after electrodeposition process was α-$Ni(OH)_2$. The α-$Ni(OH)_2$ will be transformed into β-$Ni(OH)_2$ after aging, of which the duration is unknown.

In this experiment, to what form the $Ni(OH)_2$ was transformed was not investigated. However it was assumed that prior to the electrochemical characterisation of the material, the $Ni(OH)_2$ was partially aged to β phase as the electrode was exposed to the air for approximately a week awaiting SEM characterisation. During OER in KOH electrolyte, the aged β-$Ni(OH)_2$ was oxidised to β-NiOOH, which is believed to be the active species for OER by many researchers such as Lyons and Brandon [84][85]. However, there has been argument on this, for example Bediako et al suggested that γ-NiOOH might be more efficient than β-NiOOH [86]. Under high anodic potential, β-NiOOH is transformed to γ-NiOOH according to Bode Diagram.

It was also believed that although the electrode was aged for some time, there was still some proportion of the $Ni(OH)_2$ was converted to γ-NiOOH via α-γ route, which was also the

hypothesis suggested by Lyons [85]. The current experimental data was not sufficient to support such hypothesis, the experiment can be improved to obtain deeper understanding in $Ni(OH)_2$ phase transformation , this improvement is mentioned in conclusion section.

3.1.5 Elemental analysis by EDS

The elemental composition of electrodes was examined by energy-dispersive X-ray spectroscopy (EDS).

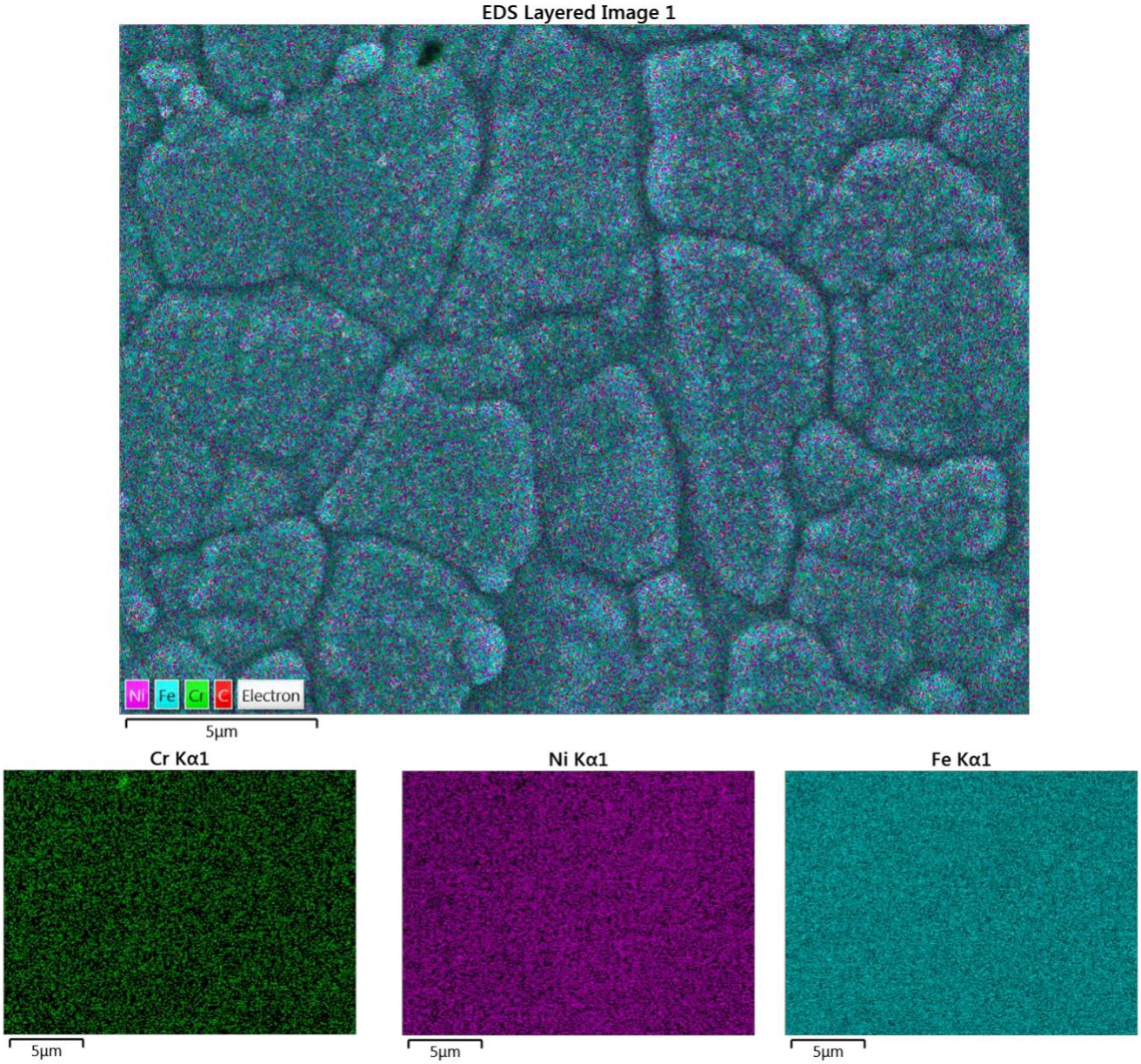

Figure 24. EDS map images of Electrode 2.

As shown in Figure 24, electroplated Ni and Fe evenly cover the substrate, the blue colour that represents detected Fe is very dense, meaning that the particular region is covered by Fe. The pink colour that represents Ni is also distributed over the substrate. The green colour that represents chromium is not as dense as Ni and Fe, indicating that the region contains much less chromium than Ni and Fe.

The above statement is confirmed by the EDS map spectrum indicates that the region shown in Figure 24 contains 63.1% Fe, 30% Ni and only 2.1% Cr. All of these values except Fe are different from those detected in bare electrode, where the percentages of Fe, Ni and Cr are 66.3%, 9.6% and 15.9%, respectively.

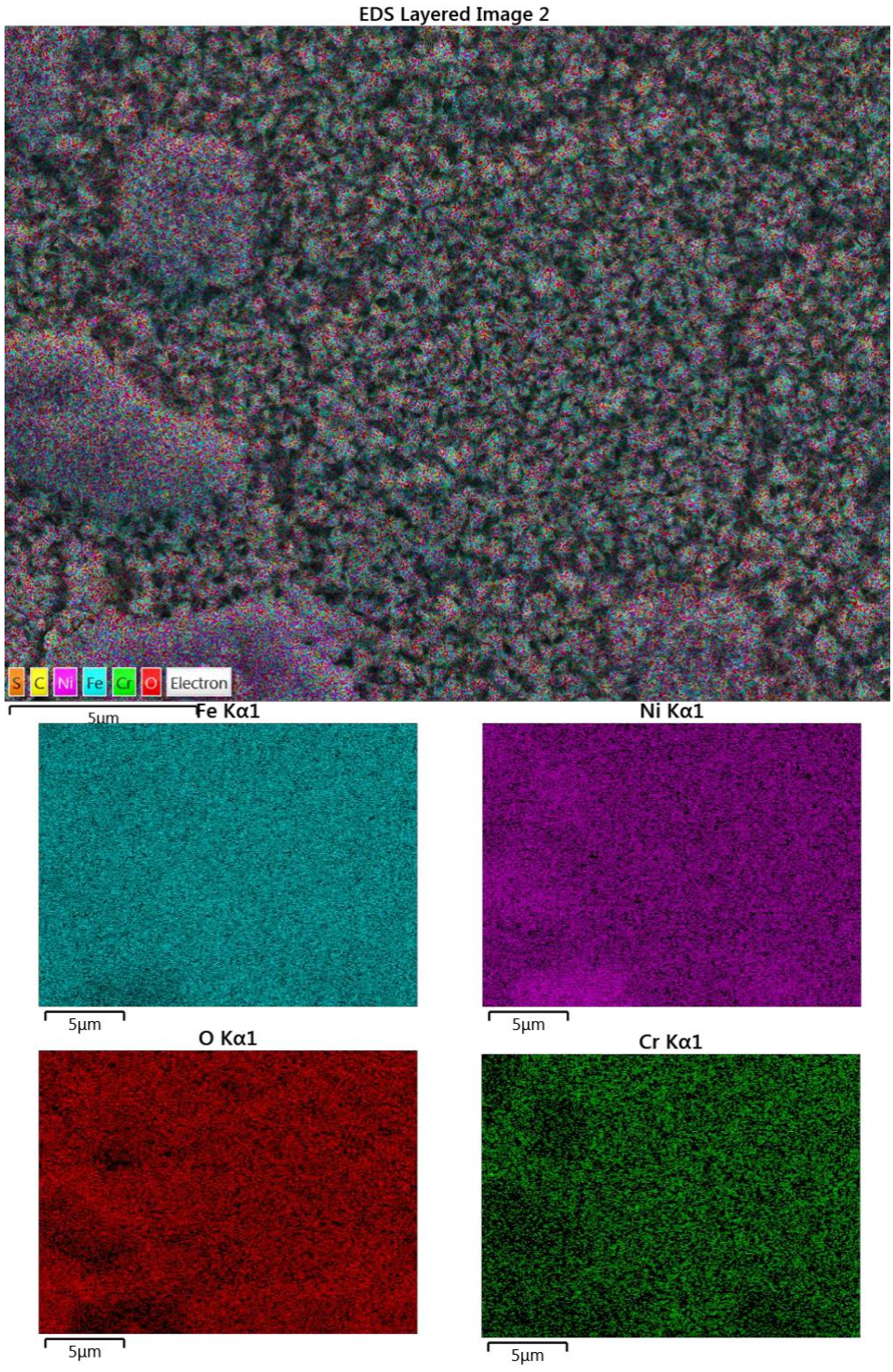

Figure 25. EDS map images of Electrode 5.

For electrode 5, the main difference from electrode 2 is the presence of oxygen. As the Figure 25 shows the region is covered by a lot of red area, representing the presence of significant amount of oxygen atom. According to the map sum spectrum, the percentage of oxygen in area shown in Figure 25 is 9.0%, which is another evidence of the formation of NiFe hydroxide on the substrate (hydrogen atom cannot be detected by EDS).

The summary of EDS spectrum of Electrode 2 and Electrode 5 is shown in the Table 5.

	Bare electrode	Electrode 2	Electrode 5
Fe	66.3%	63.1%	47.7%
Ni	9.6%	30%	35.1%
Cr	15.9%	2.1%	3.2%
C	5.2%	4.7%	4.7%
O	0	0	9.0%

Table 5. Elemental composition of each element in bare electrode, Electrode 2 and Electrode 5, given by EDS spectrum.

The ratio of Fe to Ni listed in Table 5 is not reflected to the Ni^{2+} and Fe^{2+} composition in deposition electrolyte, this is because the electrodeposition process in this experiment was believed to be anomalous codeposition, during which the reduction rate of more active species was faster than that of noble species [87]. In this case, the rate of $Fe^{2+} \rightarrow Fe$ was faster than $Ni^{2+} \rightarrow Ni$. Moreover, the coverage of Fe would hinder the growth of Ni on top of it. For this reason, the composition of less noble metal (Fe^{2+}) was larger than that of more noble metal (Ni^{2+}) [88].

3.1.6 Electrochemical characterisation of OER

The activity of OER was assessed by cyclic voltammetry (CV) and linear sweep voltammetry (LSV) techniques using 3-electrode system, where prepared NiFe electrode, SCE and Pt wire were used as working, reference and counter electrodes, respectively. The CV and LSV were performed in 0.1M KOH at room temperature. The scan range was between 0-1.2V vs SCE with scan rate of 50 mV/s.

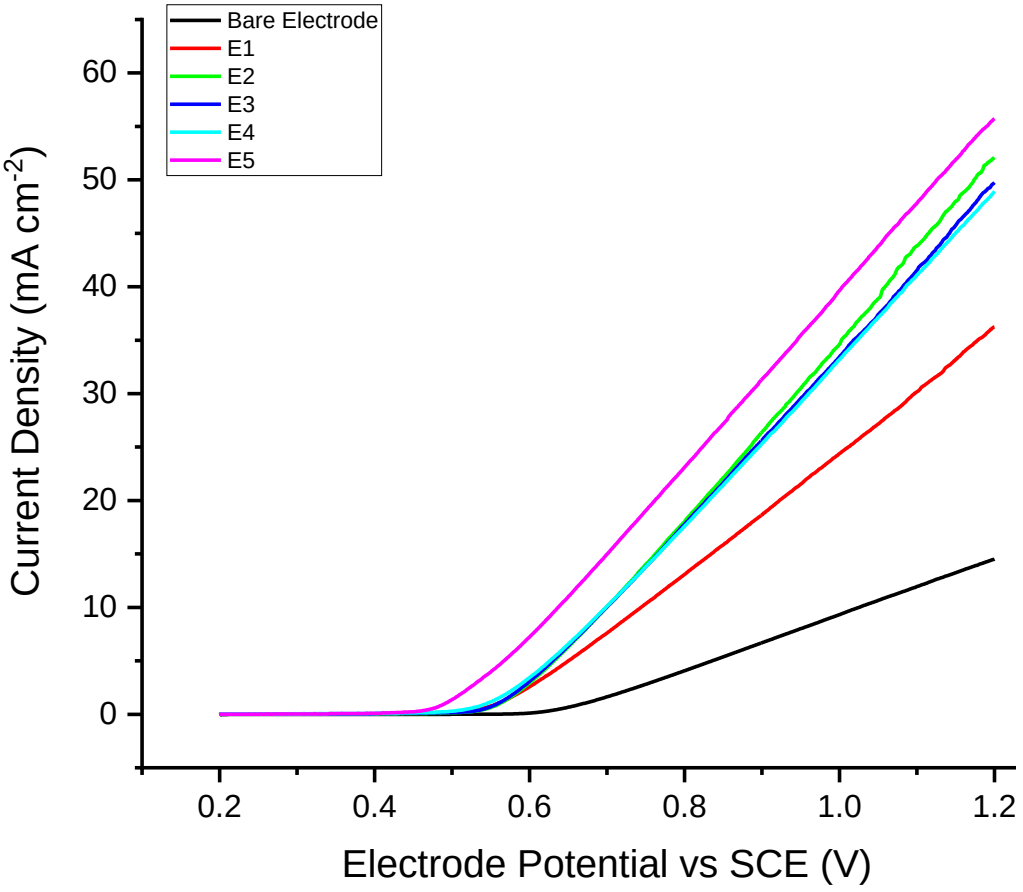

Figure 26. Linear Sweep Voltammogram of NiFe deposited electrodes prepared in Experiment 1. The bare electrode was used as reference to compare how much OER was improved by individual electrode that was coated with NiFe. The LSV plots were recorded between 0.2 – 1.2 V vs SCE at room temperature, 0.1M KOH, 20 mV/s scan rate.

The LSV plot shows that all electrodeposited NiFe samples prepared in this experiment exhibited enhanced OER compared to the stainless steel without any coating (black line in Figure 26). At any point of the Figure 26, E5 was the best performing sample, for instance, at 1.2V vs SCE, the peak current density of Electrode 5 is 55 mA cm^{-2}. E2, E3 and E4 slightly underperformed with current density between 50—48 mA cm^{-2}. E1 exhibits significant low current density of 35 mA cm^{-2}. The bare electrode only produced small current density of approximately 15 mA cm^{-2}.

All potentials were recorded against SCE, of which the potential is 0.248 V vs SHE at 20 °C. Therefore, 0.248 V should be added to the potential read in Figure 26. For example, at 10 mA cm^{-2}, the potential of E5 is 0.67 V vs SCE and 0.918 V vs SHE. The thermodynamically potential of OER half reaction is 0.4 V vs SHE in alkaline electrolyte, therefore the overpotential of E5 at 10 mA cm-2 is 0.518 V (518 mV). It is worth noting that although E5 displayed the lowest overpotential at 10 mA cm^{-2}, the onset potential of E5 (0.55 V) was a bit higher than that of E4 (0.5 V). The overpotential of other samples at 10 mA cm^{-2} are shown in the Table 6.

Materials	Current Density at 1.2 V vs SCE (mA cm-2)	Onset OER potential vs SCE (mV)	Overpotential vs SCE at 10 mA cm-2 (mV)
E1	35	450	578
E2	52	580	628
E3	49	580	628
E4	48	550	628
E5	56	480	518
Bare stainless-steel	15	600	848

Table 6. Electrochemical performance of all samples in experiment 1.

The Tafel plot of OER is shown in the Figure 27, where only anodic half of the Tafel plots are presented. Tafel equation is a very important electrochemical kinetics characterisation tool which indicates how current responds to the change of applied electrochemical potential [89]. The linear section enclosed by the red box is used to find out the Tafel slope, which is shown in the Figure 27. The Tafel equation is derived from Butler Volmer equation, which is shown by Equation 13. The Butler Volmer equation can be simplified as Tafel equation when the overpotential is large enough (Wei, Fang and Liu, 2012), e.g. above 15 mV. The Equation 13 would become:

$$\eta = \left(\frac{2.303RT}{\alpha F}\right)\log\left({}^{i}/_{i_0}\right) \qquad Equation\ 30$$

Where the term b is the constant variable that related to the charge transfer coefficient α. Therefore, the Tafel equation can be used to evaluate the reaction kinetic of electron transfer reaction. The charge transfer coefficient α is related to the number of electron transfer of electrochemical reactions, which usually involve multiple electron transfer. The charge transfer coefficient is mainly attributed to the electron transfer of rate determining steps of a series of electrochemical reaction, however the non-rate determining steps also contribute to the charge transfer coefficient. For instance, if only one electron is involved in rate determining step when the charge transfer coefficient is 0.5, then the Tafel gradient of the overall reaction is RT/(n+0.5)F, where n represents the number of electron transfer in non-rate determining step. By calculation, when n is 0 and 1, the Tafel gradient values are roughly 120 mV dec^{-1} and 40mV dec^{-1} (millivolt per decades of current), respectively, at 298K.

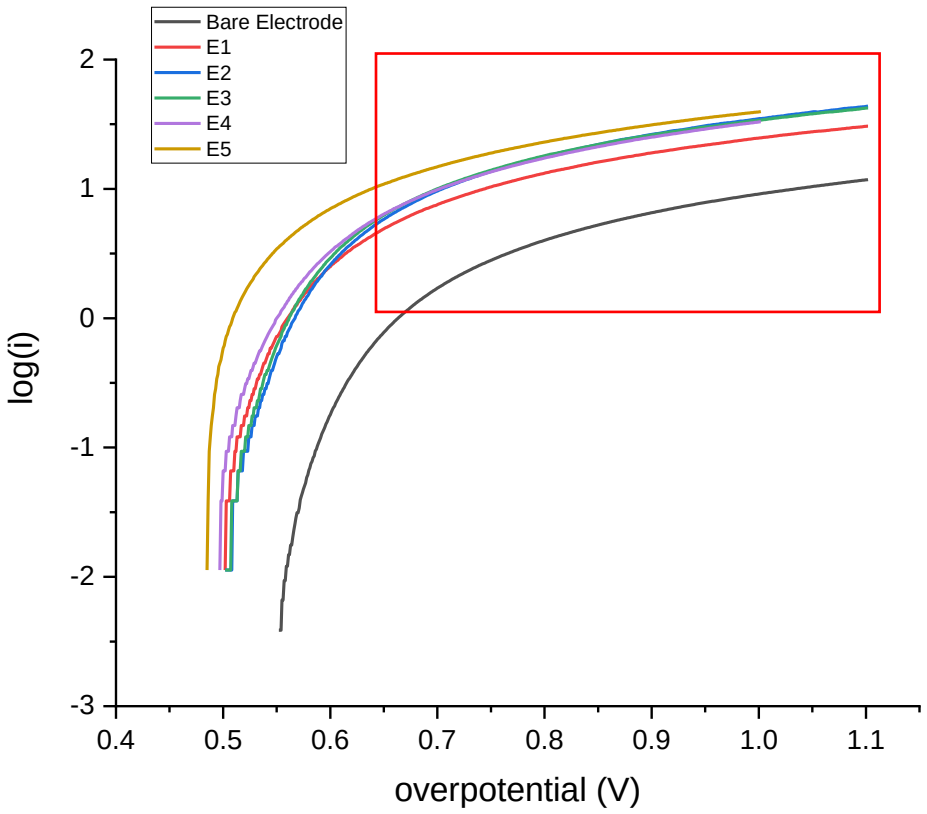

Figure 27. Anodic Tafel plots of all NiFe deposited electrodes

To calculate the exchange current density (i_0), the straight line is extrapolated and its y – intercept with OER onset potential is the value of log(i_0). The value of i_0 can be obtained by taking e^log(i_0), this number is usually very small. At this current density, the current flows to both anodic and cathodic directions and the overpotential is 0, i.e. no net current flowing. The full Tafel plot of E5 is shown in the Figure 28, the equation of linear section of E5 is y = 1.3x + 0.26, the equation of the straight line was obtained simply by dividing the difference of y coordinates by the difference of x coordinates of 2 data points, because it was challenging to obtain a straight line that best fit the linear section of the Tafel plot. Therefore, the log of exchange current density can be calculated by substituting appropriate value of "x", which was 0.48, therefore log(i_0) = 0.884. The exchange current density of E5 is therefore the exponent of 0.884, obtaining a value of 2.42 x 10-3 A cm^{-2}.

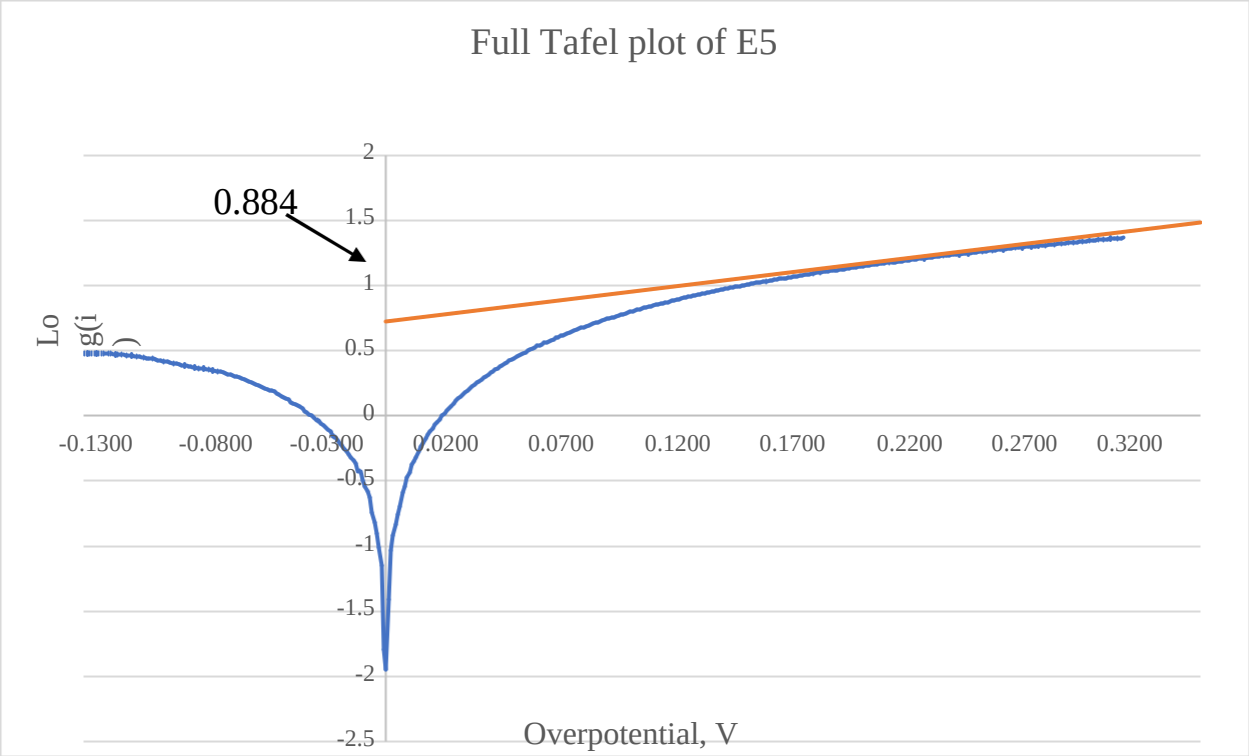

Figure 28. Full Tafel plot of E5.

Many literatures present the Tafel plot in the format of overpotential verses log(i). To compare with the Tafel gradient obtained by other researchers, the Tafel gradient should be converted to the format that is aligned to the form that other researchers use, in which case the reciprocal of the gradient value (1.3) will be taken. Therefore the Tafel gradient of Electrode 5 is 769.2 mV dec-1. This value is much higher than currently state of art OER catalyst such as RuO_2, which is approximately 60 – 120 mV dec^{-1}, obtained by Devadas et al [90]. Damjanov et al. proposed 14 possible OER reaction routes, which the observed Tafel gradients are ~120 mV dec-1 for Pt and RuO_2 in acid solution and ~60 mV dec^{-1} for platinum in alkaline solution [91]. The much higher Tafel gradient for Electrode 5 may in some degree suggest that it is not as good OER electrocatalyst as platinum and RuO_2. However, it is also difficult to draw meaningful information by graphically analyse Tafel plot of OER due to its limitations such as the formation of gas bubbles on the electrode. The nucleation of air bubbles is controlled by current density and mass transfer [92]. Therefore the high Tafel gradient of Electrode 5 can be partially resulted by the blockage of channel through which air bubbles could escape. The unremoved air bubbles can reduce the surface area of active sites of electrocatalyst and increase the ohmic resistance, for which polarisation curve as well as Tafel plot are distorted [92]. To investigate Tafel plot more

meaningfully, it is essential to correct the polarisation curves by considering the ohmic drop, in which case the Equation 30 becomes:

$$\eta = \left(\frac{2.303RT}{\alpha F}\right)\log\left({}^{i}/_{i_0}\right) + iR \qquad Equation\ 31$$

Where R is the total area-specific uncompensated resistance of the electrochemical system [92]. To obtain the value of R, the Equation 31 can be differentiated with respect to current density, giving:

$$\frac{d\eta}{di} = \left(\frac{2.303RT}{\alpha F}\right)\Big/_{i} + R \qquad Equation\ 32$$

The value of R in Equation 32 helps the correction of experimental overpotential by subtracting ohmic drop from overall overpotential, which can be calculated by : $\eta_{correction} = \eta - iR$.

3.1.7 Stability of the best performing sample (Electrode 5)

As bare stainless-steel electrode, nickel iron compound deposited electrode would also undergo degradation during its operation in alkaline environment, for which the resistance to degradation is also a key parameter to ensure a good overall performance of the electrolyser. In this section, the results of stability test were presented in the form of current density vs time plot. The chronoamperometry was used to investigate the stability, where the potential was held constant at 1.2V vs SCE for 15 hours each day. 4 consecutive days of stability test lasted for a total of 60 hours. The sample was rinsed by deionised water to eliminate the effect of bubble blinding which would cause reduced performance over long time. A carbon rod was used as counter electrode in this experiment. The concentration of the electrolyte used in the stability test was slightly higher, which was 0.178 M KOH (10g of KOH in 1L water). This concentration matched the one used by Clean Power Hydrogen Ltd, however the temperature was kept at room temperature.

The trend of plots in Figure 29 is the same for all days, the current density increased with time during the first 5000 seconds. Then it started to drop until the end of the test. Although the current density reduced with time, it could be seen that the current density remained high at the beginning of the next day. The initial current density was even higher than that of previous day. This could be the indication of more $Ni(OH)_2$ underneath the interface was transformed to β- or γ-NiOOH. As mentioned above, it was not evident if it was the β- or γ-NiOOH, as the Electrode 5 was not cycled in KOH immediately after it was prepared but stored for some days awaiting SEM, therefore it was unable to identify if $Ni(OH)_2$ was aged to β-NiOOH during this period. If β-NiOOH

was not formed, then the CV cycling in KOH would transform original α-$Ni(OH)_2$ directly to γ-NiOOH, according to Bode diagram. Furthermore, the trend of current density change for all 4 days was also a sign of the reduced current density was not caused by the degradation of catalytic material. The assumption is that the decline of current density could be due to the bubble blinding during the day as well as the resistance of diffusion layer.

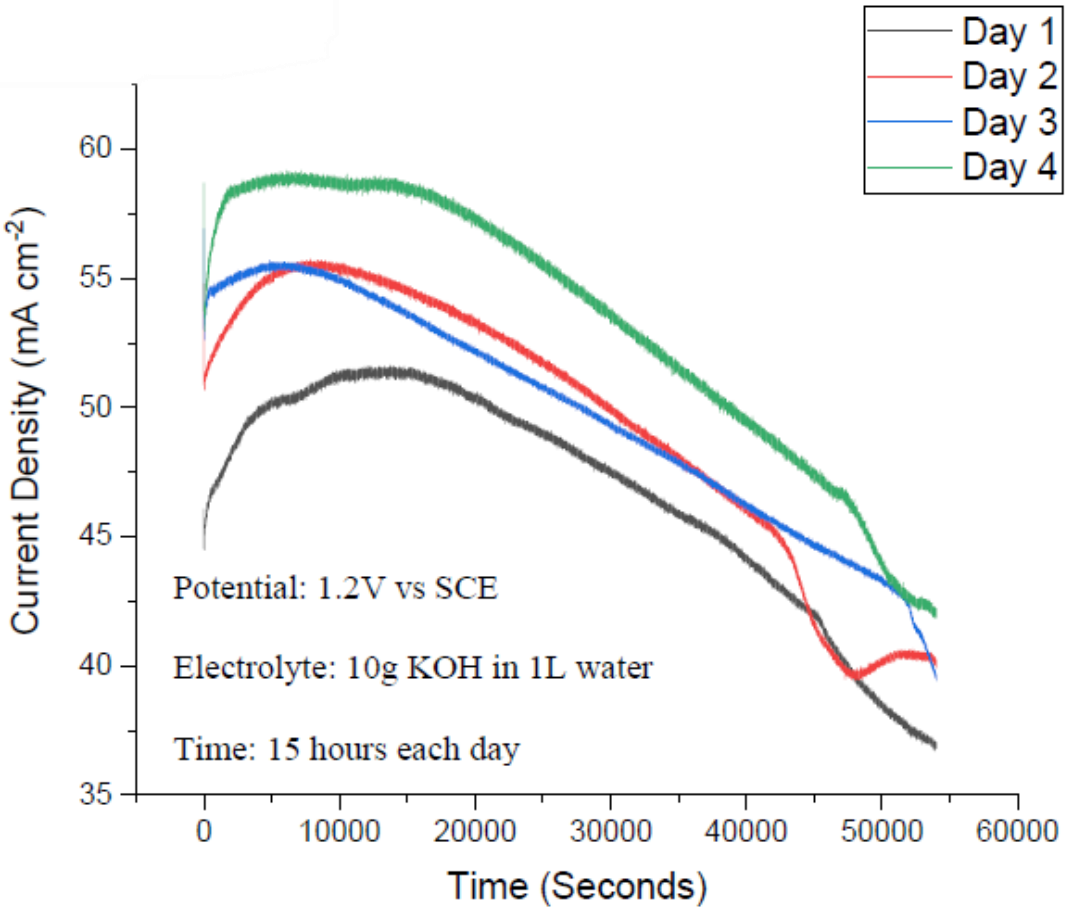

Figure 29. The stability test results of E5 carried out by using chronoamperometry. The electrolyte concentration was 10g KOH in 1L water. 1.2V vs SCE was held during each day, which lasted for 15 hours. At the end of each day, the electrode was rinsed by DI water and fresh electrolyte was used for next day.

3.1.8 Conclusion

In this experiment, NiFe thin films were successfully deposited by electrodeposition in a mixed solution containing Ni^{2+} and Fe^{2+}. It is proven that the deposition condition will alter the morphologies of the thin films and affect their electrochemical performance. At low pH, the rate of Ni^{2+} and Fe^{2+} reduction dominated the process which metallic nickel and iron were produced. When pH increased, the formation of NiFe hydroxide became dominant. The electrodes with NiFe thin film deposited in this experiment all exhibited outstanding OER performance, especially for NiFe hydroxide sample (Electrode 5). Yet it is still vague if the enhanced OER activity was caused by β- or γ-NiOOH, however it can be certain that the rate determining step is the formation of OOH, which can be targeted in future design of NiFe based catalyst in order to reduce the reaction kinetic. If the experiment can be repeated in future, individual nickel and iron coated electrodes also need testing as control variables. In order to investigate how phase transformation takes place, e.g. how long of aging can achieve β-$Ni(OH)_2$ from pristine α-$Ni(OH)_2$ and how much current would cause α-$Ni(OH)_2$ to be transformed to γ-NiOOH, more cycles of CV (1000 cycles for example) need applying to the working electrodes. Then the current density at a specific potential or the overpotential at 10 mA cm^{-2} can be compared to evaluate if aged or cycled electrodes outperform the pristine electrodes. This could potentially provide understanding in how different phases of $Ni(OH)_2$ and NiOOH would enhance the OER and how electrode materials degrade with number of operation cycles in alkaline electrolyte. Furthermore, EIS will be useful technique to gain deeper understanding in overall reaction kinetics of OER with the presence of NiFe based catalyst.

The SEM image of Electrode 5 shows that the Electrode 5 had more porous-like structure, which provides sufficient pathway for gas removal and mass transport of reactant species. To obtain evidence of the surface area plays a role in enhanced OER, further experiment can consider measuring the surface area of the Electrode 5 by BET analysis.

The stability test suggested that the reduced current density during each day was caused by air bubbles remained on electrode rather than electrode degradation, the evidence was that the current density generated at the beginning of next day still remained high, after thorough washing to remove the air bubbles and diffusive layer. Therefore, it can be concluded that the stability of Electrode 5 was good for four days, yet it is not sufficient to evaluate its longer-term stability due to the project timescale. To improve this, a longer-term stability test should be performed in both half cell and full cell electrolysers. The Electrode 1-4 should also be tested under same procedure to compare the stability of all Electrodes 1-5.

Although the NiFe hydroxide film developed in this experiment shown excellent OER activity, there are still some improvement areas. Many literatures suggested that when the Ni and Fe are present in a specific ratio of 1:2, it forms $NiFe_2O_4$, which is called nickel ferrite which has a spinel structure. Due to its resistance to corrosion and high OER activity, nickel ferrite would be an excellent choice in a commercial ready electrolyser device because its low cost.

3.2 Experiment 2: Electrodeposition of hierarchical NiFe hydroxides

3.2.1 Formation of NiFe hydroxide films

Although the materials of the films produced in this experiment were the same as the materials in Experiment 1, the condition of the electrodeposition and raw materials used were different, for which the chemical and electrochemical properties were also altered. The main differences were:

- The precursors in this experiment were nickel nitrate and iron nitrate, whereas in Experiment 1, the precursors were nickel sulphate and iron sulphate.
- The oxidation state of Fe in iron sulphate used in Experiment 1 was 2+, however the Fe in iron nitrate used in this experiment had the oxidation state of 3+. This would result in difference in cyclic voltammetry plot due to the redox reaction between Fe (III) and Fe (II).
- The deposition potentials used were -1.0V and -1.3V vs SCE. Initially, only -1.3V vs SCE was used however it generated very poorly adherent coatings. Then the pH was adjusted by 0.1V towards to less negative potential. It was found that when the potential was -1.0V vs SCE, observable improvement was observed.
- The pH of the deposition solution in this experiment was not measured, it was also not artificially changed.

Under the conditions described in experimental procedures section, the mechanism of NiFe hydroxide growth were different from the one in Experiment 1. With the presence of NO^{3-} ions, they were reduced to produce OH^- near the electrode by following reaction [93]:

$$NO_3^- + 7H_2O + 8e^- \rightarrow NH_4^+ + 10OH^-$$

As the result, the local generated OH^- would combine with Ni^{2+} and Fe^{3+} present in aqueous solution, producing $Ni(OH)_2$ and $Fe(OH)_3$ thin film on the surface of the substrate. This resulted in the formation of a brown coating on stainless steel, as shown in the Figure 30. The reaction occurred during the formation of the film is shown in the Equation 33 [93]:

$$3Ni^{2+} + 2Fe^{3+} + 6OH^- \rightarrow Ni_3Fe_2(OH)_6 \qquad Equation\ 33$$

Nickel hydroxide produced by electrodeposition of nitrate solution is described as electrochromic [94], which showed optical colour change when the potential was applied. As figure 30 shows, the initial colour of pristine electrodes was pale brown/yellow, which indicated possible mixture of nickel hydroxide (green) and iron hydroxide (brown). Due to the electrochromic effect, the electrodes turned black during oxidation and the colour did not change back to its original colour during reduction. Unfortunately, the electrochromic effect was not investigated in depth as it was out of scope of the objectives.

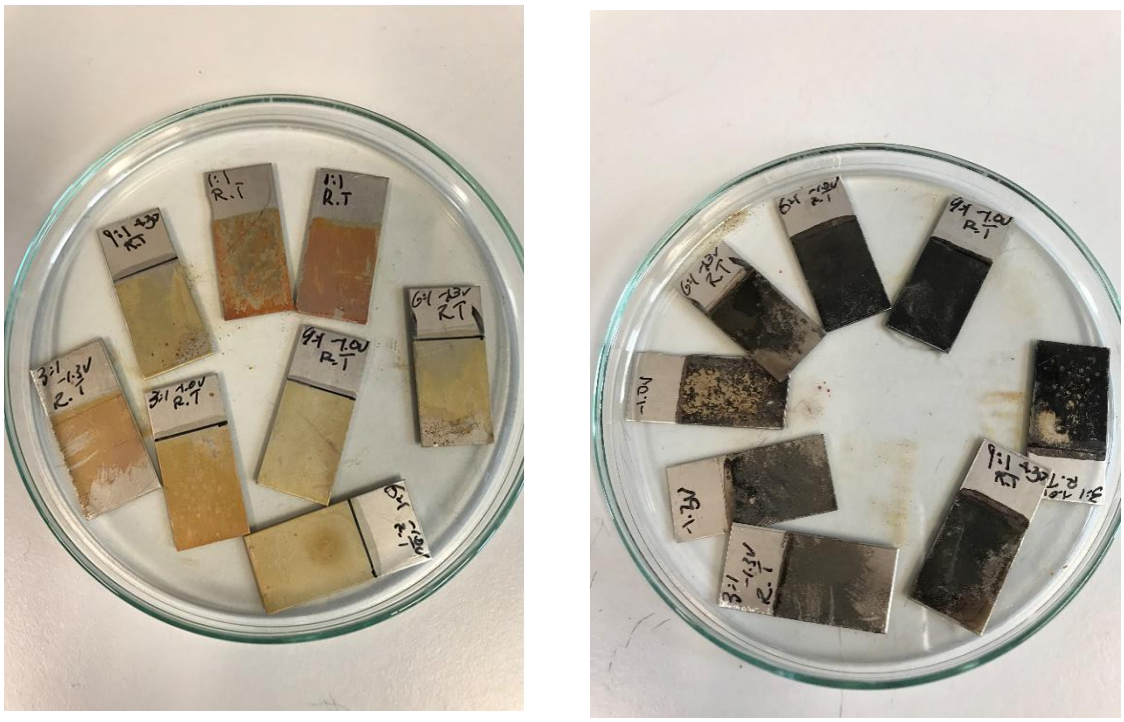

Figure 30. The NiFe electrodes coated in Experiment 2. Left: not yet cycled in KOH. Right: Already cycled in KOH.

3.2.2 SEM images and EDS mapping

The SEM images of NiFe hydroxide 3-1 deposited at -1.0 V and -1.3 V are shown in the Figure 31 and Figure 32, both potentials were measured against SCE. When the thin film was deposited at -1.0 V, it formed of evenly distributed layers of small micron scale particles (as displayed in Figure 31).

Poor adhesion and flaking were the main issues of using nickel nitrate and iron nitrate as deposition electrolyte, particularly when the deposition potential applied was -1.3V. As shown in Figure 32, when the deposition potential of -1.3 V was applied, a large area of stainless steel could still be observed, displaying very poor coverage of the NiFe hydroxide. Only some areas were covered by dense NiFe hydroxide, as illustrated in red circles in Figure 32. The reason of this was because when the thin film was deposited at -1.3 V, the coating was very non-adherent. Even a gentle movement would result in the peel of the film due to flow of air. In contrast, the film deposited at -1.0 V was more adherent. The possible route cause was that when -1.3V vs SCE was applied to the working electrode, the kinetics of HER was high so that it increased the rate of HER, producing large air bubbles which could adversely affect the formation of nickel hydroxide on the electrode surface and lead to adhesion issues. In addition, the EDS analysis showed that when deposited at -1.0 V, the content of Ni was twice as much as that when deposited at -1.3 V, which was also an indication of loss of nickel hydroxide.

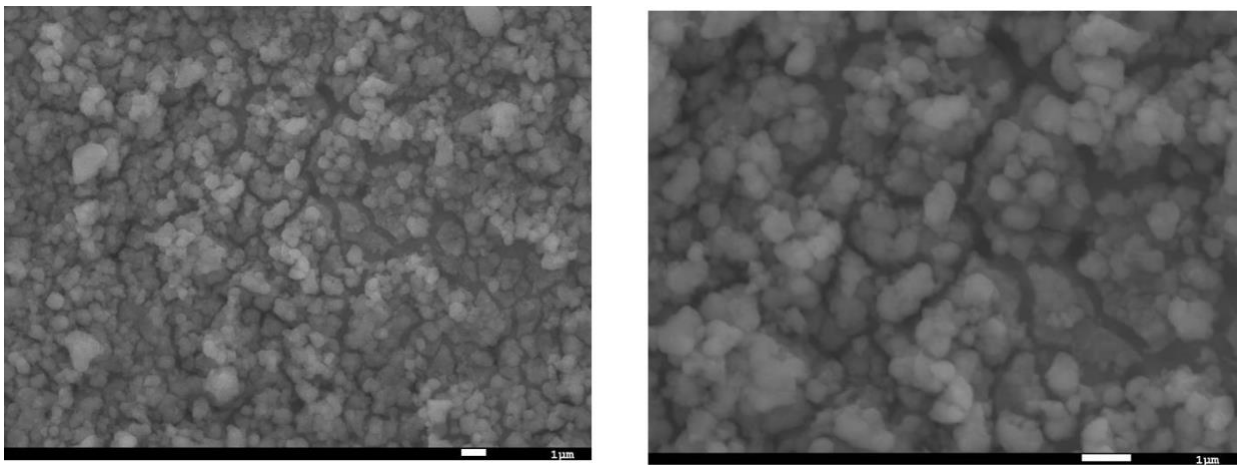

Figure 31. SEM images of NiFe hydroxide 3-1 deposited at -1.0V vs SCE, of which the magnification is x5000 (left) and x 10000 (right).

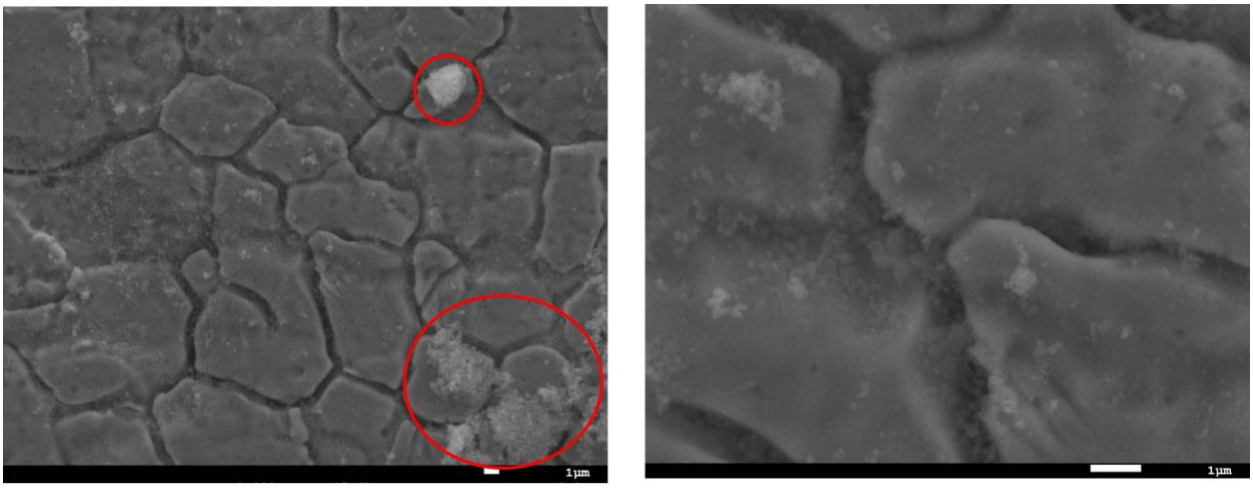

Figure 32. SEM images of NiFe hydroxide 3-1 deposited at -1.3V vs SCE. The magnification is x5000 (left) and x10000 (right).

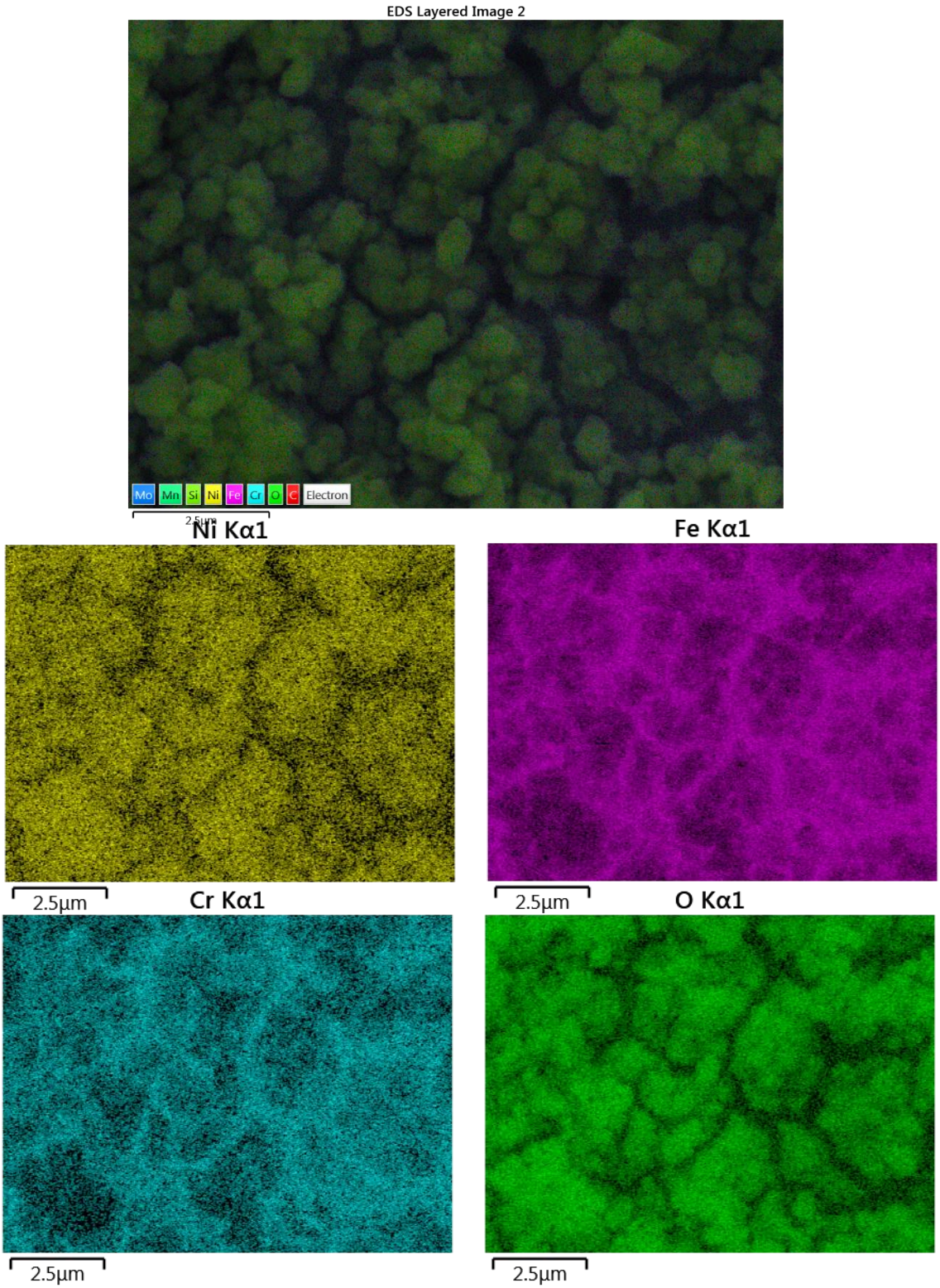

Figure 33. EDS mapping of NiFe 3-1 -1.0V vs SCE.

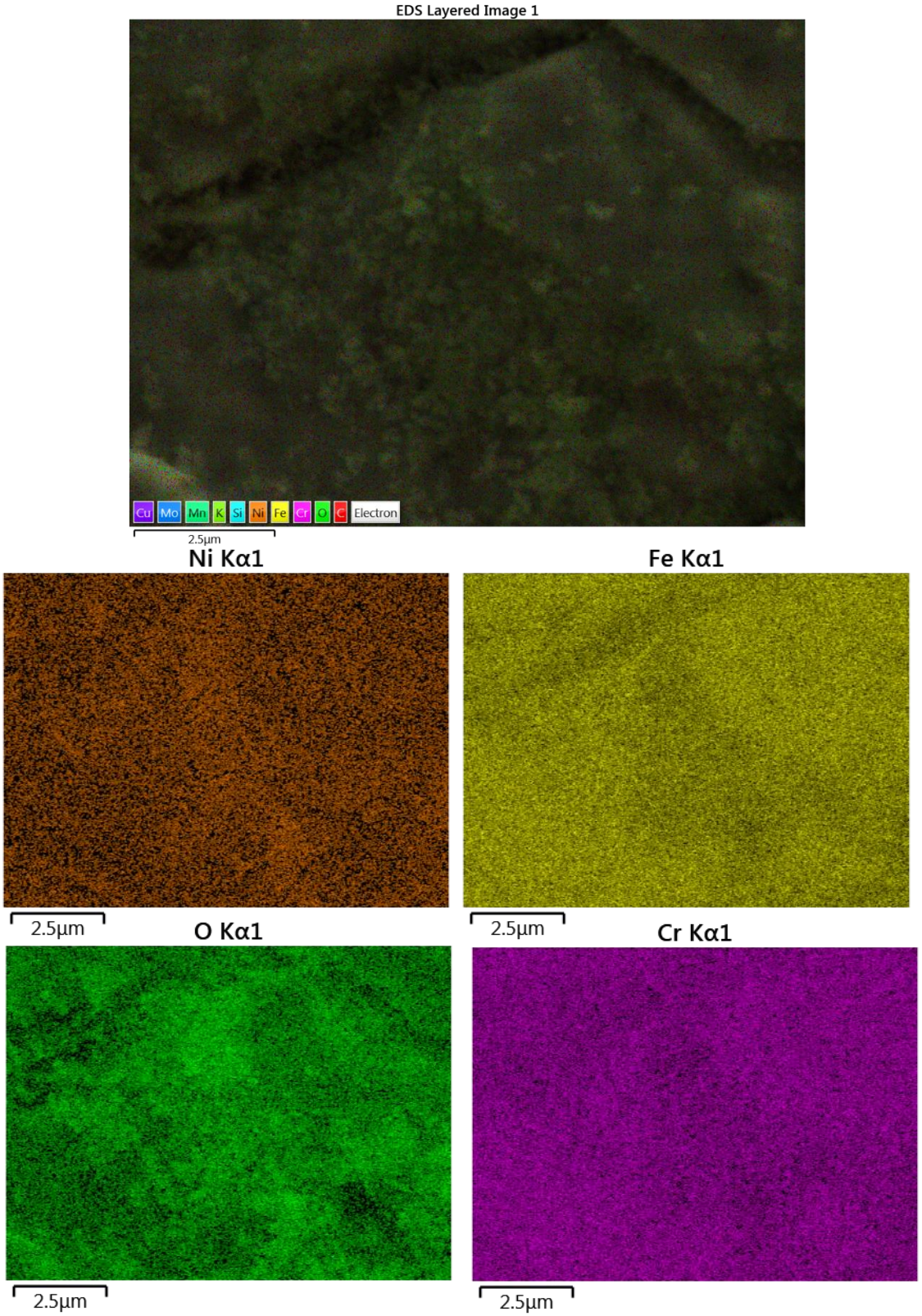

Figure 34. EDS mapping of NiFe 3-1 -1.3V vs SCE.

As shown in Figure 33, when -1.0V vs SCE was used to prepare electrodes, the SEM image shows evenly distributed micron scale particles on the stainless steel substrates. Particle cracking was also observed, which revealed that the condition under which the electrode was prepared was not optimised. According to the EDS mapping images, the main elements detected in particles were nickel and oxygen. This was the sign of the formation of nickel hydroxide. It was difficult to distinguish how much iron was present in the particles as the stainless steel also contained ~66% iron. Large fraction of iron detected was believed to be in stainless steel because the iron map and chromium map in Figure 33 look overlay, the chromium detected can be fully attributed to the stainless-steel substrates. Nevertheless, the successful coating of nickel hydroxide was evident. The elemental analysis showed that the electrode contained 26% nickel, which is much greater than the composition of nickel in bare stainless-steel.

When -1.3V vs SCE was used to prepare the electrodes, there was no obvious particles formed. There was only small amount of possible deposits present on the substrate. The Figure 34 shows that iron and chromium were denser than nickel in terms of elemental distribution. The presence of oxygen suggested that the formation of small amount of nickel hydroxide was formed. However, it only contained 13.4% of nickel, that was not significantly higher than bare stainless-steel electrode. The reason of this was peel or flaking of the deposits.

Elements	Bare electrode	NiFe hydroxide -1.0V	NiFe hydroxide -1.3V
Fe	66.3%	40%	57.5%
Ni	9.6%	26%	13.4%
Cr	15.9%	9.9%	13.8%
C	5.2%	5%	5%
O	0	17.3%	7%

Table 7. Elemental composition of Experiment 2 electrodes.

3.2.3 Electrochemical performance of OER

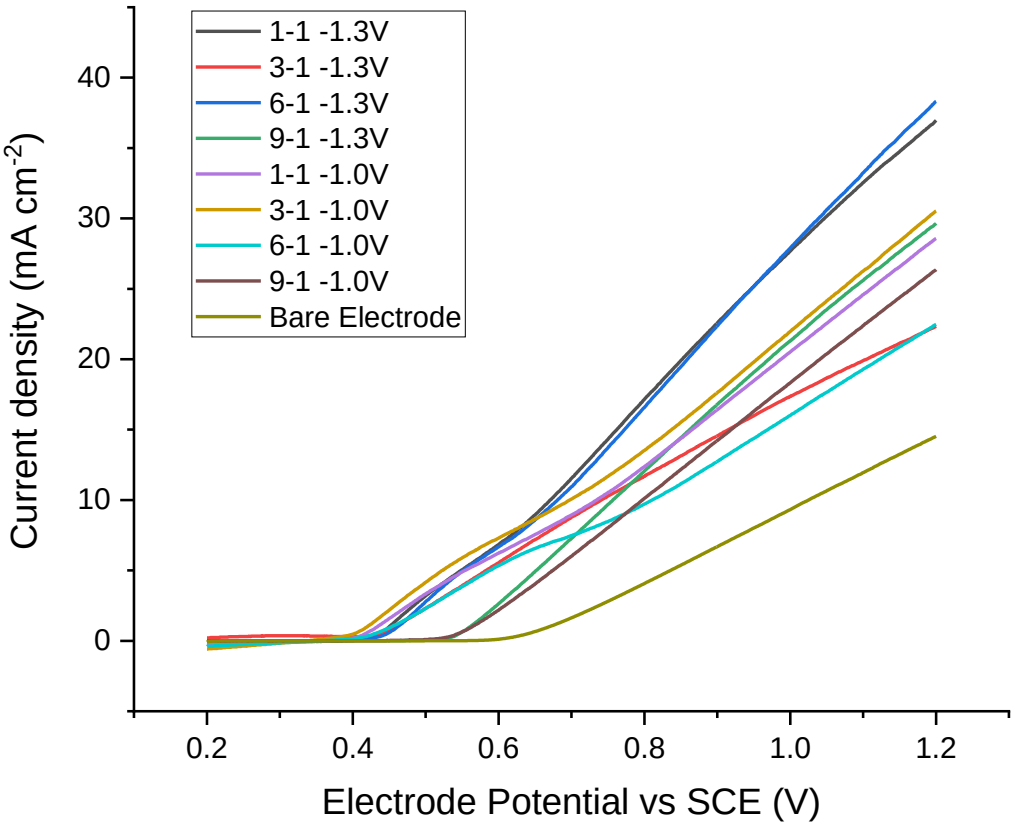

Figure 35. LSV plots of all NiFe films prepared in this experiment. The ratios of NiFe are 1-1, 3-1, 6-1 and 9-1. For each ratio the samples were deposited at -1.0 V and -1.3 V. The LSV plots were obtained by CV forward scan between 0.2 – 1.2V vs SCE, with scan rate of 20 mV/s. The electrolyte concentration was 0.1M KOH and the temperature was room temperature.

The LSV results shown in the Figure 35 displayed how current density changed with increased electrode potential. The current densities of all samples generated during OER laid within the range of 20 – 40 mA cm^{-2}, which was at least twice as much as bare stainless steel produced. This demonstrated that the thin films prepared in this experiment could be used as reliable OER catalyst in alkaline medium. Among all samples, NiFe 6-1 deposited at -1.3 V and NiFe 1-1 deposited at -1.3 V exhibited much higher current densities than other samples, it however was not sufficient enough to make conclusions that either NiFe ratio or deposition potential had any relationship with current density.

In Figure 35, it could also be observed that the OER onset potentials of majority of the prepared samples were approximately between 0.3 V to 0.4 V vs SCE. Two of them had the OER onset

potential of 0.5 V, and for the bare stainless steel it was 0.6 V. The figure clearly displayed that NiFe hydroxide films prepared in this experiment exhibited 200 – 400 mV smaller overpotentials

than bare stainless steel when the current density was 10 mA cm^{-2}. The overpotential of samples prepared in this experiment are shown in the Table 8.

Materials	Current Density at 1.2 V vs SCE (mA cm-2)	Overpotential vs SCE at 10 mA cm-2 (mV)
NiFe 1-1 -1.3V	36	671
NiFe 3-1 -1.3V	24	741
NiFe 6-1 -1.3V	39	681
NiFe 9-1 -1.3V	28	757
NiFe 1-1 -1.0V	28	735
NiFe 3-1 -1.0V	30	698
NiFe 6-1 -1.0V	24	811
NiFe 9-1 -1.0V	29	798
Bare stainless steel	15	848

Table 8. Electrochemical performances of all ratio of NiFe samples prepared in Experiment 2.

Based on the data in Table 8, all coated electrodes showed better electrochemical performance than bare stainless steel electrode because of higher current densities at 1.2V vs SCE and smaller overpotential at 10 mA cm^{-2}. However, there was no clear relationship between their electrochemical performances and the investigated parameters (Ni/Fe ratio and deposition potential).

It can also be observed that in Figure 35, the LSV of some electrodes, for instance 6-1 -1.0V electrode, there was a oxidation peak evident between 0.45 V to 0.7 V region, which was likely to be the oxidation of NiFe hydroxides to NiFe oxyhydroxide, however this redox reaction was not further investigated.

3.2.4 Stability test of the best performing sample

NiFe hydroxide 6-1 deposited at -1.3 V was used in this stability test. The conditions and methods used for stability test in this experiment were the same as those in Experiment 1. The trends shown in Figure 36 showed that initially the current density increased with time during the first 10000 seconds, then started to decline. Again, it was difficult to tell whether the reason of this material degradation, mass loss of the thin film, or bubble blinding was. During the 60 hours of stability test, the current density reached the highest on the second day, of which the current density was even higher than that measured in Experiment 1. However, it then never reached the same high current density again on day 3 and 4. Again, for each day, the current densities reduced with time because of the bubble blinding. High concentration of electrolyte and potential facilitated the oxygen bubbles evolution because they provided high mass transport rate and fast reaction kinetic of OER. The reduced stability could also be caused by the material peeling because of poor material adherence. The oxygen bubbles could remove considerable amount of material when they left the electrode surface. The strong evidence of this conclusion was that after the end of each day, the deposition material could be visually observed on the bottom of the electrolyte flask.

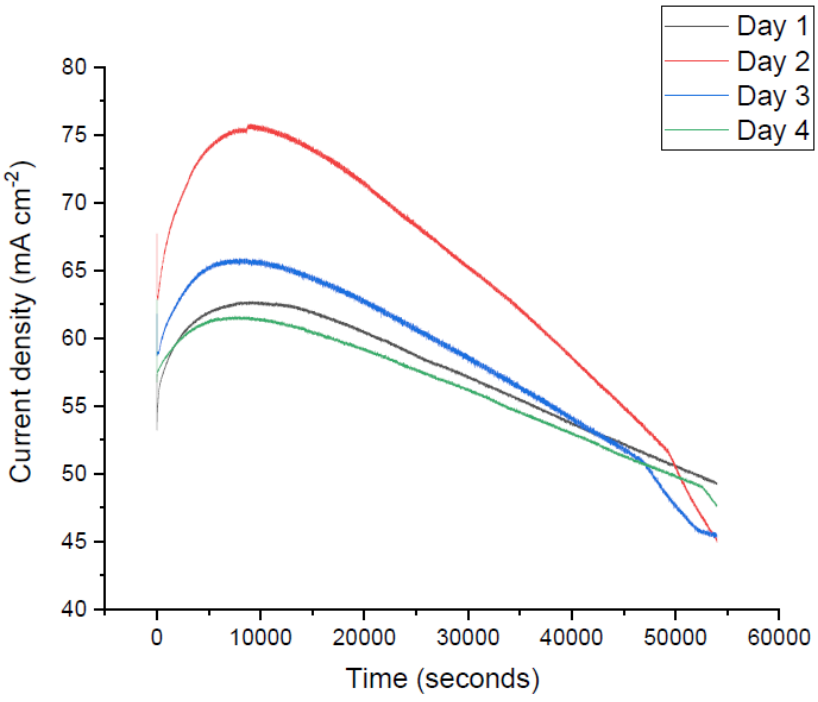

Figure 36. Stability test of NiFe 6-1 deposited at -1.3V vs SCE. The electrolyte concentration was 10g KOH in 1L water. The constant potential of 1.2V vs SCE was applied to working electrode for 15 hours for each day.

3.2.5 Conclusion

In conclusion, NiFe hydroxide films were successfully deposited on stainless steel substrate with various morphologies by electrodeposition method without using any chemical binder. The prepared NiFe electrode could be used as anode directly in alkaline solution electrolyser. The morphologies of the prepared NiFe films varied depend on the deposition condition such as Ni/Fe ratio of deposition solution and potential at which they were deposited. With presence of NiFe hydroxide thin films, the overpotential of OER were significantly reduced by 200 – 400 mV depending on deposition conditions in comparison with bare stainless-steel substrate. The electrode prepared in this experiment exhibited poor stability under high concentration of KOH, this was mainly due to the poor material adhesion and peel.

The poor adhesion of the material could be resulted in many factors. For example, it could be the inadequate removal of surface oxide. Prior to the material deposition, the stainless-steel substrates were cleaned by acetone and isopropyl alcohol, they were then sonicated in deionised water. By such cleaning procedure, any surface impurities such as oil and dust were adequately cleaned. However, it may not be sufficient to remove the oxide layers such as chromium oxide, which is the layer that makes stainless steel corrosion resistance.

Another two assumptive reasons that caused material flaking could be excessive coating thickness and interruption of electric current during deposition process, which could be due to air bubbles generated during HER. Thus, it was very important to further investigate the parameters that could affect the coating formation and the optimisation of the electrode preparation procedures.

3.3 Experiment 3: Doping of Fe on electrodeposited metallic Ni/Ni hydroxide in organic solvent

Apart from developing electrocatalyst material to enhance OER, the optimised design of such catalysts and the engineering to apply the catalyst on substrates also remain interesting to industries. As mentioned earlier, the ideal OER electrocatalysts would have high surface area which provides more active sites exposure. Moreover, the structure of catalyst should provide feasibility of mass transport, electron transfer and bubble removal. If the catalyst is too compact, the gas bubbles are no longer to escape from electrode surface through tunnels, that would ultimately increase the overpotential with operation time.

Inspired by the nature, Wei et al proposed a design of a NiFe material that they described it as 'dendritic nickel tree with Fe'. The SEM images of the material obtained by Wei et al are shown in Figure 37. The tree-branch like microstructure was expected to have network which facilitated mass transport and was electrically conductive [71]. The Experiment 3 intended to investigate if the success of producing dendritic nickel trees on nickel foam by Wei et al could be replicated to stainless steel.

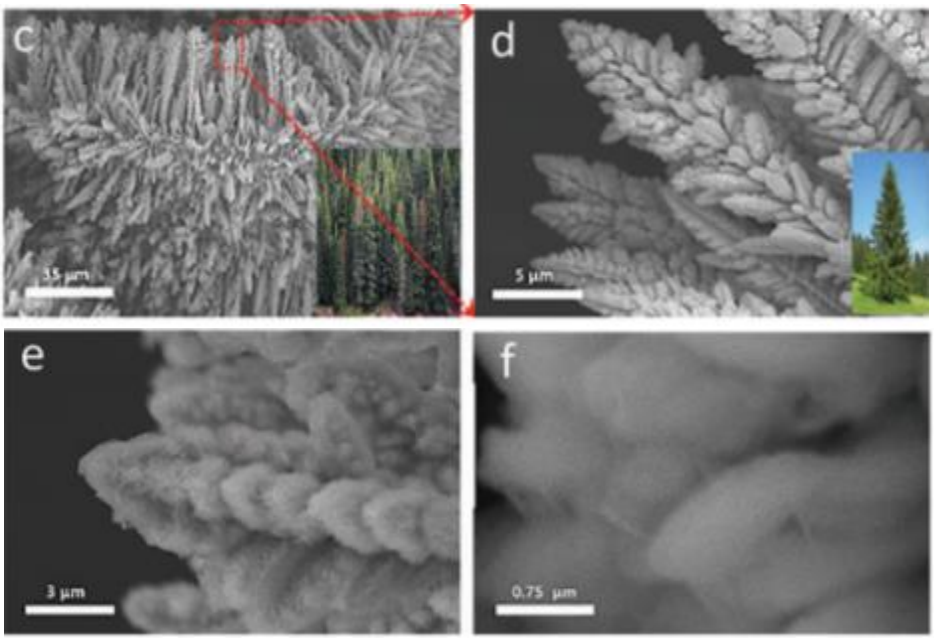

Figure 37. The SEM images of dendritic nickel tree obtained by Wei et al [71].

3.3.1 SEM images and elemental analysis by EDS

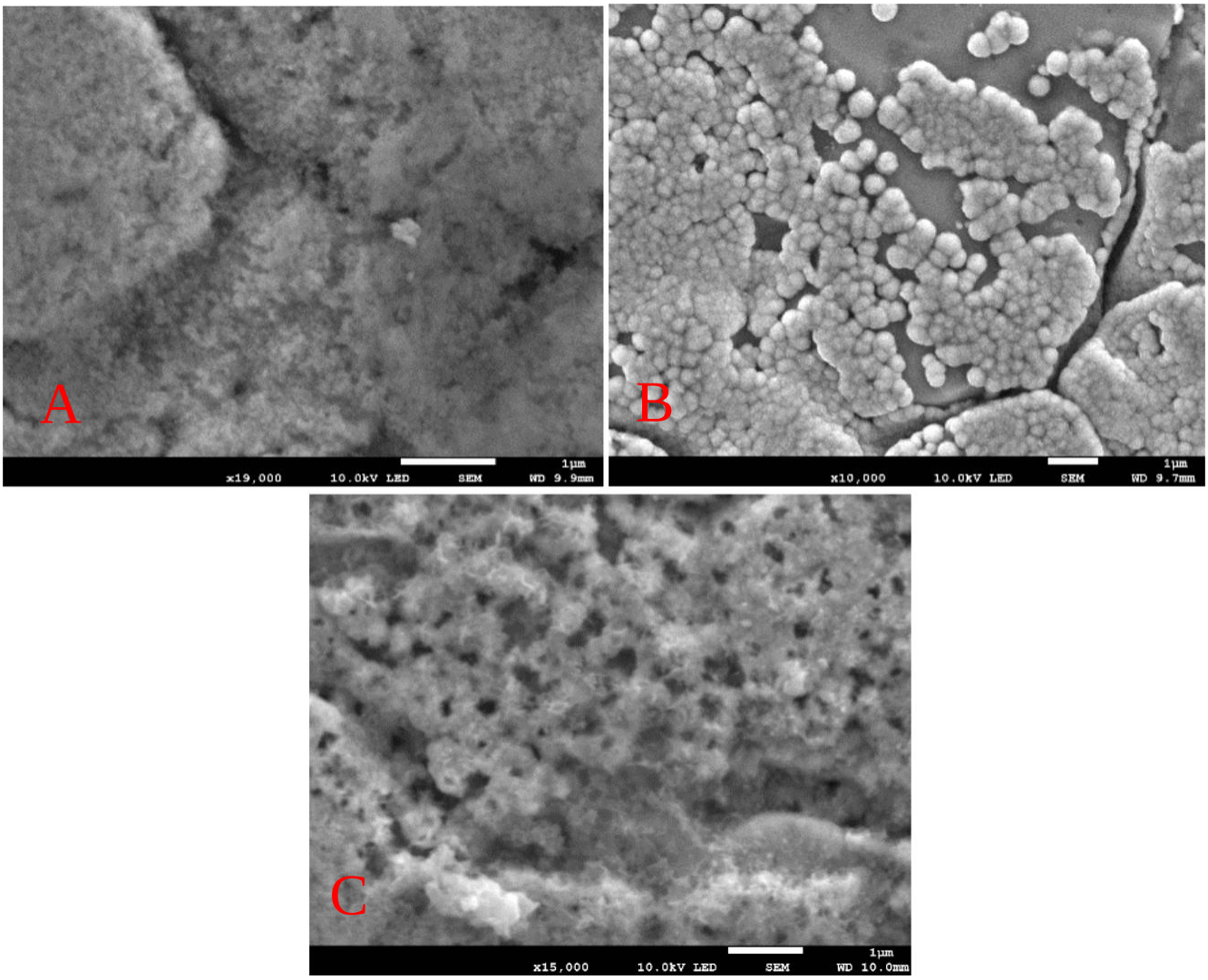

Figure 38. SEM images of A: nickel plated electrode; B: After heating in water; C: Fe doped $Ni(OH)_2$

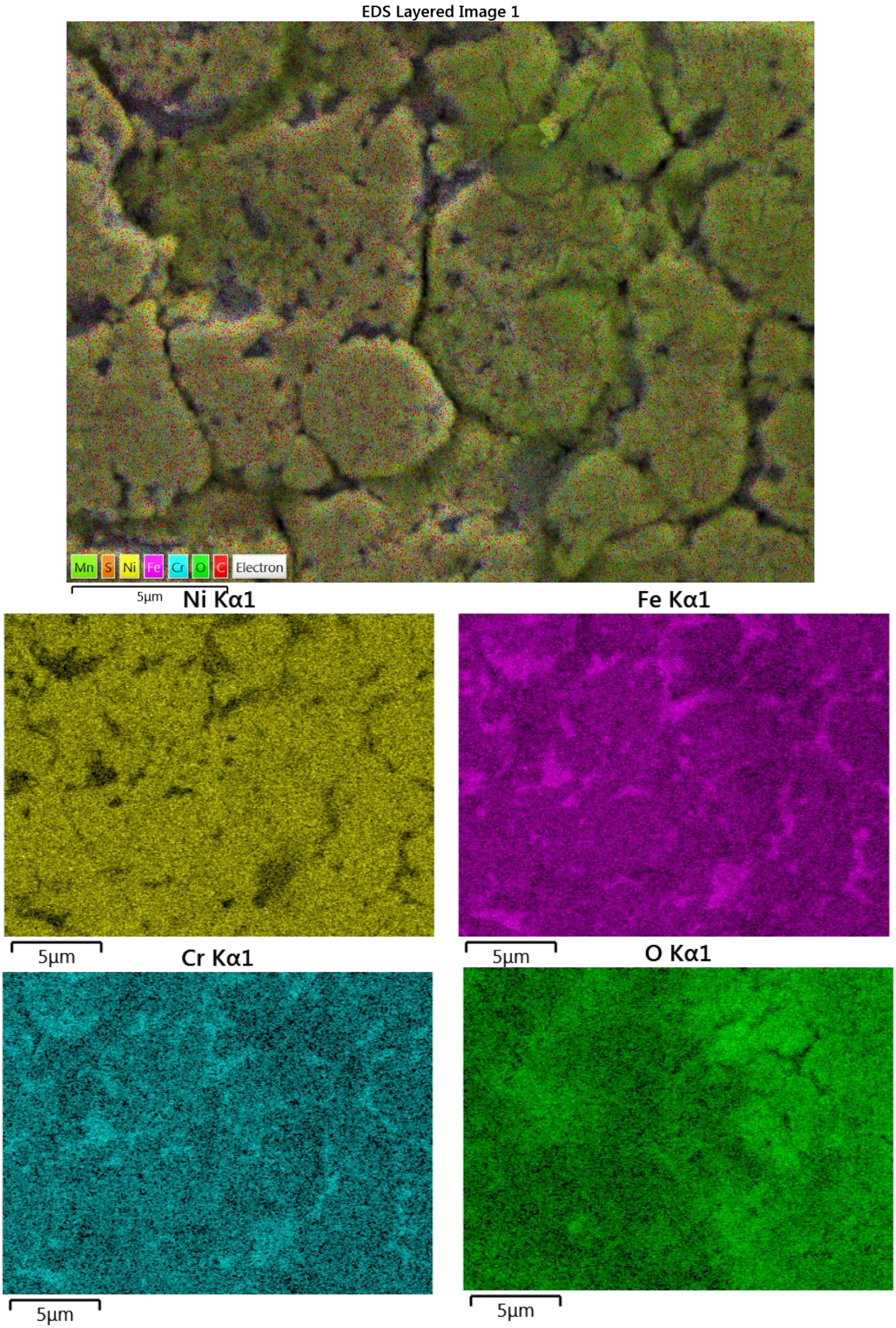

Figure 39. EDS mappings of Ni plated electrode.

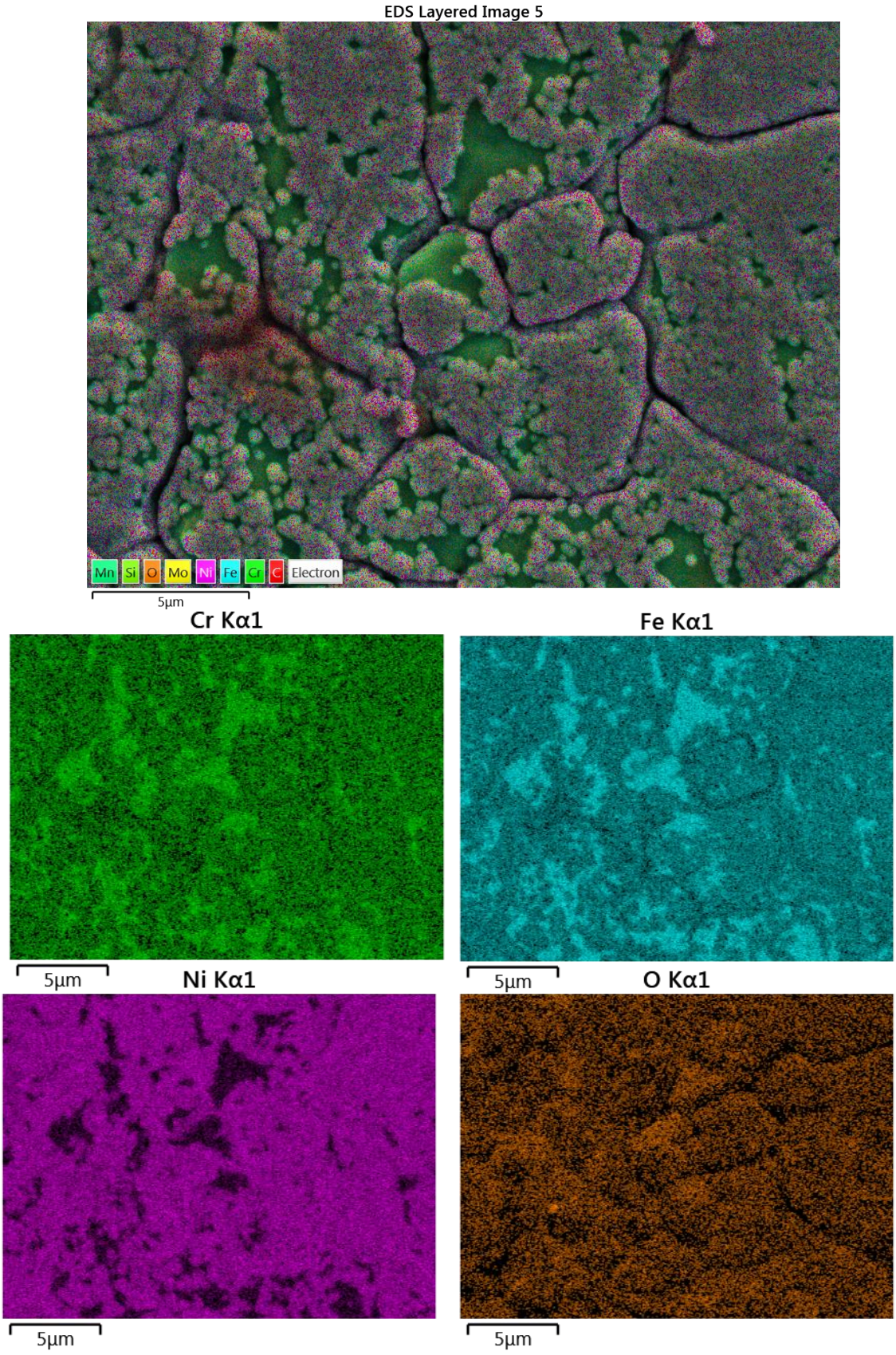

Figure 40. EDS mappings of electrode after heating treatment in water.

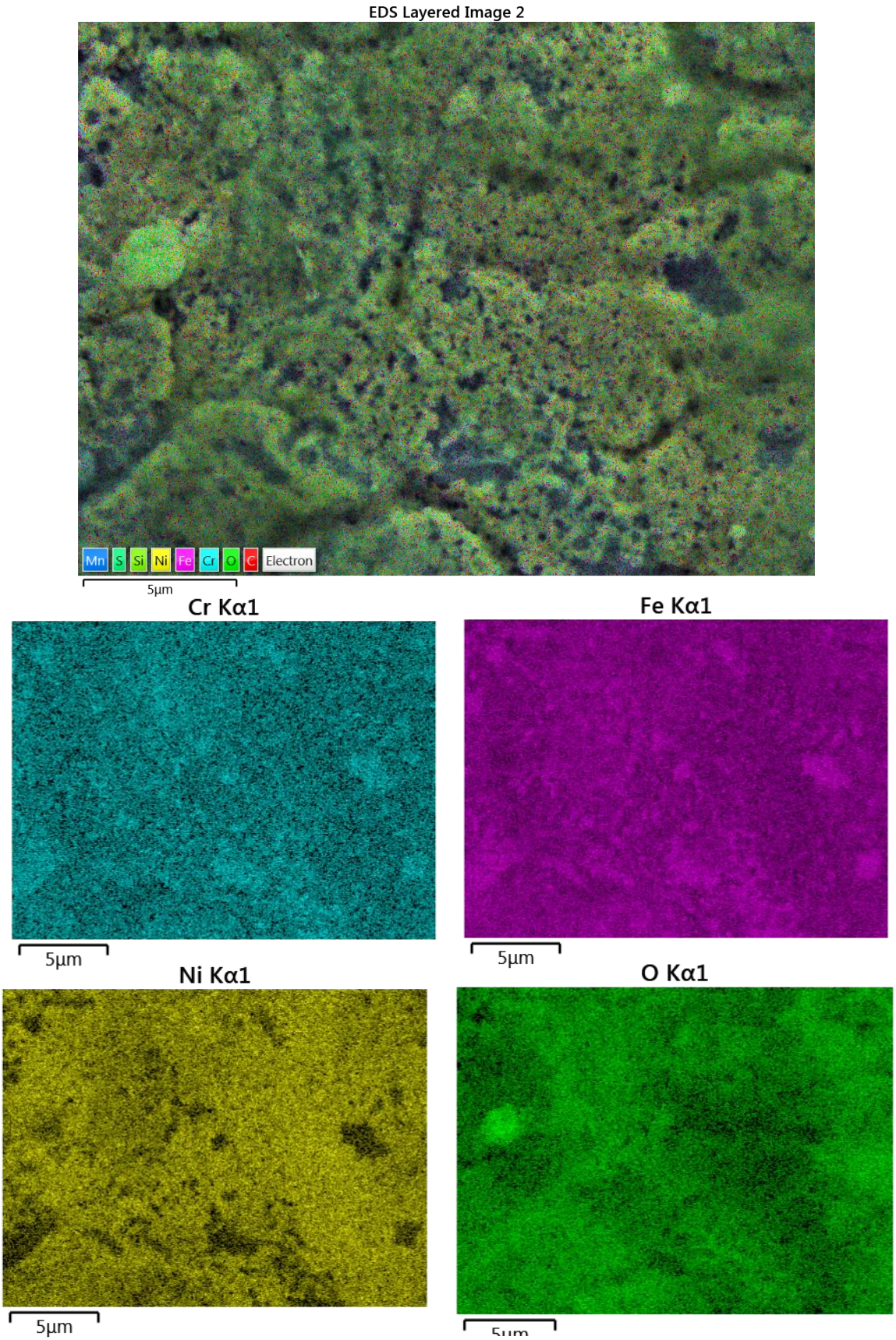

Figure 41. EDS mappings of Fe-doped $Ni(OH)_2$.

Elements	Bare electrode	Nickel metal	Intermediate Ni(OH)2	Fe-doped Ni(OH)2
Fe	66.3%	21.5%	25%	35.3%
Ni	9.6%	53.2%	58.6%	42.1%
Cr	15.9%	5.8%	6.7%	8%
C	5.2%	11.2%	7.6%	5.1%
O	0	7.4%	1%	8.1%

Table 9. Elemental composition of Experiment 3 electrodes.

From the SEM images, it was obvious that after first electrodeposition of nickel. It was expected that nickel metal would be formed on the substrate, as Figure 38(A) shown. The coating material consisted of nickel compounds evenly plated on substrate. The plated coating material contained high nickel level, which was 53.2% according to the EDS data. 7.4% of oxygen atom was detected by EDS which suggested that the material was not purely metallic nickel but oxygen-containing nickel compound, either nickel oxide or nickel hydroxide. After the material was heated in water, the hydrothermal treatment caused partial loss of coating material, as shown in Figure 38 (B). The EDS data showed only 1% of oxygen atom which proved the loss of nickel compound. At the final step, the electrodeposition produced iron onto the nickel-based coating.

3.3.2 Electrochemical performance

The LSV results showed that nickel metal alone and nickel hydroxide only enhanced OER for a small degree, whereas doping Fe into nickel hydroxide would enhance OER further.

For nickel coated electrode (black plot in Figure 42), there was a small but noticeable anodic peak occurring at 0.4 V vs SCE, that indicated the oxidation of nickel oxide/hydroxide to nickel oxyhdroxide, during which the oxidation state of nickel was increased from 2+ (in nickel oxide or nickel hydroxide) to 3+ (in NiOOH). After heating in water (red curve), the reaction reported by Wei et al. that metallic nickel was transformed to nickel hydroxide by weak oxidation power of water was not evident in this Experiment. It displayed a slightly declined current density at 1.2 V vs SCE compared to the black plot, which was caused by partial loss of coating material. However, after doping Fe(II) onto nickel hydroxide, an improved OER activity could be observed (the blue plot). The LSV of these electrodes are shown in Figure 42.

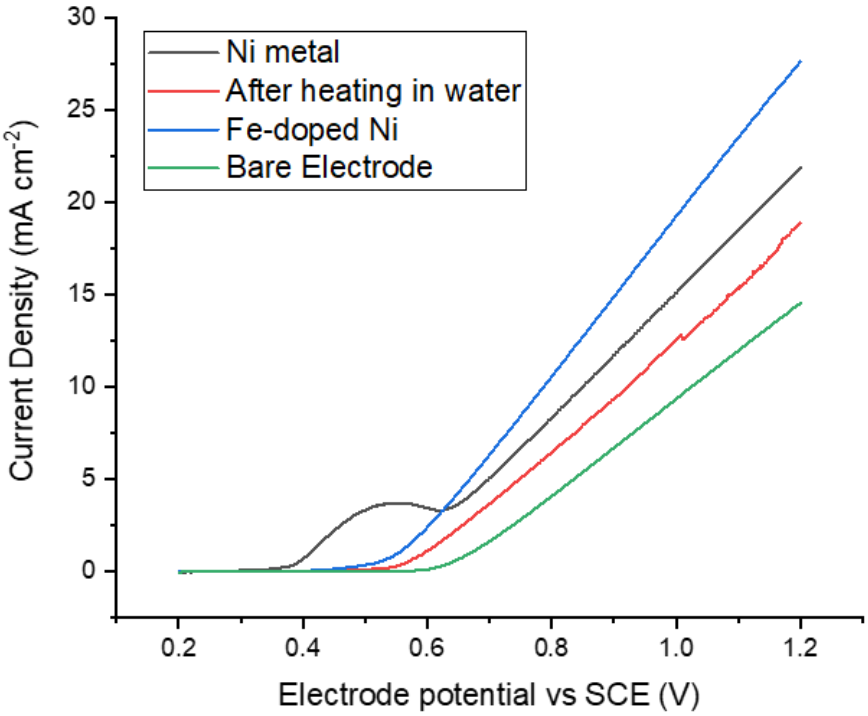

Figure 42. Linear Sweep Voltammograms of electrodes prepared in Experiment 3. The LSVs were obtained from forward scan of CV between 0.2 – 1.2V vs SCE, at room temperature, 0.1M KOH and 20 mV/s scan rate.

The electrochemical performance of the electrodes can be quantified in Table 10.

Materials	Current Density at 1.2 V vs SCE (mA cm-2)	Overpotential at 10 mA cm-2 (mV)
Ni	22	668
Fe-Ni(OH)2	27	628
Bare stainless steel	15	848

Table 10. Electrochemical data of Experiment 3 electrodes.

The initial nickel material reduced the overpotential by approximately 200 mV at 10 mA cm^{-2} compared to bare stainless steel. It also generated almost doubled current density at 1.2V vs SCE. The presence of mixed Ni^{3+} and Ni^{4+} played a role in improved OER activity. The change of oxidation state was due to the phase transformation of $Ni(OH)_2$ to NiOOH. Similar to NiFe electrodes fabricated in Experiment 1 and 2, the main mechanisms during OER were proceeding by following steps: 1) the formation of α-$Ni(OH)_2$ when the electrode was just submerged in KOH electrolyte; 2) transformation of pristine material to β- and γ- NiOOH at certain potential before

OER could begin. The exact potential at which the phase transformation occurred in this experiment was unknown. Some papers suggested that this potential could be as low as 450 mV verses Hg/HgO [72].

3.3.3 Stability test of Fe – doped Ni $(OH)_2$

The results of stability test of Fe – doped Ni $(OH)_2$ is shown in the Figure 43. There is no difference in the trends of the plots compared to the stability test results obtained for other samples. However, the main difference is that the current density measured on day 2 onwards dramatically increased compared to that measured on day 1. During day 1, the Fe-doped $Ni(OH)_2$ was activated and sufficiently transformed to γ-NiOOH, which was the possible reason of improved current density from day 2 to 4. From day 2 to 4, the current density of each day overlapped each other, which indicated that the material was fully activated and transformed. This was also a sign that there was no decline in performance of the catalytic material caused by material degradation or flaking. The reduction of current density during each day could be attributed to the resistance caused by gas bubble generation. One observation could be investigated later one was that during day 2 and day 3, the current density became unstable for a short period time. As green and blue plots shown in Figure 43, the instability lasted for roughly 3.5 hours on day 3 and much longer on day 4 (~ 8 hours). If there was opportunity to repeat the experiment, it would be useful to use the impedance spectroscopy investigate the charge transfer impedance growth, as the fluctuations at the beginning of the blue and green plots showed sign of interrupted charge transfer.

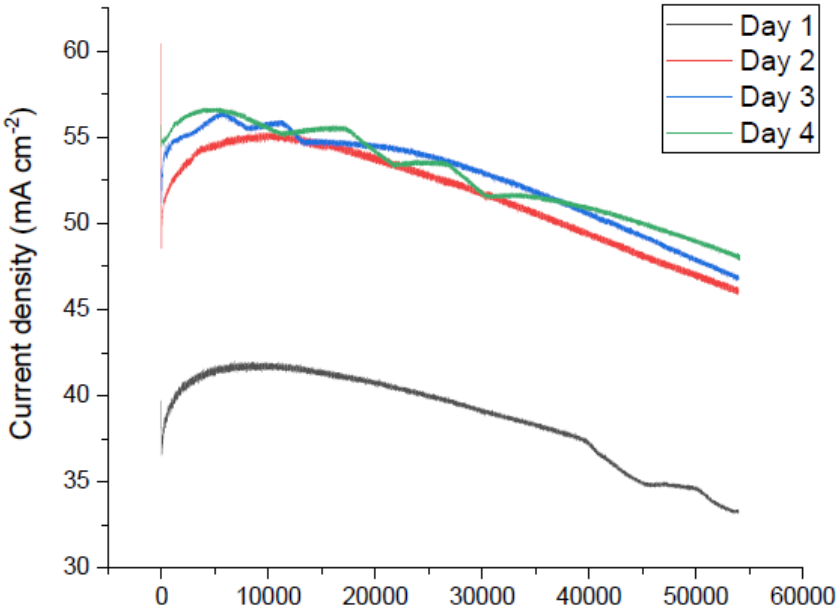

Figure 43. Stability test of Fe-$Ni(OH)_2$ electrode. Constant potential of 1.2V vs SCE was applied to working electrode for 15 hours each day, under room temperature. The electrolyte concentration was 10g KOH in 1L water.

3.3.4 Conclusion

As the standalone conclusion of Experiment 3, the Fe-$Ni(OH)_2$ electrode exhibited better OER activity than bare stainless steel in terms of both overpotential at 10 mA cm^{-2} and current density at 1.2V vs SCE. The fabrication time of the electrode was a bit longer because it consisted of 2 separate electrodeposition processes and a thermal treatment to produce intermediate. The experimental procedures used in Experiment 3 were very similar to those used by Wei et al., however the results were very different because the expected nickel dendrite trees were not evident according to the SEM images, whereas Wei et al. obtained perfect dendritic structure. It was assumed that the structure of substrates played a key role because nickel foams used by Wei et al. had porous 3D structure, however stainless steel was planar 2D substrate.

One benefit of separated electrodeposition of nickel and iron was mitigating the effect of anomalous codeposition, which was mentioned in the results and discussion section of Experiment 1. The anomalous codeposition effect favoured the reduction of more active species, that was Fe in a NiFe system. The consequence could be more Fe^{2+} was reduced and excessive Fe could even cover the OER active sites of nickel. Separated electrodeposition enabled precise control of Fe concentration and therefore Ni:Fe ratio.

The stability test data were also suggested that the Fe-$Ni(OH)_2$ electrodes fabricated by this experiment could potentially be utilised as anode material in industrial alkaline electrolyser due to its good stability. During each day, the electrodes sustained high current density and exhibited small current reduction over 15 hours, that could be the evidence of better bubble removal by the material.

3.4 Experiment 4: Thermal deposition of NiFe LDH

NiFe layered double hydroxides have only been widely studied as OER catalyst in recent years although successful synthesis of LDH materials were achieved much earlier. Like other metal hydroxides, one of the disadvantages of LDHs is their poor electrical conductivity. Therefore some research groups synthesis NiFe LDH on an carbon nanotubes [95]. However, using carbon nanotubes is not a compromising approach to improve the electrochemical performance of LDH due to its high cost. In Experiment 4, attempts were made to synthesis NiFe LDH by hydrothermal process.

3.4.1 SEM images and elemental analysis by EDS

The ammonium fluoride was mistakenly missing during the initial attempt to produce NiFe LDH. The SEM images in Figure 44 showed very different molecular structures when LDH was synthesised with and without NH_4F, which acted as etching agent. The separated layered structure was evident in the image on the left, where NH_4F was added.

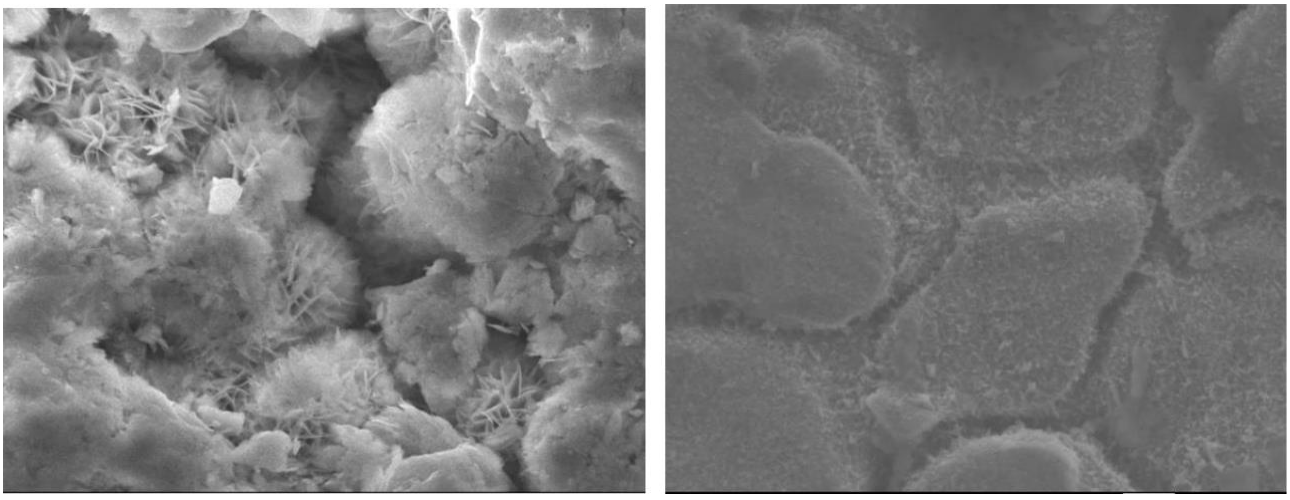

Figure 44. Morphologies of NiFe LDH; Left: when ammonium fluoride was added, and right: ammonium fluoride was not added.

The elemental composition of all elements detected by EDS are summarised in Table 11. When NH_4F was added, very high nickel concentration was detected even though the ratio of nickel and iron ions in solution was 0.5 mmol: 0.5 mmol. 23.% oxygen element detected also proved successful growth of hydroxide compounds. The chromium concentration was only 0.9%, which may reveal that thick LDH coating was formed, and the substrate surface was substantially covered by the coating. Without carbon support, it was predicted that this electrode would only generate very small current density because of poor electrical conductivity of LDH. When NH_4F

was missing, there was no significant difference in elemental ratio from bare stainless steel except nickel level was a bit higher, which indicated very limited growth of NiFe hydroxide on substrate.

Elements	Bare electrode	NiFe LDH 0.5:0.5, with NH4F	NiFe LDH 0.5:0.5, without NH4F
Fe	66.3%	11.9%	61%
Ni	9.6%	58.4%	14.1%
Cr	15.9%	0.9%	13.2%
C	5.2%	3.1%	4.8%
O	0	23.7%	4.8%

Table 11. Elemental composition of Experiment 4 electrodes.

3.4.2 Electrochemical performance

The LSV of NiFe LDH 0.5-0.5 with NH_4F is shown in the Figure 45. The cyclic voltammetry was used between 0.2 – 1.2V vs SCE, with scan rate of 20 mV/s. Only oxidation scan was displayed in the Figure 45. As the figure displayed, after 5 consecutive scans, it still exhibited a very low current density (less than 10 mA cm^{-2}). There was no sign of further improvement. As predicted, this was caused by low conductivity of LDH. The thickness of the coating prevented sufficient mass transport pathway, therefore it hindered electron transfer from substrate to the interphase between catalyst and electrolyte and resulted in low reaction kinetics of OER.

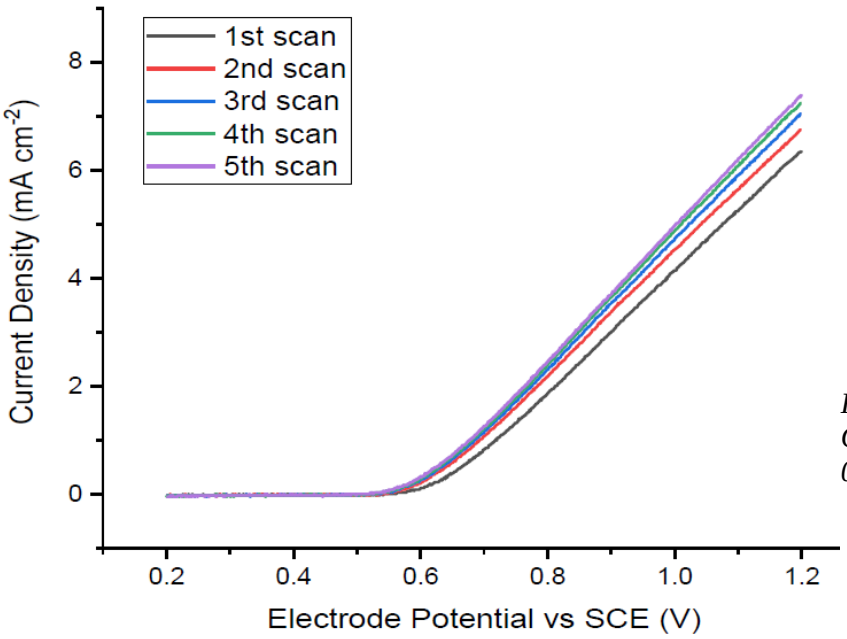

Figure 45. First 5 forward CV scans of NiFe LDH 0.5-0.5.

Surprisingly, when NH4F was not used, the electrode generated much higher current density, as Figure 46 showed. Although there was limited amount of NiFe hydroxide coating was formed without the etching effect by NH_4F, even small amount of the nickel hydroxide active sites was able to improve the OER. The numerical data were quantified in Table 12.

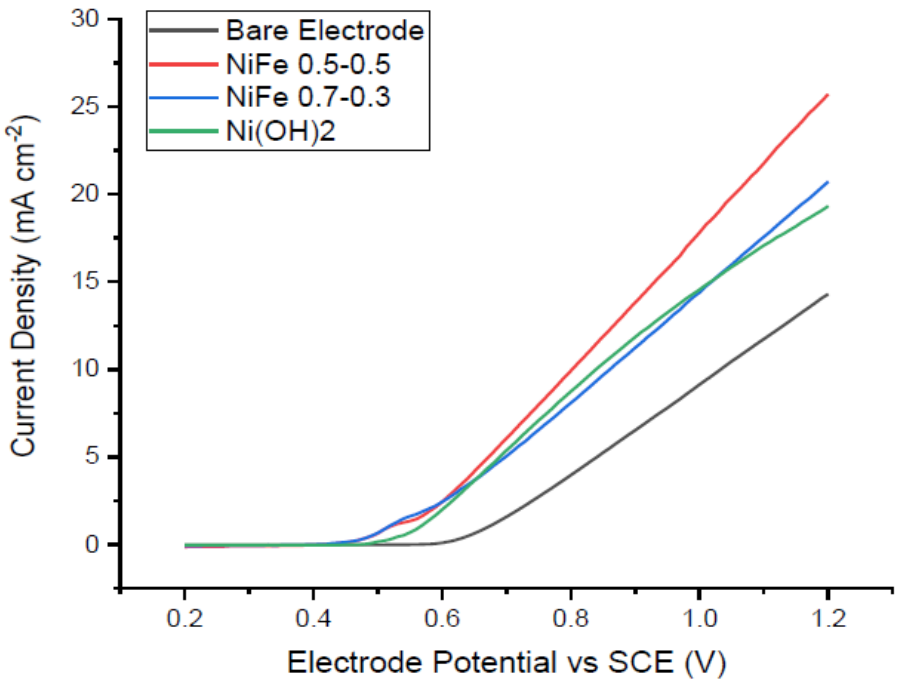

Figure 46. Linear Sweep Voltammograms of NiFe LDH electrodes prepared in Experiment 4. Obtained by forward CV scans between 0.2 – 1.2V vs SCE, under room temperature, 0.1M KOH, scan rate of 20 mV/s.

Materials	Current Density at 1.2 V vs SCE (mA cm^{-2})	Overpotential at 10 mA cm^{-2} (mV)
NiFe 0.5-0.5 no NH_4F	26	648
NiFe 0.7-0.3 no NH_4F	21	678
$Ni(OH)_2$ alone	19	668
Bare stainless steel	15	848

Table 12. Electrochemical data of Experiment 4 electrodes.

3.4.3 Conclusion

Although NiFe LDH has been attracted much research attention and a good candidate of OER electrocatalyst, it still suffers poor electrical conductivity when synthesised by single step hydrothermal method on stainless steel substrate. Although some literature reported excellent OER activity by NiFe LDH, the majority of them used nickel foam as substrate, which was a 3D porous substrate with very high surface area to volume ratio. When stainless steel substrate is used, the NiFe LDH synthesised by hydrothermal deposition tends to build up and grow a thick coating layer. Thick NiFe hydroxide layer not only hindered mass transport of reactant to the catalyst active sites, but more importantly, it created very high resistance that acted as a barrier to electron transfer. To overcome such high resistance, much higher overpotential would be required to achieve certain current density. Thereby the efficiency of electrolysis would be much lower.

Tremendous effort is required to optimise the synthesis process of NiFe LDH on 2D plane substrate such as stainless steel with some key design considerations. For example, the optimum Ni:Fe ratio, the engineering design on nanostructure improvement which ensure high availability of catalyst active sites.

Research has focused on improving conductivity by synthesising them on more conductive substrate or templates such as graphene and carbon nanotube. However, using carbon – based materials to improve its electrical conductivity would further increase the material cost and not commercially beneficial for industry – scale electrolyser anode materials. Thereby, it remains a challenge to seek alternative conductive additives that satisfy some key requirements. For example, they must be low cost and must be electrochemically stable under operational potential.

3.5 Full cell electrolyser test

The NiFe hydroxide prepared by Experiment 1 was selected to be an anode candidate for a single cell electrolyser test. The set-up of the electrolyser rig is shown in the Figure 47. The rig consisted of anode and cathode, both of which were CPH2 standard stainless steel 316. Other components include a gasket and a separator. The electrolyte in the beaker was 0.1 M KOH solution. The electrolyte concentration was much smaller than that of commercial scale electrolyser, which is usually between 10-30 wt% KOH [96]. The electrolyte was delivered to the electrolyser by a pump via the rubber tube. The outlet electrolyte in another tube contained the mixture of hydrogen and oxygen.

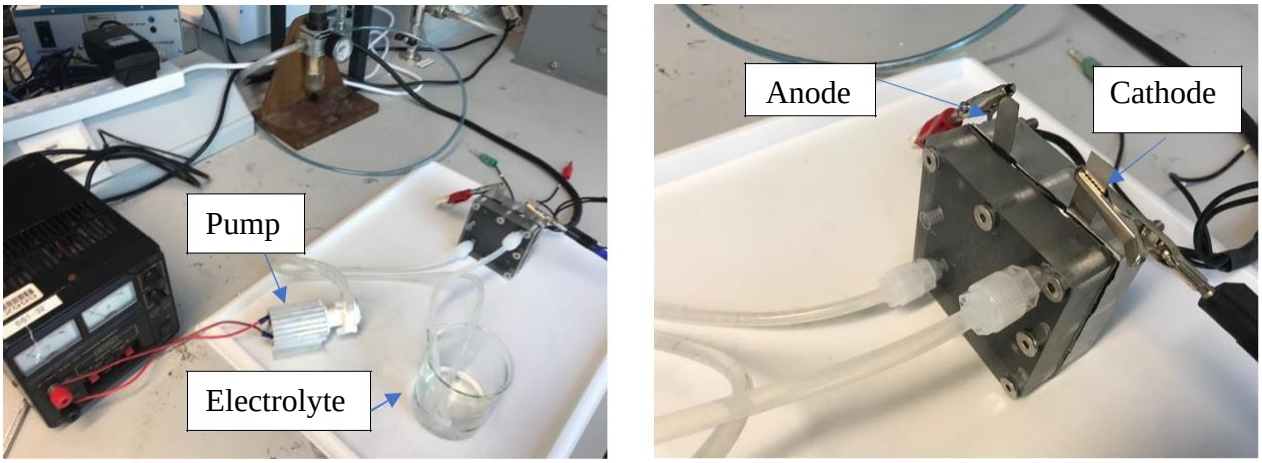

Figure 47. The setup of electrolyser unit for full cell testing.

The CV was recorded in 0.1 M KOH between 0.6 – 2.0 V of cell voltage at room temperature, the scan rate was 50 mV/s. The NiFe hydroxide plot in Figure 48 indicated that there was an initial reaction took place between 1.2 – 1.6 V, which was possibly simultaneous reactions of Ni(II) → Ni(III), Fe(II) → Fe(III), and OER. Another obvious peak was observed at 2.0 V, which could be OER. In comparison, the bare electrode (black line) generated much less current and the bare electrode curve elevated very slowly. At 2.0 V, bare electrode only generated 2.4 mA current, whereas NiFe hydroxide deposited electrode generated 12.5 mA, more than 5 times as much as bare electrode. During reverse scan, a reduction peak was observed at 1.05 V, which corresponded to the reduction of Ni(III) → Ni(II).

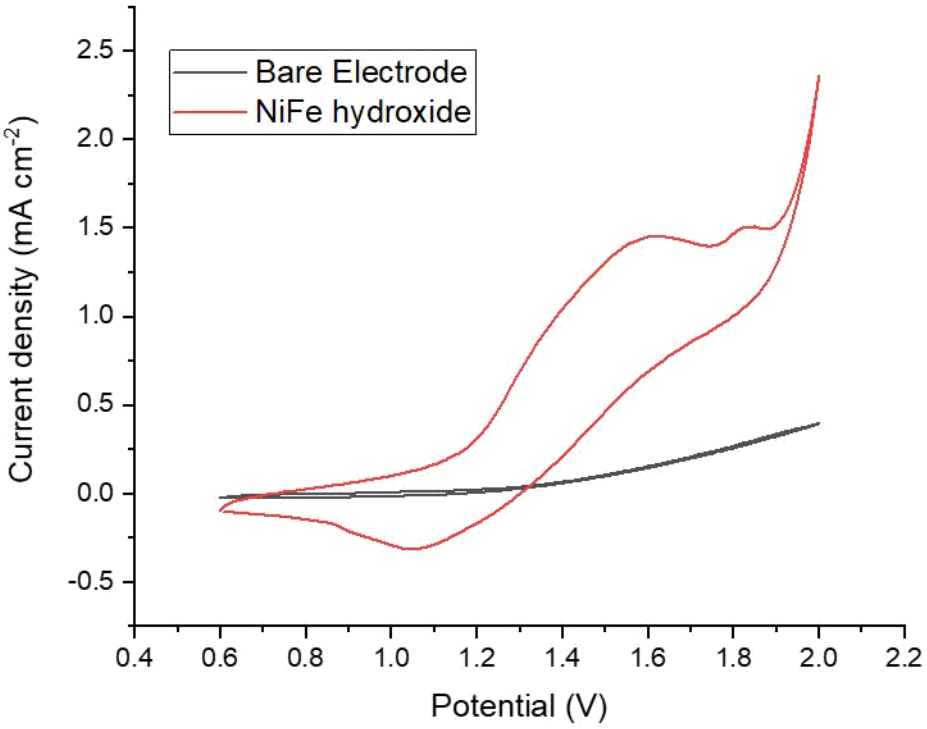

Figure 48. Cyclic Voltammetry of stainless-steel cathode vs bare stainless-steel anode (black plot) and stainless-steel cathode vs NiFe hydroxide deposited anode (red plot). The CV was scanned between 0.6 – 2.0 V cell potential.

The chronoamperometry technique was also used to the electrolyser rig, where 1.6 V was applied to the electrolyser for 30 minutes. The current responses were recorded as shown in the Figure 49. The figure displayed that the response of bare electrode fluctuated and exhibited poor stability. According to Figure 49, at 1.6 V the current response of NiFe electrode was the combination of surface reaction as well as OER. At this voltage, the OER is only low intensive process. The bare electrode exhibited irregular response at 1.6 V which revealed that there was no obvious surface reaction occurring and had very low current responding to OER. Although some factors may affect this result such as the partial blockage of gasket channel and flow rate of the electrolyte, under the same condition, NiFe deposited electrode exhibited a much more stable response when same potential was applied and lasted for same duration. The generated current exhibited no obvious fluctuation except at around 1500 second due to loss of electrolyte at the time. After the electrolyte was resupplied, the current went back to normal (approximately 5 mA).

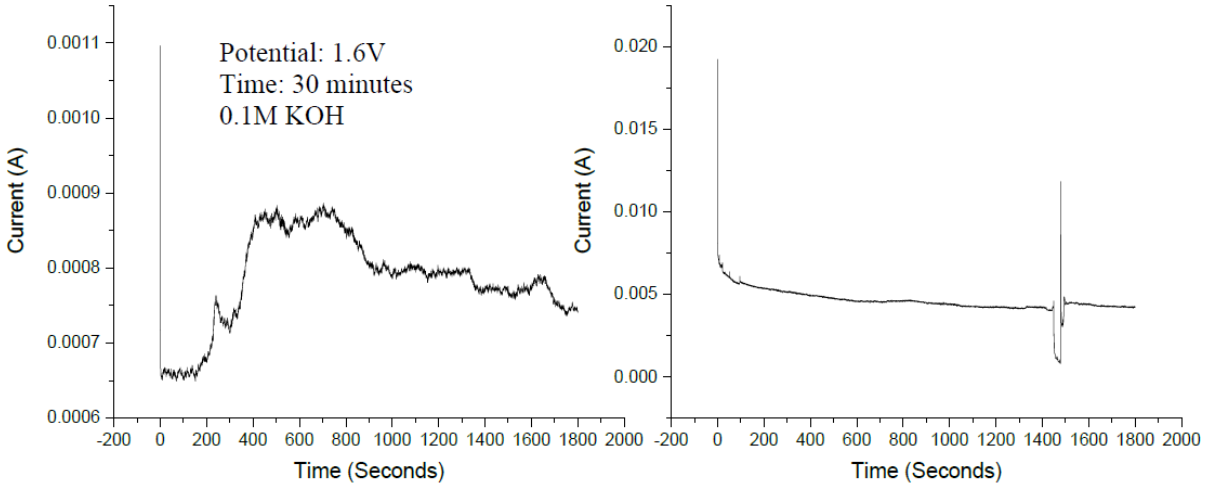

Figure 49. The chronoamperometry plots of left: bare electrode anode.; right: NiFe hydroxide coated anode. Constant potential of 1.6V was applied to electrodes for 30 minutes.

The charge—time plots were obtained for both bare electrode and NiFe hydroxide deposited electrode during 30 – minute electrolysis and shown in the Figure 50. These plots could help to calculate the amount of oxygen electrochemically produced during 30 minutes by using Faraday's law of electrolysis. In both plots, the charge produced increased linearly with time, indicating that the charge produced on both electrodes increased linearly with time (this includes charge accumulation within capacitance of double layer and gas evolution beyond capacitance of double layer). NiFe deposited electrode produced more than 8 C charge within 30 minutes whereas bare

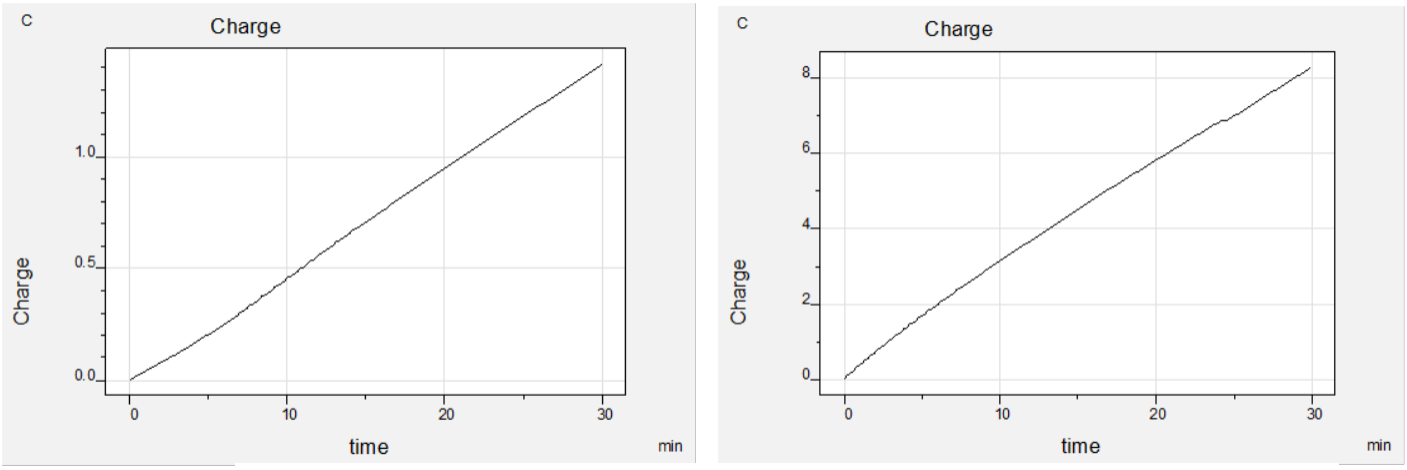

Figure 50. The charge vs time plots of left: bare electrode, and right: NiFe deposited electrode.

electrode only produced approximately 1.4 C charge within the same duration. The theoretical mass of oxygen produced can be calculated directly by counting the quantity of charge in coulombs passed during the electrolysis process. This was initially stated in Faraday's law of electrolysis, of which the equation is:

$$m = \frac{I \cdot t \cdot M}{nF} \qquad Equation\ 34$$

By definition, the quantity of charge Q equals current multiplies by time, therefore the equation can be simplified as:

$$Q = nFN \qquad Equation\ 35$$

Where Q = total charge accumulated, coulombs

n = number of electrons, for OER there are 4 electrons for each mole of O_2 produced

F = Faraday's constant

N = moles of gas produced, which equals to m/M

I = the current passes during electrolysis

t = electrolysis time

m = mass of the product

M = molar mass of the substance, for O_2, M = 16

By using the Equation 35, the theoretical volume of oxygen produced during 30 minutes by NiFe hydroxide coated anode was 0.48 ml, assuming 100% faradaic efficiency. For bare electrode, there was no oxygen produced because the voltage applied was not high enough for OER to occur. As a correction, 2.0V should be used to both bare stainless steel and NiFe hydroxide coated electrode. As shown in cyclic voltammogram in Figure 48, the OER started to happen when the scanned voltage reached 2.0V, which should be used in amperometry test.

To make the calculation above meaningful, there would be a very important assumption, that is the current efficiency is 100%, which means that all current produced contributes to the redox reaction. However, this is not an appropriate assumption to make when designing commercial electrolyser. Thus, another factor should be considered is the faradaic efficiency, which is the ratio between experimentally produced gas and theoretically calculated gas in volume. The equation of the faradaic efficiency is:

$$\eta = \frac{V_{H_{2,exp}}}{V_{H_{2,theo}}} \qquad Equation\ 36$$

It was unable to obtain the experimental produced volume of oxygen due to the gas generated by the electrolyser unit was in form of H_2 and O_2 mixture, and gas separation unit was not used. Another performance matrix can be assessed is the energy efficiency, which is the ratio between the energy carried by experimental produced hydrogen and the total electrical energy applied to the electrolyser. The energy efficiency is given by:

$$\eta = \frac{H_{hydrogen} \cdot V_{hydrogen,exp}}{U \cdot I \cdot t} \qquad Equation\ 37$$

Where Hhydrogen is the heat of combustion (calorific value) of hydrogen at 25 °C, kJ/m^3
V is the volume of experimental collected hydrogen
U is the voltage applied to the electrolyser unit
I is the current passed through the electrolyser
t is the time during which voltage was applied

At 25 °C, the calorific value and density of hydrogen are 144,000 kJ/kg and 0.0813 kg/m^3, respectively [97]. Thus, the value of Hhydrogen is 11707.2 kJ/m^3. The energy efficiency calculated by above equation was very low even though assuming 100% faradaic efficiency, because of inappropriate voltage applied to the electrolyser cell during chronoamperometry test (should be at least 2.0V).

It is impossible to achieve 100% efficiency in real world because overpotential would always exist, due to the energy required to overcome ohmic resistance, which by definition means the voltage drop between electrodes. This resistance is not consistent in electrolyser cells and dependent on the individual design of electrolysers. For example, LeRoy et al. concluded that as gas evolved during the electrolyser operation, the volume fraction of gas bubbles between electrode increased, which resulted in increased resistance of the electrolyte [98]. The resistance of electrolyte could also be affected by the electrode gap. If electrodes are too close to each other, the electrolyte resistance could be very large and lower the electrolyser cell efficiency [99]. Furthermore, the electrode morphology would also have huge impact on the cell efficiency because poorly designed electrode could increase the overpotential and ion transport resistance. Some key measures that reflect the morphology can be porosity, electrode surface area, crystalline structure and thickness of catalytic coating etc. It is expected that using high surface area substrates such as foams and meshes could reduce the ion transport resistance compared to flat plate substrates [21].

As the conclusion, the electrode coated with NiFe hydroxide by using the same procedure as Experiment 1 was used as anode in full cell electrolyser testing. The full cell electrolyser contains anode and cathode that were both made of stainless steel 316. The electrodes were separated by PTFE gasket and the membrane was not used, therefore the oxygen and hydrogen produced during water electrolysis came out of the electrolyser as mixture. In the cyclic voltammogram of NiFe hydroxide coated electrode, 2 oxidation peaks were evident which were the oxidation of $Ni(OH)_2$ to NiOOH and OER. Compared to bare stainless steel, the NiFe hydroxide coated anode exhibited significant improved OER due to higher current produced. The cyclic voltammogram of bare electrode also showed the charge transfer, however, the current only increased at moderate rate which indicated slow OER kinetics and therefore the reaction rate. For NiFe hydroxide coated anode, onset OER potential was evident and at 2.0V cell voltage (end point of CV scan), the NiFe hydroxide coated electrode showed much higher current than bare stainless-steel electrode.

The chronoamperometry test of both bare electrode and NiFe hydroxide coated electrode showed small current that was because of low voltage applied. The current generated by NiFe hydroxide electrode was mainly attributed to the oxidation of $Ni(OH)_2$ rather than OER. As a remediation, 2.0V should be applied to the cell and both current and faradaic efficiency would be expected to be higher.

As suggestions to Clean Power Hydrogen Ltd, the NiFe hydroxide electrode can be used as anode in their full-scale electrolyser test with optimum operational condition, e.g. temperature. The bare stainless-steel anode can be used as a good reference to compare the improvement of coated anodes. In addition, the electrode prepared by Experiment 3 can also be considered in full electrolyser test due to positive stability test data.

4. Summary and future work

In summary, all experiments discussed in this thesis have enhanced OER in alkaline solution by different degree. In half cell tests, most of substrates with catalytic coatings except NiFe LDH exhibited much higher current density compared to them without a coating. It expected that with optimised NiFe hydroxide coating, the electrical efficiency of CPH2's electrolyser would be much higher than current achieved efficiency. Based on the results of the half – cell experiments, the lower OER onset potential and overpotential at 10 mA cm^{-2} meant that with the coating, CPH2's electrolyser would consume much less electrical energy to initiate the OER and certain amount of current density than stainless steel substrates themselves. Higher current density at 1.2 V vs SCE indicates that with the coating, the OER kinetic (reaction rate) is higher than that of bare substrates. The stability test results have proven their excellent durability in strong alkaline electrolyte. The summarised data of all experiments 1-4 are presented in the Table 13, in addition, the data of best performing electrocatalysts from literature are also summarised in the same table.

Catalysts	Electrolyte	Substrates	Overpotential at specific current density	Reference
Bare stainless steel	0.1M KOH	/	848 mV @10mA cm^{-2}	/
Exp 1: E1	0.1M KOH	SS316	578 mV @ 10 mA cm^{-2}	Experiment 1
Exp 1: E2	0.1M KOH	SS316	628 mV @ 10 mA cm^{-2}	Experiment 1
Exp 1: E5	0.1M KOH	SS316	518 mV @ 10 mA cm^{-2}	Experiment 1
Exp 2: NiFe 1-1 - 1.3V	0.1MKOH	SS316	671 mV @ 10 mA cm^{-2}	Experiment 2
Exp 2: NiFe 3-1 - 1.3V	0.1M KOH	SS316	741 mV @ 10 mA cm^{-2}	Experiment 2
Exp 2: NiFe 6-1 - 1.3V	0.1M KOH	SS316	681 mV @ 10 mA cm^{-2}	Experiment 2

Exp 2: NiFe 9-1 - 1.3V	0.1M KOH	SS316	757 mV @ 10 mA cm^{-2}	Experiment 2
Exp 3: Pure nickel	0.1M KOH	SS316	668 mV @ 10 mA cm^{-2}	Experiment 3
Exp 3: Fe-$Ni(OH)_2$	0.1M KOH	SS316	628 mA @ 10 mA cm^{-2}	Experiment 3
Exp 4: NiFe 0.5-0.5	0.1M KOH	SS316	648 mV @ 10 mA cm^{-2}	Experiment 4
Exp 4: NiFe 0.7-0.3	0.1M KOH	SS316	678 mV @ 10 mA cm^{-2}	Experiment 4
Exp 4: $Ni(OH)_2$ alone	0.1M KOH	SS316	668 mV @ 10 mA cm^{-2}	Experiment 4
Co/N-CNTs	0.1M KOH	GCE	390 mV @ 10 mA cm^{-2}	[100]
Fe/N-CNTs	0.1M KOH	GCE	520 mV @ 10 mA cm^{-2}	[100]
Ni/N-CNTs	0.1M KOH	GCE	590 mV @ 10 mA cm^{-2}	[100]
CoO_x NPs/BNG	0.1M KOH	GCE	295 mV @ 10 mA cm^{-2}	[101]
Co-Bi/G	0.1M KOH	GCE	320 mV @ 10 mA cm^{-2}	[101]
CoO_x @ CN	1M KOH	Ni foal	260 mV @ 10 mA cm^{-2}	[102]
Co-Fe-O/rGO	1M KOH	GCE	340 mV @ 10 mA cm^{-2}	[103]
$CoFe_2O_4$/rGO	0.1M KOH	GCE	430 mV @ 29.5 mA cm^{-2}	[104]
$Ni_{0.4}Co_{2.6}O_4$	0.1M KOH	Ni foil	520 mV @ 10 mA cm^{-2}	[105]
$Ni_{0.6}Co_{2.4}O_4$	0.1M KOH	Ni foil	530 mV @ 10 mA cm^{-2}	[105]

$Ni_{0.9}Co_{2.6}O_4$	0.1M KOH	Ni foil	530 mV @ 10 mA cm^{-2}	[105]
$NiCo_2O_4$	0.1M KOH	GCE	490 mV @ 10 mA cm^{-2}	[105]
$CuCo_2O_4$/NrGO	0.1M KOH	GCE	410 mV @ 10 mA cm^{-2}	[106]
$MnFe_2O_4$	0.1M KOH	GCE	470 mV @ 10 mA cm^{-2}	[107]
$CoFe_2O_4$	0.1M KOH	GCE	370 mV @ 10 mA cm^{-2}	[107]
$NiFe_2O_4$	0.1M KOH	GCE	440 mV @ 10 mA cm^{-2}	[107]
$CuFe_2O_4$	0.1M KOH	GCE	410 mV @ 10 mA cm^{-2}	[107]
NG	0.1M KOH	GC	700 mV @ 10 mA cm^{-2}	[108]
N-CNT/GNR	0.1M KOH	GC	360 mV @ 10 mA cm^{-2}	[109]
NPMC	0.1M KOH	GCE	395 mV @ 10 mA cm^{-2}	[110]
N-CNTs	0.1M KOH	GCE	390 mV @ 10 mA cm^{-2}	[63]

Table 13. The summarised table of electrochemical performance data reported by Experiments 1-4 and literatures.

The raw materials used, deposition method, advantages and limitations of Experiments 1-4 are all summarised in the Table 14.

Experiment	Raw Materials	Deposition method	Advantages	Limitations
1	$NiSO_4 \cdot 6H_2O$, $FeSO_4 \cdot 7H_2O$, Na_2SO_4	Electrodeposition	Adherent coating; high surface area; decent durability and OER activity; low cost of raw materials and process; the process is quick and straightforward	
2	$Ni(NO_3)_2 \cdot 6H_2O$, $Fe(NO_3)_3 \cdot 9H_2O$, KNO_3	Electrodeposition	Good OER activity; low material and process cost;	Non-adherent coating; relatively poor stability;
3	$NiCl_2 \cdot 6H_2O$, NH_4Cl, NaCl, $FeSO_4 \cdot 7H_2O$	Electrodeposition plus thermal treatment	Good OER activity; good durability	Higher energy requirement; slow process; slightly higher cost;
4	Ni (NO3)2·6H2O, Fe (NO3)3·9H2O, NH4F, urea	Thermal deposition		Poor electrical conductivity; poor OER activity; thick coating;

				hazardous material (NH_4F)

Table 14. Experiment summary include raw materials used, process, advantages and limitations.

Although the outcome of this project has achieved the aims and objectives mentioned in section 1.9, there are still improvement areas to further solidify the chemistry knowledge behind the scene and develop the current coatings. The majority of improvement areas are:

1) Developing current NiFe materials

The electrochemical performance of NiFe materials is affected by many factors, for instance, the methods of coating preparation, temperature, pH, Ni:Fe ratio. Tremendous amount effort is required to find the best coating process and optimal conditions of the process. The current disadvantages have been found for NiFe meterials in this project are poor adherence to substrate surface, and poor electrical conductivity of metal oxides/hydroxides. Poor surface adherence would result in very quick loss of coating materials and catalytic activity. Although annealing at high temperature is helpful in some degree, it would oxidise the metal hydroxides and reduce its electrical conductivity. Many researchers have found that using carbon support and carbon nanotube is an excellent solution to address the issue of poor electrical conductivity, it would however significantly increase the cost, which makes no economic sense for businesses.

2) Research on new materials

Transition metals oxide/hydroxides are currently the most popular OER catalysts in market. The research on new OER anode materials never slows down. The effort has been made not only in the electrochemical performance of the materials, but also in cost reduction and sustainability. For example, the metal free catalysts have attracted huge attention. Some published papers show very exciting opportunities of next – generation OER electrocatalysts such as heteroatom doped CNTs and graphene materials. The background knowledge has not been fully understood yet, however keeping an eye on the newest research results would bring a lot of opportunities for future development.

3) Extending material lifetime

The OER activity decays with time because of the formation of compound that inhibits OER. In this case, it could be chromium oxide. During electrolysis in alkaline condition, the penetration

of KOH accelerate the formation of chromium oxide, which is OER inactive species. The thickness of Cr compound continues building up with time. As the results, less Ni and Fe OER active sites would become available. Although the half-cell stability tests exhibited a good stability over 60 hours, it is not a strong enough evidence that the industrial – scale electrolyser would be as stable as the laboratory scale. One of the solutions is to apply an anti – corrosive coating to OER catalytic coating, which acts as a protective layer which prevents electrolyte from "damaging" the substrates while it allows electrons to flow across. Examples of these conductive layers such as Fluoropolymer, PTFE, and Ceramic Epoxy Coating can be attempted. It would lead to another problems: firstly, the gas removal would be difficult due to the presence of the protective layer. Secondly, an addition coating would also increase the impedance within the electrochemical device. Inappropriate thickness of anti – corrosion layer would significantly reduce the OER.

4) Bubble blinding on the surface of substrates

During both OER and HER, gas bubbles removal has been a big challenge in this project. This subject is out of the scope of the project because it involves the study of fluid dynamics. However, it is worth mentioning that the bubble blinding had big impact on the evaluation of electrochemical properties of the coating materials, especially its stability. The reason of this was that when a reduction of current density was observed, it was difficult to tell whether it was due to the materials degradation or bubble blinding. Ineffective bubble removal would increase the resistance within the electrolyser and consequently the overpotential of the overall electrolysis would increase significantly.

5. References

[1] World Meteorological Organization. (2019). CSIRO: Burning of fossil fuel causes most sea level rise. [online] Available at: https://public.wmo.int/en/media/news/csiro-burning-of-fossil-fuel-causes-most-sea-level-rise [Accessed 25 Apr. 2019].

[2] Ritchie, H. and Roser, M. (2019). Fossil Fuels. [online] Our World in Data. Available at: https://ourworldindata.org/fossil-fuels [Accessed 25 May 2019].

[3] Denchak, M. (2019). Fossil Fuels: The Dirty Facts. [online] NRDC. Available at: https://www.nrdc.org/stories/fossil-fuels-dirty-facts [Accessed 18 Mar. 2019].

[4] GOV.UK. (2019). Fossil fuel price assumptions. [online] Available at: https://www.gov.uk/government/collections/fossil-fuel-price-assumptions [Accessed 9 Mar. 2019].

[5] Department for Business, Energy & Industrial Strategy (2019). 2018 UK greenhouse gas emissions, provisional figures. London.

[6] Ogden, J. (2002). Hydrogen: The Fuel of the Future?. Physics Today, 55(4), pp.69-75.

[7] New Energy Treasure - The Coming Energy Revolution. (2019). Hydrogen Production In The Coming Hydrogen Economy. [online] Available at: https://newenergytreasure.com/2014/06/28/hydrogen-production-in-the-new-hydrogen-economy/ [Accessed 14 Jun. 2019].

[8] Kayfeci, M., Keçebaş, A. and Bayat, M. (2019). Hydrogen production. Solar Hydrogen Production, pp.45-83.

[9] Royalsociety.org. (2019). Methods of Producing Hydrogen at Scale | Royal Society. [online] Available at: https://royalsociety.org/topics-policy/projects/low-carbon-energy-programme/hydrogen-production/?gclid=Cj0KCQjwrfvsBRD7ARIsAKuDvMPmA_HupzljI7Q9-IJB2XuX_qThTm1fCDP3ZvoAYnii8IBm3HF83NYaAvqqEALw_wcB [Accessed 28 Aug. 2019].

[10] Www1.eere.energy.gov. (2019). Hydrogen Production: Overview of Technology Options. [online] Available at: https://www1.eere.energy.gov/hydrogenandfuelcells/pdfs/h2_tech_roadmap.pdf [Accessed 11 Feb. 2019].

[11] Goodall, C. and Goodall, C. (2020). Hydrogen made by the electrolysis of water is now cost-competitive and gives us another building block for the low-carbon economy | Carbon Commentary. [online] Carbon Commentary. Available at: https://www.carboncommentary.com/blog/2017/7/5/hydrogen-made-by-the-electrolysis-of-water-is-now-cost-competitive-and-gives-us-another-building-block-for-the-low-carbon-economy [Accessed 4 Jan. 2020].

[12] Nel Hydrogen. (2019). Hydrogen Production • Nel Hydrogen. [online] Available at: https://nelhydrogen.com/market/hydrogen-production/#related-products [Accessed 14 May 2019].

[13] Shiva Kumar, S. and Himabindu, v., 2019. Hydrogen production by PEM water electrolysis – A review. Materials Science for Energy Technologies, [online] 2(3). Available at: <https://www.sciencedirect.com/science/article/pii/S2589299119300035> [Accessed 19 February 2021].

[14] Xu, W. and Scott, K., 2010. The effects of ionomer content on PEM water electrolyser membrane electrode assembly performance. International Journal of Hydrogen Energy, [online] 35(21), pp.12029-12037. Available at: <https://www.sciencedirect.com/science/article/pii/S0360319910016940> [Accessed 3 January 2021].

[15] Mocoteguy, P. and Brisse, A., 2014. ChemInform Abstract: A Review and Comprehensive Analysis of Degradation Mechanisms of Solid Oxide Electrolysis Cells. ChemInform, [online] 45(6), p.no-no. Available at: <https://www.sciencedirect.com/science/article/pii/S0360319913022684> [Accessed 11 February 2021].

[16] Laguna-Bercero, M., 2012. Recent advances in high temperature electrolysis using solid oxide fuel cells: A review. Journal of Power Sources, [online] 203, pp.4-16. Available at: <https://www.sciencedirect.com/science/article/pii/S0378775311024384> [Accessed 7 February 2021].

[17] Options for producing low-carbon hydrogen at scale. (2019). The Royal Society. [online] Available at: http://creativecommons.org/licenses/by/4.0 [Accessed 16 Jan. 2019].

[18] Santos, D., Sequeira, C. and Figueiredo, J. (2013). Hydrogen production by alkaline water electrolysis. Química Nova, [online] 36(8), pp.1176-1193. Available at: http://www.scielo.br/scielo.php?script=sci_arttext&pid=S0100-40422013000800017 [Accessed 10 Jun. 2019].

[19] Naimi, Y. and Antar, A., 2018. Hydrogen Generation by Water Electrolysis. Advances In Hydrogen Generation Technologies, [online] Available at: <https://www.intechopen.com/books/advances-in-hydrogen-generation-technologies/hydrogen-generation-by-water-electrolysis> [Accessed 23 March 2021].

[20] Chemistry LibreTexts. 2018. 6.2: Standard Electrode Potentials. [online] Available at: <https://chem.libretexts.org/Courses/Mount_Royal_University/Chem_1202/Unit_6%3A_Electrochemistry/6.2%3A_Standard_Electrode_Potentials> [Accessed 23 March 2021].

[21] Phillips, R., Edwards, A., Rome, B., Jones, D. and Dunnill, C., 2017. Minimising the ohmic resistance of an alkaline electrolysis cell through effective cell design. International Journal of Hydrogen Energy, [online] 42(38), pp.23986-23994. Available at:

<https://www.sciencedirect.com/science/article/pii/S0360319917330203#bib14> [Accessed 21 January 2021].

[22] de Souza, R., Padilha, J., Gonçalves, R., de Souza, M. and Rault-Berthelot, J., 2007. Electrochemical hydrogen production from water electrolysis using ionic liquid as electrolytes: Towards the best device. Journal of Power Sources, [online] 164(2), pp.792-798. Available at: <https://www.researchgate.net/publication/223450680_Electrochemical_hydrogen_production_from_water_electrolysis_using_ionic_liquid_as_electrolytes_Towards_the_best_device> [Accessed 11 November 2020].

[23] Zeng, K. and Zhang, D., 2010. Recent progress in alkaline water electrolysis for hydrogen production and applications. Progress in Energy and Combustion Science, [online] 36(3), pp.307-326. Available at: <https://www.sciencedirect.com/science/article/pii/S0360128509000598> [Accessed 5 November 2020].

[24] JANJUA, M. and LEROY, R., 1985. Electrocatalyst performance in industrial water electrolysers. International Journal of Hydrogen Energy, [online] 10(1), pp.11-19. Available at: <https://www.sciencedirect.com/science/article/abs/pii/0360319985901302> [Accessed 12 December 2020].

[25] Stojić, D., Marčeta, M., Sovilj, S. and Miljanić, Š., 2003. Hydrogen generation from water electrolysis—possibilities of energy saving. Journal of Power Sources, [online] 118(1-2), pp.315-319. Available at: <https://ui.adsabs.harvard.edu/abs/2003JPS...118..315S/abstract> [Accessed 2 January 2021].

[26] Mpie.de. (2019). Oxygen Evolution Reaction. [online] Available at: https://www.mpie.de/3146541/Water_Electrolysis [Accessed 15 Jan. 2019].

[27] Kim, J., Kim, B., Kim, H. and Kang, K. (2018). Recent Progress on Multimetal Oxide Catalysts for the Oxygen Evolution Reaction. Advanced Energy Materials, [online] 8(11), p.1702774. Available at: https://onlinelibrary.wiley.com/doi/full/10.1002/aenm.201702774 [Accessed 27 Nov. 2018].

[28] Hu, C., Zhang, L. and Gong, J. (2019). Recent progress made in the mechanism comprehension and design of electrocatalysts for alkaline water splitting. Energy & Environmental Science, [online] 12(9), pp.2620-2645. Available at: https://pubs.rsc.org/en/content/articlelanding/2019/ee/c9ee01202h#!divAbstract [Accessed 15 Aug. 2019].

[29] Dau, H., Limberg, C., Reier, T., Risch, M., Roggan, S. and Strasser, P., 2010. ChemInform Abstract: The Mechanism of Water Oxidation: From Electrolysis via Homogeneous to Biological Catalysis. ChemInform, [online] 41(38). Available at: <https://chemistry-europe.onlinelibrary.wiley.com/doi/abs/10.1002/cctc.201000126> [Accessed 15 January 2021].

[30] Man, I., Su, H., Calle-Vallejo, F., Hansen, H., Martínez, J., Inoglu, N., Kitchin, J., Jaramillo, T., Nørskov, J. and Rossmeisl, J. (2011). Cover Picture: Universality in Oxygen Evolution Electrocatalysis on Oxide Surfaces (ChemCatChem 7/2011). ChemCatChem, [online] 3(7), pp.1085-1085. Available at: https://onlinelibrary.wiley.com/doi/10.1002/cctc.201000397 [Accessed 11 Feb. 2019].

[31] Fabbri, E., Habereder, A., Waltar, K., Kötz, R. and Schmidt, T. (2014). Developments and perspectives of oxide-based catalysts for the oxygen evolution reaction. Catal. Sci. Technol., [online] 4(11), pp.3800-3821. Available at: https://pubs.rsc.org/en/content/articlehtml/2014/cy/c4cy00669k [Accessed 26 Nov. 2018].

[32] Suen, N., Hung, S., Quan, Q., Zhang, N., Xu, Y. and Chen, H. (2017). Electrocatalysis for the oxygen evolution reaction: recent development and future perspectives. Chemical Society Reviews, [online] 46(2), pp.337-365. Available at: https://pubs.rsc.org/en/content/articlelanding/2017/cs/c6cs00328a#!divAbstract [Accessed 18 Feb. 2019].

[33] Zayat, B., Mitra, D. and Narayanan, S., 2020. Inexpensive and Efficient Alkaline Water Electrolyzer with Robust Steel-Based Electrodes. Journal of The Electrochemical Society, [online] 167(11), p.114513. Available at: <https://iopscience.iop.org/article/10.1149/1945-7111/aba792> [Accessed 2 January 2021].

[34] McCrory, C., Jung, S., Peters, J. and Jaramillo, T., 2013. Benchmarking Heterogeneous Electrocatalysts for the Oxygen Evolution Reaction. Journal of the American Chemical Society, [online] 135(45), pp.16977-16987. Available at: <https://pubs.acs.org/doi/full/10.1021/ja407115p> [Accessed 6 February 2021].

[35] Oakton, E., Lebedev, D., Povia, M., Abbott, D., Fabbri, E., Fedorov, A., Nachtegaal, M., Copéret, C. and Schmidt, T., 2017. IrO2-TiO2: A High-Surface-Area, Active, and Stable Electrocatalyst for the Oxygen Evolution Reaction. ACS Catalysis, [online] 7(4), pp.2346-2352. Available at: <https://pubs.acs.org/doi/10.1021/acscatal.6b03246> [Accessed 5 February 2021].

[36] Wang, Y., Yu, J., Wang, Y., Chen, Z., Dong, L., Cai, R., Hong, M., Long, X. and Yang, S., 2020. In situ templating synthesis of mesoporous Ni–Fe electrocatalyst for oxygen evolution reaction. RSC Advances, [online] 10(39), pp.23321-23330. Available at: <https://pubs.rsc.org/en/content/articlehtml/2020/ra/d0ra03111a> [Accessed 3 February 2021].

[37] CORRIGAN, D. (1987). ChemInform Abstract: Catalysis of the Oxygen Evolution Reaction by Iron Impurities in Thin Film Nickel Oxide Electrodes. ChemInform, [online] 18(22). Available at: http://jes.ecsdl.org/content/134/2/377.full.pdf+html [Accessed 13 Feb. 2019].

[38] David, M., Ocampo-Martínez, C. and Sánchez-Peña, R., 2019. Advances in alkaline water electrolyzers: A review. Journal of Energy Storage, [online] 23, pp.392-403. Available at: <https://core.ac.uk/download/pdf/288624715.pdf> [Accessed 4 January 2021].

[39] Yi, J., Lee, W., Choi, C., Lee, Y., Park, K., Min, B., Hwang, Y. and Oh, H. (2019). Effect of Pt introduced on Ru-based electrocatalyst for oxygen evolution activity and stability. Electrochemistry Communications, [online] 104, p.106469. Available at: https://www.sciencedirect.com/science/article/pii/S1388248119301262 [Accessed 9 Aug. 2019].

[40] Reier, T., Oezaslan, M. and Strasser, P. (2012). Electrocatalytic Oxygen Evolution Reaction (OER) on Ru, Ir, and Pt Catalysts: A Comparative Study of Nanoparticles and Bulk Materials. ACS Catalysis, [online] 2(8), pp.1765-1772. Available at: https://pubs.acs.org/doi/10.1021/cs3003098 [Accessed 8 Nov. 2018].

[41] Tahir, M., Pan, L., Idrees, F., Zhang, X., Wang, L., Zou, J. and Wang, Z. (2017). Electrocatalytic oxygen evolution reaction for energy conversion and storage: A comprehensive review. Nano Energy, [online] 37, pp.136-157. Available at: https://www.sciencedirect.com/science/article/pii/S221128551730294X [Accessed 8 Dec. 2018].

[42] Trasatti, S. (1980). Electrocatalysis by oxides — attempt at a unifying approach. Journal of Electroanalytical Chemistry, [online] 111(1), pp.125-131. Available at: https://www.sciencedirect.com/science/article/pii/S0022072880800842 [Accessed 10 Dec. 2018].

[43] Lee, Y., Suntivich, J., May, K., Perry, E. and Shao-Horn, Y. (2012). Synthesis and Activities of Rutile IrO2 and RuO2 Nanoparticles for Oxygen Evolution in Acid and Alkaline Solutions. The Journal of Physical Chemistry Letters, [online] 3(3), pp.399-404. Available at: https://pubs.acs.org/doi/10.1021/jz2016507 [Accessed 9 Dec. 2018].

[44] Cherevko, S., Geiger, S., Kasian, O., Kulyk, N., Grote, J., Savan, A., Shrestha, B., Merzlikin, S., Breitbach, B., Ludwig, A. and Mayrhofer, K. (2016). Oxygen and hydrogen evolution reactions on Ru, RuO 2 , Ir, and IrO 2 thin film electrodes in acidic and alkaline electrolytes: A comparative study on activity and stability. Catalysis Today, [online] 262, pp.170-180. Available at: https://www.sciencedirect.com/science/article/abs/pii/S0920586115004940 [Accessed 10 Dec. 2018].

[45] Wang, Y., Zhou, T., Jiang, K., Da, P., Peng, Z., Tang, J., Kong, B., Cai, W., Yang, Z. and Zheng, G. (2014). Electrocatalysis: Reduced Mesoporous Co3O4Nanowires as Efficient Water Oxidation Electrocatalysts and Supercapacitor Electrodes (Adv. Energy Mater. 16/2014). Advanced Energy Materials, [online] 4(16), p.n/a-n/a. Available at: https://onlinelibrary.wiley.com/doi/full/10.1002/aenm.201400696 [Accessed 8 Nov. 2018].

[46] Xu, L., Jiang, Q., Xiao, Z., Li, X., Huo, J., Wang, S. and Dai, L. (2016). Plasma-Engraved Co3O4 Nanosheets with Oxygen Vacancies and High Surface Area for the Oxygen Evolution Reaction. Angewandte Chemie, [online] 128(17), pp.5363-5367. Available at: https://onlinelibrary.wiley.com/doi/full/10.1002/anie.201600687 [Accessed 9 Nov. 2018].

[47] Wang, H., Hung, S., Chen, H., Chan, T., Chen, H. and Liu, B. (2015). In Operando Identification of Geometrical-Site-Dependent Water Oxidation Activity of Spinel Co3O4. Journal

of the American Chemical Society, [online] 138(1), pp.36-39. Available at: https://pubs.acs.org/doi/10.1021/jacs.5b10525 [Accessed 9 Nov. 2018].

[48] Greenwood, N. and Earnshaw, A. (2016). Chemistry of the elements. 2nd ed. Amsterdam [etc.]: Elsevier Butterworth-Heinemann, p.1118.

[49] Chen, Y., Rui, K., Zhu, J., Dou, S. and Sun, W. (2018). Recent Progress on Nickel-Based Oxide/(Oxy)Hydroxide Electrocatalysts for the Oxygen Evolution Reaction. Chemistry – A European Journal, [online] 25(3), pp.703-713. Available at: https://onlinelibrary.wiley.com/doi/10.1002/chem.201802068 [Accessed 12 Nov. 2018].

[50] Juodkazis, K., Juodkazytė, J., Vilkauskaitė, R. and Jasulaitienė, V. (2008). Nickel surface anodic oxidation and electrocatalysis of oxygen evolution. Journal of Solid State Electrochemistry, [online] 12(11), pp.1469-1479. Available at: https://link.springer.com/article/10.1007%2Fs10008-007-0484-0 [Accessed 12 Nov. 2018].

[51] Fayad, R., Dhainy, J., Ghandour, H. and Halaoui, L. (2017). Electrochemical study of the promoting effect of Fe on oxygen evolution at thin 'NiFe–Bi' films and the inhibiting effect of Al in borate electrolyte. Catalysis Science & Technology, [online] 7(17), pp.3876-3891. Available at: https://pubs.rsc.org/en/content/articlelanding/2017/cy/c7cy00873b#!divAbstract [Accessed 11 Nov. 2018].

[52] Fominykh, K., Feckl, J., Sicklinger, J., Döblinger, M., Böcklein, S., Ziegler, J., Peter, L., Rathousky, J., Scheidt, E., Bein, T. and Fattakhova-Rohlfing, D. (2014). Water Splitting: Ultrasmall Dispersible Crystalline Nickel Oxide Nanoparticles as High-Performance Catalysts for Electrochemical Water Splitting (Adv. Funct. Mater. 21/2014). Advanced Functional Materials, [online] 24(21), pp.3105-3105. Available at: https://onlinelibrary.wiley.com/doi/full/10.1002/adfm.201303600 [Accessed 16 Nov. 2018].

[53] Bergmann, A., Zaharieva, I., Dau, H. and Strasser, P. (2013). Electrochemical water splitting by layered and 3D cross-linked manganese oxides: correlating structural motifs and catalytic activity. Energy & Environmental Science, [online] 6(9), p.2745. Available at: https://pubs.rsc.org/en/content/articlelanding/2013/EE/c3ee41194j#!divAbstract [Accessed 20 Nov. 2018].

[54] Lian, S., Browne, M., Domínguez, C., Stamatin, S., Nolan, H., Duesberg, G., Lyons, M., Fonda, E. and Colavita, P. (2017). Template-free synthesis of mesoporous manganese oxides with catalytic activity in the oxygen evolution reaction. Sustainable Energy & Fuels, [online] 1(4), pp.780-788. Available at: https://pubs.rsc.org/en/content/articlelanding/2017/se/c7se00086c#!divAbstract [Accessed 21 Nov. 2018].

[55] Huynh, M., Shi, C., Billinge, S. and Nocera, D. (2015). Nature of Activated Manganese Oxide for Oxygen Evolution. Journal of the American Chemical Society, [online] 137(47), pp.14887-14904. Available at: https://pubs.acs.org/doi/10.1021/jacs.5b06382 [Accessed 22 Nov. 2018].

[56] Cdti.com. (2019). CDTi Advanced Materials, Inc.. [online] Available at: http://www.cdti.com/spinel/ [Accessed 25 Nov. 2018].

[57] Li, Y., Hasin, P. and Wu, Y. (2010). NixCo3−xO4 Nanowire Arrays for Electrocatalytic Oxygen Evolution. Advanced Materials, [online] 22(17), pp.1926-1929. Available at: https://onlinelibrary.wiley.com/doi/full/10.1002/adma.200903896 [Accessed 29 Nov. 2018].

[58] Jin, C., Lu, F., Cao, X., Yang, Z. and Yang, R. (2013). Facile synthesis and excellent electrochemical properties of NiCo2O4 spinel nanowire arrays as a bifunctional catalyst for the oxygen reduction and evolution reaction. Journal of Materials Chemistry A, [online] 1(39), p.12170. Available at: https://pubs.rsc.org/en/content/articlelanding/2013/TA/c3ta12118f#!divAbstract [Accessed 29 Nov. 2018].

[59] Chen, R., Wang, H., Miao, J., Yang, H. and Liu, B. (2015). A flexible high-performance oxygen evolution electrode with three-dimensional NiCo2O4 core-shell nanowires. Nano Energy, [online] 11, pp.333-340. Available at: https://www.sciencedirect.com/science/article/pii/S2211285514201340 [Accessed 29 Nov. 2018].

[60] Cui, B., Lin, H., Li, J., Li, X., Yang, J. and Tao, J. (2008). Core-Ring Structured NiCo2O4 Nanoplatelets: Synthesis, Characterization, and Electrocatalytic Applications. Advanced Functional Materials, [online] 18(9), pp.1440-1447. Available at: https://onlinelibrary-wiley-com.ezproxy.lancs.ac.uk/doi/epdf/10.1002/adfm.200700982 [Accessed 30 Nov. 2018].

[61] Shi, H. and Zhao, G. (2014). Water Oxidation on Spinel NiCo2O4 Nanoneedles Anode: Microstructures, Specific Surface Character, and the Enhanced Electrocatalytic Performance. The Journal of Physical Chemistry C, [online] 118(45), pp.25939-25946. Available at: https://pubs.acs.org/doi/pdf/10.1021/jp508977j [Accessed 30 Nov. 2018].

[62] Tan, Y., Wu, C., Lin, H., Li, J., Chi, B., Pu, J. and Jian, L. (2014). Insight the effect of surface Co cations on the electrocatalytic oxygen evolution properties of cobaltite spinels. Electrochimica Acta, [online] 121, pp.183-187. Available at: https://www.sciencedirect.com/science/article/pii/S0013468613025814 [Accessed 30 Nov. 2018].

[63] Cheng, Y. and Jiang, S. (2015). Advances in electrocatalysts for oxygen evolution reaction of water electrolysis-from metal oxides to carbon nanotubes. Progress in Natural Science: Materials International, [online] 25(6), pp.545-553. Available at: https://www.sciencedirect.com/science/article/pii/S1002007115001264 [Accessed 30 Nov. 2018].

[64] Phys.org. (2019). Revealing the ligand-hole localization behaviors in oxides with unusual high-valence Fe. [online] Available at: https://phys.org/news/2012-06-revealing-ligand-hole-localization-behaviors-oxides.html [Accessed 30 Nov. 2018].

[65] Sapountzi, F., Gracia, J., Weststrate, C., Fredriksson, H. and Niemantsverdriet, J. (2017). Electrocatalysts for the generation of hydrogen, oxygen and synthesis gas. Progress in Energy and Combustion Science, [online] 58, pp.1-35. Available at: https://www.sciencedirect.com/science/article/pii/S0360128516300260 [Accessed 30 Nov. 2018].

[66] Mishra, G., Dash, B. and Pandey, S. (2018). Layered double hydroxides: A brief review from fundamentals to application as evolving biomaterials. Applied Clay Science, [online] 153, pp.172-186. Available at: https://www.sciencedirect.com/science/article/pii/S0169131717305707 [Accessed 30 Nov. 2018].

[67] Song, F. and Hu, X. (2014). Exfoliation of layered double hydroxides for enhanced oxygen evolution catalysis. Nature Communications, [online] 5(1). Available at: https://www.nature.com/articles/ncomms5477?origin=ppub [Accessed 30 Nov. 2018].

[68] Badruzzaman, A., Yuda, A., Ashok, A. and Kumar, A., 2020. Recent advances in cobalt based heterogeneous catalysts for oxygen evolution reaction. Inorganica Chimica Acta, [online] 511, p.119854. Available at: <https://www.sciencedirect.com/science/article/pii/S0020169320310537> [Accessed 9 March 2021].

[69] Tichenor, R., 1952. Nickel Oxides-Relation Between Electrochemical and Foreign Ion Content. Industrial & Engineering Chemistry, [online] 44(5), pp.973-977. Available at: <https://pubs.acs.org/doi/pdf/10.1021/ie50509a022> [Accessed 4 February 2021].

[70] Louie, M. and Bell, A., 2013. An Investigation of Thin-Film Ni–Fe Oxide Catalysts for the Electrochemical Evolution of Oxygen. Journal of the American Chemical Society, [online] 135(33), pp.12329-12337. Available at: <https://pubs.acs.org/doi/full/10.1021/ja405351s> [Accessed 5 February 2021].

[71] Wei, W., He, W., Shi, B., Dong, G., Lu, X., Zeng, M., Gao, X., Wang, Q., Zhou, G., Liu, J., Herczynski, A., Kempa, K. and Gao, J. (2019). A bio-inspired 3D quasi-fractal nanostructure for an improved oxygen evolution reaction. Chemical Communications, [online] 55(3), pp.357-360. Available at: https://pubs.rsc.org/en/content/articlelanding/2019/cc/c8cc08221a#!divAbstract [Accessed 18 May 2019].

[72] Spanos, I., Masa, J., Zeradjanin, A. and Schlögl, R., 2020. The Effect of Iron Impurities on Transition Metal Catalysts for the Oxygen Evolution Reaction in Alkaline Environment: Activity Mediators or Active Sites?. Catalysis Letters, [online] Available at: <https://link.springer.com/article/10.1007/s10562-020-03478-4> [Accessed 7 January 2021].

[73] Atkins, P. and De Paula, J. (2010). Physical chemistry. 6th ed. Oxford: Freeman.

[74] Kim, K., Zheng, J., Shin, W. and Kang, Y. (2012). Preparation of dendritic NiFe films by electrodeposition for oxygen evolution. RSC Advances, [online] 2(11), p.4759. Available at:

https://pubs.rsc.org/en/content/articlelanding/2012/ra/c2ra20241g#!divAbstract [Accessed 9 Mar. 2019].

[75] Saraby-Reintjes, A. and Fleischmann, M., 1984. Kinetics of electrodeposition of nickel from watts baths. Electrochimica Acta, [online] 29(4), pp.557-566. Available at: <https://www.sciencedirect.com/science/article/abs/pii/0013468684871091> [Accessed 8 November 2020].

[76] Oriňáková, R., Turoňová, A., Kladeková, D., Gálová, M. and Smith, R., 2006. Recent developments in the electrodeposition of nickel and some nickel-based alloys. Journal of Applied Electrochemistry, [online] 36(9), pp.957-972. Available at: <https://link.springer.com/article/10.1007/s10800-006-9162-7> [Accessed 17 October 2020].

[77] Su, C., He, F., Ju, H., Zhang, Y. and Wang, E., 2009. Electrodeposition of Ni, Fe and Ni–Fe alloys on a 316 stainless steel surface in a fluorborate bath. Electrochimica Acta, [online] 54(26), pp.6257-6263. Available at: <https://www.sciencedirect.com/science/article/pii/S0013468609007713> [Accessed 11 December 2020].

[78] Miranda-Hernández, M. and González, I., 2004. Effect of Potential on the Early Stages of Nucleation and Growth during Silver Electrocrystallization in Ammonium Medium on Vitreous Carbon. Journal of The Electrochemical Society, [online] 151(3), p.C220. Available at: <https://www.researchgate.net/publication/234932680_Effect_of_Potential_on_the_Early_Stages_of_Nucleation_and_Growth_during_Silver_Electrocrystallization_in_Ammonium_Medium_on_Vitreous_Carbon> [Accessed 21 November 2020].

[79] Chassaing, E., 1983. The kinetics of nickel electrodeposition inhibition by absorbed hydrogen and anions. Journal of Electroanalytical Chemistry, [online] 157(1), pp.75-88. Available at: <https://www.sciencedirect.com/science/article/abs/pii/S0022072883803775> [Accessed 21 November 2020].

[80] Moharana, M. and Mallik, A., 2013. Nickel electrocrystallization in different electrolytes: An in-process and post synthesis analysis. Electrochimica Acta, [online] 98, pp.1-10. Available at: <https://www.sciencedirect.com/science/article/pii/S0013468613004283> [Accessed 10 December 2020].

[81] Lantelme, F., Seghiouer, A. and Derja, A., 1998. Model of nickel electrodeposition from acidic medium. Journal of Applied Electrochemistry, [online] 28(907–913(1998). Available at: <https://link.springer.com/article/10.1023%2FA%3A1003404118601> [Accessed 19 January 2021].

[82] Holm, M. and O'Keefe, T., 2000. Evaluation of nickel deposition by electrochemical impedance spectroscopy. Journal of Applied Electrochemistry, [online] 30(1125–1132). Available at: <https://link.springer.com/article/10.1023/A:1004002303181> [Accessed 24 January 2021].

[83] Li, Y. and Selloni, A., 2014. Mechanism and Activity of Water Oxidation on Selected Surfaces of Pure and Fe-Doped NiOx. ACS Catalysis, [online] 4(4), pp.1148-1153. Available at: <https://pubs.acs.org/doi/pdf/10.1021/cs401245q> [Accessed 3 December 2020].

[84] Lyons, M. and Brandon, M., 2008. HomeWater SplittingCatalysisChemistryOxygen Evolution Reaction ArticlePDF Available The Oxygen Evolution Reaction on Passive Oxide Covered Transition Metal Electrodes in Aqueous Alkaline Solution. Part 1-Nickel. International Journal of Electrochemical Science, [online] 3(1386-1424). Available at: <https://www.researchgate.net/publication/228357069_The_Oxygen_Evolution_Reaction_on_Passive_Oxide_Covered_Transition_Metal_Electrodes_in_Aqueous_Alkaline_Solution_Part_1-Nickel> [Accessed 16 January 2021].

[85] Lyons, M. and Brandon, M., 2010. A comparative study of the oxygen evolution reaction on oxidised nickel, cobalt and iron electrodes in base. Journal of Electroanalytical Chemistry, [online] 641(1-2), pp.119-130. Available at: <http://www.tara.tcd.ie/xmlui/bitstream/handle/2262/41125/JEAC6.pdf;jsessionid=FD72AA84B78C7A13900B463F3CD55CB7?sequence=1> [Accessed 5 November 2020].

[86] Bediako, D., Lassalle-Kaiser, B., Surendranath, Y., Yano, J., Yachandra, V. and Nocera, D., 2012. Structure–Activity Correlations in a Nickel–Borate Oxygen Evolution Catalyst. Journal of the American Chemical Society, [online] 134(15), pp.6801-6809. Available at: <https://pubmed.ncbi.nlm.nih.gov/22417283/> [Accessed 30 November 2020].

[87] Nakano, H., Matsuno, M., Oue, S., Yano, M., Kobayashi, S. and Fukushima, H., 2004. Mechanism of Anomalous Type Electrodeposition of Fe-Ni Alloys from Sulfate Solutions. MATERIALS TRANSACTIONS, [online] 45(11), pp.3130-3135. Available at: <https://www.jim.or.jp/journal/e/pdf3/45/11/3130.pdf> [Accessed 4 November 2020].

[88] Frey, A., Wozniak, N., Nagi, T., Keller, M., Lunderberg, J., Peaslee, G., DeYoung, P. and Hampton, J., 2011. Analysis of Electrodeposited Nickel-Iron Alloy Film Composition Using Particle-Induced X-Ray Emission. International Journal of Electrochemistry, [online] 2011, pp.1-7. Available at: <https://www.hindawi.com/journals/ijelc/2011/604395/> [Accessed 5 January 2021].

[89] Wei, G., Fang, Y. and Liu, Z., 2012. First Principles Tafel Kinetics for Resolving Key Parameters in Optimizing Oxygen Electrocatalytic Reduction Catalyst. The Journal of Physical Chemistry C, 116(23), pp.12696-12705.

[90] Devadas, A., Baranton, S. and Coutanceau, C., 2020. Green Synthesis and Modification of RuO2 Materials for the Oxygen Evolution Reaction. Frontiers in Energy Research, [online] 8. Available at: <https://www.frontiersin.org/articles/10.3389/fenrg.2020.571704/full> [Accessed 8 February 2021].

[91] Damjanovic, A., Dey, A. and Bockris, J., 1966. Kinetics of oxygen evolution and dissolution on platinum electrodes. Electrochimica Acta, [online] 11(7), pp.791-814. Available at: <https://www.sciencedirect.com/science/article/abs/pii/0013468666870561?via%

[92] Kapałka, A., Fóti, G. and Comninellis, C., 2008. Determination of the Tafel slope for oxygen evolution on boron-doped diamond electrodes. Electrochemistry Communications, 10(4), pp.607-610.

[93] Lu, X. and Zhao, C. (2015). Electrodeposition of hierarchically structured three-dimensional nickel–iron electrodes for efficient oxygen evolution at high current densities. Nature Communications, [online] 6(1). Available at: https://www.nature.com/articles/ncomms7616#Sec2 [Accessed 17 Apr. 2019].

[94] Jayashree, R. and Kamath, P., 2001. Nickel hydroxide electrodeposition from nickel nitrate solutions: mechanistic studies. Journal of Power Sources, [online] 93(1-2), pp.273-278. Available at: <https://core.ac.uk/download/pdf/72796969.pdf> [Accessed 30 December 2020].

[95] Gong, M., Li, Y., Wang, H., Liang, Y., Wu, J., Zhou, J., Wang, J., Regier, T., Wei, F. and Dai, H., 2013. An Advanced Ni–Fe Layered Double Hydroxide Electrocatalyst for Water Oxidation. Journal of the American Chemical Society, [online] 135(23), pp.8452-8455. Available at: <https://pubs.acs.org/doi/10.1021/ja4027715> [Accessed 11 November 2020].

[96] Manabe, A., Kashiwase, M., Hashimoto, T., Hayashida, T., Kato, A., Hirao, K., Shimomura, I. and Nagashima, I., 2013. Basic study of alkaline water electrolysis. Electrochimica Acta, [online] 100, pp.249-256. Available at: <https://www.sciencedirect.com/science/article/pii/S0013468612020798> [Accessed 14 December 2020].

[97] Engineeringtoolbox.com. 2021. Hydrogen - Density and Specific Weight. [online] Available at: <https://www.engineeringtoolbox.com/hydrogen-H2-density-specific-weight-temperature-pressure-d_2044.html> [Accessed 23 March 2021].

[98] LeRoy, R., Janjua, M., Renaud, R. and Leuenberger, U., 1979. Analysis of Time-Variation Effects in Water Electrolyzers. Journal of The Electrochemical Society, [online] 126(10), pp.1674-1682. Available at: <https://iopscience.iop.org/article/10.1149/1.2128775/pdf> [Accessed 10 February 2021].

[99] Nagai, N., 2003. Existence of optimum space between electrodes on hydrogen production by water electrolysis. International Journal of Hydrogen Energy, [online] 28(1), pp.35-41. Available at: <https://www.sciencedirect.com/science/article/pii/S0360319902000277> [Accessed 2 January 2021].

[100] Liu, Y., Jiang, H., Zhu, Y., Yang, X. and Li, C., 2016. Transition metals (Fe, Co, and Ni) encapsulated in nitrogen-doped carbon nanotubes as bi-functional catalysts for oxygen electrode reactions. Journal of Materials Chemistry A, [online] 4(5), pp.1694-1701. Available at: <https://pubs.rsc.org/en/content/articlelanding/2016/ta/c5ta10551j#!divAbstract> [Accessed 12 March 2021].

[101] Tong, Y., Chen, P., Zhou, T., Xu, K., Chu, W., Wu, C. and Xie, Y., 2017. A Bifunctional Hybrid Electrocatalyst for Oxygen Reduction and Evolution: Cobalt Oxide Nanoparticles Strongly Coupled to B,N-Decorated Graphene. Angewandte Chemie, [online] 129(25), pp.7227-7231.

Available at:
<https://www.researchgate.net/publication/317033788_A_Bifunctional_Hybrid_Electrocatalyst_for_Oxygen_Reduction_and_Evolution_Cobalt_Oxide_Nanoparticles_Strongly_Coupled_to_BN-Decorated_Graphene> [Accessed 12 March 2021].

[102] Singh, S., Takeyasu, K., Paul, B., Sharma, S. and Nakamura, J., 2021. CoOx electro-catalysts anchored on nitrogen-doped carbon nanotubes for the oxygen evolution reaction. Sustainable Energy & Fuels, [online] 5(3), pp.820-827. Available at:
<https://pubs.rsc.org/en/content/articlelanding/2021/se/d0se01285h#!divAbstract> [Accessed 12 March 2021].

[103] Geng, J., Kuai, L., Kan, E., Wang, Q. and Geng, B., 2015. Precious-Metal-Free Co-Fe-O/rGO Synergetic Electrocatalysts for Oxygen Evolution Reaction by a Facile Hydrothermal Route. ChemSusChem, [online] 8(4), pp.659-664. Available at: <https://chemistry-europe.onlinelibrary.wiley.com/doi/10.1002/cssc.201403222> [Accessed 12 March 2021].

[104] Bian, W., Yang, Z., Strasser, P. and Yang, R., 2014. A CoFe2O4/graphene nanohybrid as an efficient bi-functional electrocatalyst for oxygen reduction and oxygen evolution. Journal of Power Sources, [online] 250, pp.196-203. Available at:
<https://www.sciencedirect.com/science/article/pii/S0378775313018508> [Accessed 12 March 2021].

[105] De Chialvo, M. and Chialvo, A., 1993. Oxygen evolution reaction on NixCo(3—xO4 electrodes with spinel structure. Electrochimica Acta, [online] 38(15), pp.2247-2252. Available at: <https://www.sciencedirect.com/science/article/abs/pii/0013468693801059> [Accessed 12 March 2021].

[106] Bikkarolla, S. and Papakonstantinou, P., 2015. CuCo 2 O 4 nanoparticles on nitrogenated graphene as highly efficient oxygen evolution catalyst. Journal of Power Sources, [online] 281, pp.243-251. Available at:
<https://www.sciencedirect.com/science/article/pii/S0378775315002232> [Accessed 12 March 2021].

[107] Li, M., Xiong, Y., Liu, X., Bo, X., Zhang, Y., Han, C. and Guo, L., 2015. Facile synthesis of electrospun MFe2O4(M = Co, Ni, Cu, Mn) spinel nanofibers with excellent electrocatalytic properties for oxygen evolution and hydrogen peroxide reduction. Nanoscale, [online] 7(19), pp.8920-8930. Available at:
<https://pubs.rsc.org/en/content/articlelanding/2015/NR/C4NR07243J#!divAbstract> [Accessed 12 March 2021].

[108] Davodi, F., Tavakkoli, M., Lahtinen, J. and Kallio, T., 2017. Straightforward synthesis of nitrogen-doped carbon nanotubes as highly active bifunctional electrocatalysts for full water splitting. Journal of Catalysis, [online] 353, pp.19-27. Available at:
<https://www.sciencedirect.com/science/article/pii/S0021951717302439> [Accessed 12 March 2021].

[109] Zhang, M., Ma, Z. and Song, H., 2021. Preparation and Application of Fe-N Co-Doped GNR@CNT Cathode Oxygen Reduction Reaction Catalyst in Microbial Fuel Cells. Nanomaterials, [online] 11(2), p.377. Available at: <https://pubmed.ncbi.nlm.nih.gov/33540737/> [Accessed 12 March 2021].

[110] Zhang, J., Zhao, Z., Xia, Z. and Dai, L., 2015. A metal-free bifunctional electrocatalyst for oxygen reduction and oxygen evolution reactions. Nature Nanotechnology, [online] 10(5), pp.444-452. Available at: <https://www.nature.com/articles/nnano.2015.48?message-global=remove> [Accessed 12 March 2021].

[111] Suntivich, J., May, K., Gasteiger, H., Goodenough, J. and Shao-Horn, Y. (2012). ChemInform Abstract: A Perovskite Oxide Optimized for Oxygen Evolution Catalysis from Molecular Orbital Principles. ChemInform, [online] 43(11), p.no-no. Available at: https://science.sciencemag.org/content/334/6061/1383.full [Accessed 30 Nov. 2018].